

Characterization of Anthocyanin Dyes and Investigation of Charge Transport in TiO₂ Dye Sensitized Solar Cells

Simiyu Justus B.Sc, MSc (Nairobi)

A thesis submitted in fulfillment of the requirements for the degree of
Doctor of Philosophy (Physics) of the University of Nairobi

Department of Physics, University of Nairobi
September, 2010


University of NAIROBI Library



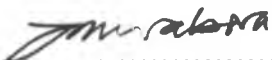
0439137 1

Declaration

This Thesis is my own work and has not been examined or submitted for examination in any other University


Signed 
Simiyu, Justus: Reg. No. I80/9152/2001
Dated 12/09/2010

This thesis had been submitted for examination with our approval as advisors:

Signed: Supervisor 
Prof. Julius M. Mwabora

Department of Physics, University of Nairobi, Kenya

Dated 13/9/2010

Signed: Supervisor 
Prof. Bernard O. Aduda

Department of Physics, University of Nairobi, Kenya

Dated 13/9/2010

Dedication

I dedicate this work to my entire family for the patience they exercised during the course of my work. To my Dad who didn't live through to witness the end of this: *The work has just began*. To my dear mother who gave me a shilling every morning of my primary school days: *May you live to enjoy the fruits of your labour*.

Acknowledgements

I give honour and gratitude to God for giving me the gift of life and energy to contribute to humankind through this research. I am most grateful to my academic advisors Prof. Julius Mwabora and Prof Bernard Aduda for their guidance, patience and their wish to see me successful in this work. I also wish to acknowledge my advisors at Uppsala University, Prof Anders Hagfeldt, Prof. Sten-Erik Lindquist, Prof. Claes-Goran Granqvist, Prof. Gunnar Niklasson and Dr. Gerrit Boschloo for their informed criticism and guidance during my research work at the Departments of Solid State Physics and Physical Chemistry, Uppsala University. I wish to also acknowledge the input in terms of resourceful discussions with group members at the Physical Chemistry's dye sensitized research group at Uppsala University, namely Dr. Kazuteru Nonomura, Dr. Jarl Nissfolk, Dr. Leif Haeggman, Dr. Alex Agrios, Dr. Nick Vlachopoulos and Ever Unger. I wish to acknowledge the assistance I got from senior scientists at the Angstrom Laboratory's clean room, Uppsala University during my work on XPS, SEM and XRD analysis, especially Dr. Jun Lu and Mr. Boniface Muthoka at the Solid State laboratory, University of Nairobi. I wish to also give appreciation to the Department of Chemistry, University of Nairobi especially Prof. Midiwo's laboratory for extraction of anthocyanin pigments and Dr. Duke Orata for review of electrochemistry.

The following institutions are gratefully acknowledged: The University of Nairobi for the tuition waiver and study leave for my PhD, a job opportunity while studying and for providing an opportunity to do research at the university. DAAD for providing me with a full scholarship to do my PhD research work at the University of Nairobi, International Programmes in Physical Sciences (IPPS), through Uppsala University, Sweden for providing me with an opportunity for research visit at Uppsala University and acquisition of crucial equipment for my research at the university of Nairobi.

Members of the Condensed Matter Research Group (University of Nairobi), Physical and Analytical Chemistry (Uppsala University) and Solid State Physics (Uppsala University) groups are acknowledged for useful discussions and interactions during the regular group meetings and the warm friendship they provided contributed a great deal to the success of this work. To you all thank you indeed.

Abstract

TiO₂ dye sensitized electrochemical solar cells employing naturally occurring anthocyanin dye pigment have been fabricated. The films were coated by screen-printing method from P25 Degussa as the starting material. Absorption characteristics of the dye pigment was studied as well as current – voltage (*I-V*) and incident photon to current conversion efficiency (*IPCE*) on complete solar cells sensitized with the anthocyanin pigment. Electron transport and recombination studies were carried out on complete solar cells sensitized with ruthenium complex dye employing time resolved intensity modulated photocurrent (IMPS) and photovoltage spectroscopy (IMVS). Structural characteristics have shown that the films were crystalline composing mainly of anatase TiO₂ with particle sizes ranging between 15 to 30 nm in diameter. XPS analysis on the films showed that Ti was completely oxidized in TiO₂ with Ti 2p state exhibiting spin-orbit splitting that resulted in peaks at 461.5 eV and 467.0 eV of binding energy. Absorption characteristics of anthocyanin pigment showed that the pigment lost the absorption maximum at 550 nm upon adsorption on TiO₂ surface. However, this was regained after the pH was adjusted to 2.00. The *I-V* characteristics of the solar cells showed that the overall efficiency depended strongly on the pH of the dye pigment with the sample at pH 2.00 showing the best performance both in terms of current-voltage (*I-V*) and incident photon to current conversion efficiency (*IPCE*) characteristics. The photocell recorded J_{sc} of 3.17 mA/cm², V_{oc} of 0.49 V, $FF = 66\%$ giving the overall efficiency of 1.04 %. The results were for TiO₂ film thickness 6.5 μm and exposed area of 0.48 cm². The same cell at pH 2.00 exhibited the highest overall *IPCE* compared with the other pH levels. The results show that anthocyanin dyes are able to convert light to electricity with quantum efficiencies of about 4 % maximum in the visible spectrum.

The performance of anthocyanin dye pigment and ruthenium sensitized solar cells were compared with ruthenium N719 sensitized solar cell of similar film thicknesses which recorded J_{sc} of 6.16 mA/cm², V_{oc} of 0.83 V, FF of 65 % giving the overall efficiency of 3.29 %. The anthocyanin-sensitized solar cell recorded an $IPCE_{max}$ of 4% in the visible compared to 27% for ruthenium sensitized solar cell. The difference in $IPCE$ maximum between the anthocyanin pigment and ruthenium dye complex is due to their kind of transition with the anthocyanin being ligand to ligand charge transition while ruthenium complex being metal to ligand charge transfer (MLCT) transition.

Electron transport and recombination studies were carried out on complete solar cells sensitized with ruthenium complex dye at film thickness 3.0, 6.0 μm , 12.8 μm , 23.5 μm and 25.3 μm . The 3.0 μm thick film exhibited the fastest photovoltage decay while the 12.8 μm thick film had the slowest photovoltage decay. This was attributed to the effect of electron recombination via redox electrolyte affecting the thinnest films and a balance between charge transport and recombination being attained at film thickness 12.8 μm . The samples, in general, exhibited linear and non-linear photovoltage decay profiles with the non-linear decay profile being observed at the onset of the decay while the linear at longer time scales of the decay. The non-linear profile at the onset of decay was attributed to the reorganization and switching effects the cells are in and the linear profile at the longer time scale being the steady state. Normalized current transients showed that there was a fast current decay at shorter time scale for thick films when illuminated from the backside. However, a single exponential decay was observed at longer time scales under same illumination mode. Charge accumulation in the

films was observed to increase with film thickness, which was attributed to the rise in trap states with increase in film thickness.

Table of Contents

List of Content	Page
Declaration	i
Dedication	ii
Acknowledgements	iii
Abstract	iv
Table of Contents	vii
List of Symbols	xi
List of Abbreviations	xiv
List of chemical formulae	xvi
List of figures	xvii
List of Tables	xx
1. CHAPTER 1: Introduction	1
1.1 Introduction	1
1.2 Photovoltaics	2
1.3 Statement of the Problem	6
1.4 Significance of the Study	6
1.5 Objectives of Study	7
2. CHAPTER 2: Literature Review	9
2.1 Introduction	9
2.2 Historical Perspective of DSCs.	11
2.3 Basic Principles of Dye Sensitized Solar Cells.	12
2.3.1 The sensitizer	14
2.4 Efficiency Limiting Processes in DSC.	22
3. CHAPTER 3: Theoretical Background	30
3.1 Introduction	30
3.2 Semiconductor Electrochemistry	30
3.2.1 Semiconductor-electrolyte interface (SEI)	30
3.2.2 Charge transfer processes at the SEI	36

3.2.3	Band bending	36
3.2.4	Dye sensitization	37
3.3	Characterization Methods	39
3.3.1	X-Ray Photoelectron Spectroscopy (XPS)	39
3.3.2	X-Ray Diffraction (XRD).	42
3.3.3	Current-voltage (<i>I-V</i>) characterization	44
3.3.3.1	Open circuit voltage (V_{oc})	46
3.3.3.2	Short circuit current (I_{sc})	47
3.3.3.3	Fill Factor (<i>FF</i>)	47
3.3.3.4	Solar-to-electric power conversion efficiency	48
3.3.4	Incident photon to current conversion efficiency (<i>IPCE</i>) characterization	49
3.4	Charge Transport and Recombination	50
3.4.1	Photovoltage decay	54
3.4.2	Charge extraction	55
3.4.3	Electrochemical potential characterization.	56
4.	CHAPTER 4: Experimental Methods	58
4.1	Introduction	58
4.2	Sample Preparation	59
4.2.1	Dye preparation	59
4.2.2	Dye characterization	59
4.2.3	TiO ₂ paste preparation	60
4.2.4	Thin film deposition	60
4.2.5	Counter-electrode preparation	61
4.2.6	Electrolyte preparation	61
4.2.7	Complete solar cell assembly	62
4.3	Thin Film Characterization	62
4.3.1	Scanning Electron Microscopy (SEM).	62
4.3.2	X-Ray Diffraction (XRD).	63
4.3.3	X-Ray Photoelectron Spectroscopy (XPS).	63
4.4.	Solar Cell Characterization	63

4.4.1	<i>I-V</i> characterization	63
4.4.2	Photoelectrochemical characterization	65
4.4.3	Incident Photon-to-Current Conversion Efficiency (<i>IPCE</i>)	67
4.5	Electron Transport and Lifetime Measurements	68
4.5.1	Photocurrent and voltage decay transients	69
4.5.2	Photovoltage decay measurements	70
4.5.3	Charge extraction	70
4.5.4	Electrochemical potential analysis	70
5.	CHAPTER 5: Results and Discussion	72
5.1	Introduction	72
5.2	Structural Characterization	72
5.3	X-ray Photoelectron Spectroscopy (XPS)	75
5.4	Dye Characterization	77
5.5	Solar Cells Characterization	82
5.6	Effect of Film Thickness	89
5.6.1	<i>I-V</i> characteristics versus film thickness	89
5.6.2	Electron transport and recombination studies	93
6.	CHAPTER 6: Conclusion and Suggestions for Further Work	111
6.1	Conclusion	111
6.2	Suggestions for Further Work	113
	REFERENCES	116
	APPENDICES	128
	I LabVIEW Development and Implementation	129
A1.0	Introduction	129
A1.1	Communication Protocol	129
A1.2	Automation of <i>I-V</i> Characterization System	130
	II IPCE Characterization Automation	134
A2.0	Introduction	134
A2.1	Communication Protocol	134
A2.2	Algorithm for Automating <i>IPCE</i>	135
A2.3	Flowchart	136

List of Symbols

h	Planck's constant divided by π
A	area of cell exposed to light
c	speed of light in a air
C_i	concentration species i in a solution
c_o	speed of light in the atmosphere
C_{ox}	concentration of oxidation species
C_{red}	concentration of reduction species
d	film thickness
de_γ	energy density
d_{hkl}	crystal's inter-planar spacing
D_i	diffusion coefficient
$d\Omega$	solid angle element
e	charge of an electron
e^-	electron
E	energy of states
E^0	standard redox potential
E_B^V	electron binding energy
E_c	energy of conduction band
E_f	energy of Fermi level
$E_{f,redox}$	Fermi level of the redox electrolyte
E_K	kinetic energy of the emitted electron
E_{pa}	anodic peak potential
E_{pc}	cathodic peak potential
E_V	energy of the valence band
$f(E)$	Fermi-Dirac distribution function
h	Planck's constant
$h\nu$	energy of an electron or photon
I_{dark}	dark current
I_{mp}	current at maximum power point
i_{pa}	anodic peak current
i_{pc}	cathodic peak current
I_{ph}	photogenerated current
I_s	saturation current
I_{sc}	short circuit current
$J_i(x)$	flux of species i
J_{sc}	short circuit photocurrent density (I_{sc} divided by area, A)
$J_{sc,0}$	current offset or current density without intensity modulation
$J_{sc,max}$	initial current transient
K	constant term in the photovoltage decay experiment
k_B	Boltzmann's constant
L	diffusion length
l	radiation path length
L_D	Debye length
l_o	thickness of the atmosphere
m	ideality factor

m^*_{dos}	effective electron mass
ms	millisecond
$N(E)$	density of states
N_C	effective density of conduction band states
n_C	density of electrons in conduction band
N_D	density of donor states
N_e	distribution of states
${}_nE_f$	quasi Fermi level of electrons under illumination
$N_{electrons}$	number of electrons
$N_{photons}$	number of photons
ns	nanosecond
$N_{trap}(E)$	density of trap states
Ox	oxidized species
P_{in}	power of incident radiation
P_{max}	maximum power
ps	picosecond
q	quantity of charge.
Q_{oc}	charge accumulation at open circuit
Q_{photo}	photogenerated charge
Q_{trap}	charge residing in trap states
r	crystal radius
R_s	series resistance
R_{sh}	shunt resistance
S	dye molecule in ground state
s	second
S^*	dye molecule in excited state
S^+	dye molecule in oxidized state
S_i	instrument broadening constant for x-ray diffractometer
T	temperature
t_e	electron lifetime
t_{max}	time it takes for V_{sc} to rise to a maximum value
t_{rec}	time constants recombination
t_{tr}	time constant for transport
V	applied voltage or bias potential
$v(x)$	velocity with which a volume element in a solution moves along the x-axis
V_{mp}	voltage at maximum power
V_{oc}	open circuit voltage
$V_{oc,0}$	open circuit voltage without modulation
$V_{sc,max}$	maximum internal voltage
V_T	thermal voltage
z_i	charge on the species i
α	incident angle of sun's radiation relative to the earth's surface
β	constant representing exponential power in open circuit voltage decay
ΔJ	current modulation magnitude
ΔV	voltage modulation magnitude

$\Delta\Phi_{sc}$	total band bending at the semiconductor-electrolyte interface
ϵ	dielectric constant of a material
ϵ_0	permittivity in free space
η	solar-to-electric power conversion efficiency
η_{abs}	light absorption efficiency
η_{coll}	charge collection efficiency
η_{inj}	charge injection efficiency
κ	Scherer constant
λ	wavelength
λ_{max}	maximum density per wavelength
μs	microsecond
π^*	transition state for ligand
π	pi = 3.14 radians
ν	frequency of light
Φ_{sc}	semiconductor band bending

List of Abbreviations

AM	air mass
AM0	air mass zero
AM1.5	air mass 1.5
BE	binding energy
BET	Brunauer-Emmer-Teller (system of measuring porosity)
CCD	charged coupled device
CE	counter electrode
CV	cyclic voltammetry
D149	commercial name for indoline dye
DAQ	data acquisition
DFT	density functional theory
DSC	dye sensitized solar cell
EE	electrolyte-electrode illumination mode
<i>FF</i>	fill factor
FWHM	full width at half maximum
GPIB	general purpose interface bus
HOMO	highest occupied molecular orbital
I/O	input/output
IAEA	International Atomic Energy Agency
IEA	International Energy Agency
IMPS	intensity modulated photocurrent spectroscopy
IMVS	intensity modulated photovoltage spectroscopy
IPCC	International Panel on Climate Change
<i>IPCE</i>	incident photon-to-current conversion efficiency
ITO	indium tin oxide
<i>I-V</i>	current-voltage
labVIEW	laboratory virtual instruments electronics workbench
LED	light emitting diode
LUMO	lowest unoccupied molecular orbital
M	molarity
MLCT	metal-to-ligand charge transfer
MT	multiple trapping
N3	commercial name for RuL ₃ (NCS) ₂ dye complex
N719	commercial name for RuL ₂ (NCS) ₂ complex
NHE	normal hydrogen electrode
oc	open circuit
PDF	powder diffraction file
RE	reference electrode
Red	reduced species
RS232	serial communication protocol
SCE	saturated calomel electrode
SCPI	standard commands for programmable instruments
SE	substrate-electrode illumination mode
SEI	semiconductor-electrolyte interface
SEM	scanning electron microscopy

spiro-OMeTAD	2,2(,7,7(-tetrakis-(N,N-di-pmethoxyphenylamine) 9,9(-spirobifluorene polymer complex
TCO	transparent conducting oxide
TDDFT	time dependent density functional theory
TOF	time-of-flight
TW	tera watt
UV	ultraviolet
VI	virtual instruments
Vis	visible
VISA	virtual instruments software architecture
WE	working electrode
XPS	X-ray photoelectron spectroscopy
XRD	X-ray diffraction

List of chemical formulae

Al	aluminium
CdS	cadmium sulphide
CdTe	cadmium telluride
CN	carbon-nitrogen ligand
CO ₂	carbon dioxide
COOH	carboxyl groups
Cu(In,Ga)Se ₂	copper indium or gallium di-selenide
CuInSe ₂	copper indium di-selenide
F:SnO ₂	fluorine-doped tin oxide
GaAs	gallium arsenide
H ₂ PtCl ₆	hexachloroplatinic acid
InP	indium phosphate
K	potassium
MPN	methoxypropionitrile
OH	hydroxyl radicals
Pt	platinum
TBA	tetrabutyl ammonium
TBA-I	tetrabutyl ammonium iodide
TBPy	tetrabutyl pyridine
TiO ₂	titanium dioxide
ZnO	zinc oxide

List of Figures

Figure No.	Figure Caption	Page
1.1	Solar cell timeline from 1975 to 2009	5
2.1	Structure of dye sensitized TiO ₂ solar cell	9
2.2	Operation scheme showing energy flow in dye sensitized solar cell	13
2.3	The structure of Ruthenium dye complexes	16
2.4	Photocurrent action spectra for ruthenium dye complexes	17
2.5	Chemical structures of the most abundant anthocyanidins	20
2.6	Principle of operation and energy level scheme of the dye-sensitized nanocrystalline solar cell showing the processes an electron goes through	22
2.7	The dynamics of the processes in the DSC	24
3.1	Energy levels for a metal, an insulator, and a semiconductor	31
3.2	Electrochemical measurement system showing the working electrode (WE), reference electrode (RE) and counter electrode (CE)	34
3.3	An ideal cyclic voltamogram for a reversible single electrode transfer reaction showing important peak parameters	35
3.4	Band bending at the semiconductor-electrolyte interface for n-type semiconductor	36
3.5	Semiconductor-electrolyte interface when the electrode is sensitized	38
3.6	An illustration showing x-ray photons with enough energy to remove the core electrons of a material	40
3.7	Typical XPS spectra showing characteristic O1s core level peak in TiO ₂	41
3.8	An X-ray diffraction pattern for SnO ₂ showing the relative peak intensity plotted as a function of 2θ	43
3.9	A typical experimental <i>I-V</i> curve showing variation of current with voltage and corresponding power curve	46
3.10	An equivalent circuit for a solar cell showing the series (R_s) and shunt (R_{sh}) resistances	48
3.11	The photocurrent response to a small-amplitude square waveform perturbation	51
3.12	Typical responses showing transport time plotted as a function of photocurrent and inset: photocurrent decay for one bias intensity	52
3.13	Sketch of photocurrent decay for one value of modulation intensity	53
3.14	Normalized photocurrent decay plotted on logarithmic scale	54
3.15	V_{oc} decay with respect to elapsed time in the dark	55
3.16	A sketch of internal voltage decay at different diode illuminations	57
4.1	Block diagram of the current-voltage characterization setup	64

4.2	Setup for cyclic voltametry studies	65
4.3	Schematic set up for <i>IPCE</i> characterization	67
4.4	Block diagram of the transport and lifetime studies setup	68
5.1	SEM micrograph for (a) screen printed TiO ₂ film with P25 as the starting material (b) coated by doctor blade technique with titanium tetrachloride as the starting material	72
5.2	XRD surface scans for TiO ₂ films made from (a) P25 by screen printing and (b) colloidal TiO ₂ by doctor blade techniques	74
5.3	XPS spectra for TiO ₂ showing Ti 2p and O 1s peaks for titanium and oxygen species respectively	75
5.4	XPS spectra for TiO ₂ showing (a) Ti 2p and (b) O 1s peaks	76
5.5	Titration curve for anthocyanin pigment using 0.01M NaOH	78
5.6	Absorption spectra for anthocyanin (a) dye in solution and (b) dye sensitized TiO ₂ photoelectrode.	78
5.7	Schematic representation of anthocyanin attachment by alcoholic condensation (a) and by chelating effect (b) to the TiO ₂ surface	79
5.8	Absorption spectra for anthocyanin dye at (a) pH 2.84 (b) pH 5.17 (c) pH 7.07 and (d) pH 8.3	80
5.9	Absorption spectra for anthocyanin dye pigment (a) before and (b) after being adsorbed on TiO ₂ photoelectrode at pH 2.5	81
5.10	<i>I-V</i> curves for anthocyanin sensitized solar cells at different pH levels of the dye compared with Ru N719 sensitized solar cell	83
5.11	<i>IPCE</i> for anthocyanin dye sensitized solar cell (a) pH 2.84, (b) pH 8.30 and (c) pH 5.17	84
5.12	Cyclic voltamograms on anthocyanin dye pigment in different environments where (a) the solution is stirred, (b) N ₂ purged and (c) Ar bubbled.	87
5.13	<i>I-V</i> characteristics of sealed solar cells from screen printed TiO ₂ films of varying thicknesses	90
5.14	Relationship between film thickness (<i>d</i>) and short circuit photocurrent density (<i>J_{sc}</i>)	92
5.15	<i>V_{oc}</i> decay profile of TiO ₂ solar cells of varying film thicknesses at highest illumination intensity	94
5.16	<i>V_{oc}</i> decay profiles for TiO ₂ solar cells at varying film thickness showing (a) decay curves at the shorter time scale and (b) at the longer time scale	94
5.17	Calculated electron lifetime from <i>V_{oc}</i> decay curves	96
5.18a	Electron transport time (<i>t_{tr}</i>) as a function of short circuit current (<i>J_{sc}</i>) for samples of varying thickness	97
5.18b	Current transient plot from which the transport time and offset current (<i>j_{sc}</i>) are obtained and plotted in (a)	97
5.19	Current transients for 25.3 μm thick film at the highest illumination intensity. (a) is the raw data and (b) is obtained from (a) by normalizing it with respect to parameters <i>J_{sc,0}</i> , <i>t_{tr}</i> and ΔJ_0	99
5.20	Normalized current transient for 25 μm thick film	

	at the highest modulating light intensity	99
5.21	An illustration of the variation of quasi Fermi level with film thickness, d at (a) shorter and (b) longer timescales	101
5.22	Accumulated charge (Q_{oc}) at different V_{oc} for different film thickness	102
5.23	Relationship between charge and film thickness	103
5.24	Internal voltage decay curves at a constant illumination of 15.6 mWcm^{-2} for different film thicknesses	104
5.25	Internal voltage decay curves for $25.3 \text{ }\mu\text{m}$ thick film at varying intensity (in mWcm^{-2}) obtained by varying the light source bias voltage	106
5.26	Maximum voltage ($V_{sc,max}$) as a function of light intensity for $25 \text{ }\mu\text{m}$ thick film.	107
5.27	Relationship between t_{max} and $V_{sc,max}$ for $25 \text{ }\mu\text{m}$ thick film	108
5.28	Comparison of t_{max} with transport time obtained from IMPS at varying illumination intensity	109
A1	A flow chart showing the events of the processes of measuring and plotting the current voltage characteristics	132
A2	Flow chart for obtaining IPCE data from a solar cell	136

List of Tables

	Page	
5.1	Peak list and particle size for TiO ₂ film made from P25	75
5.2	Summary of IV characteristics at different pH levels	83
5.3	A comparison of IV and <i>IPCE</i> characteristics between anthocyanin sensitized solar cell at pH 2.00 and ruthenium N719 sensitized solar cell	86
5.4	<i>I-V</i> characteristics for solar cells sensitized with ruthenium N719 at varying film thickness	90
5.5	Relationship between t_{max} and film thickness	105

Chapter One

Introduction

1.1. Introduction

Energy is essential for development. Nearly every aspect of development – from reducing poverty to improving health care – requires reliable access to modern energy services. The worldwide human quest for more energy of which electricity generation accounts for about 40 % of humanity's total energy needs has played a big role in the climate change of the Earth. Electricity generation - mostly from the combustion of fossil fuels such as coal, oil and natural gas accounts for more than 10 Gigatonnes of carbon dioxide (CO₂) produced every year (Birol, 2007). CO₂ (one of the greenhouse gases in our atmosphere) emission into the atmosphere in significantly large quantities has lead to the widely talked about global warming (IPCC, 2007), the result of which has been an increase in the average sea level at a rate of 1.8 mm per year between 1961 and 2003 (IPCC, 2007).

As the world's population increases and the way/standard of living changes, the demand for energy also increases with estimated electricity consumption in 2050 to be four times greater than today (European Commission, 2006; IEA, 2007). Ways of reducing the CO₂ emissions accompanying this consumption has been a major challenge, alongside reduction of overdependence on fossil fuels. The approach has been to embrace other technologies that are renewable and environmentally friendly. Much as nuclear power is able to supply 15% of world's energy (El Baraday, 2007), it has related health risks and the known resources of uranium at current levels of use are estimated to last for just another 80 years. Moreover, this

technology may not easily be used in many countries and some countries have been shutting down their reactors. Due to these concerns, there has been urgent need to find a suitable renewable energy source in which solar energy has been one of them.

The earth receives about 105 TW of solar power at its surface and harvesting this energy for one hour would supply the energy needs of the earth for one year (Quirin, *et. al.*, 2008). One of the techniques of harvesting this vast amount of energy is photovoltaics and it is the work that is reported in this thesis.

1.2 Photovoltaics

Photovoltaic devices derive their theoretical basis from Edmund Becquerel's experiment (Becquerel, 1848) and Planck's explanation of the spectral distribution of solar spectrum (Williams, 1960). The theory (known as photovoltaics) states that photons of suitable energy incident on a semiconductor excite electrons from the valence band into the higher energy conduction band where they are collected and transported to the outer circuit. The development of silicon electronics in the 1950s witnessed the breakthrough in photovoltaic devices when p-n junction boron doped silicon wafers were developed, achieving near 6% conversion efficiency (Chapin, *et. al.*, 1954). The solar cells based on the silicon technology were categorized in the first generation of solar cells.

The energy crisis in 1970 greatly stimulated the interest in and funding for research in alternative sources of energy, including photovoltaics. It was during this period that polycrystalline and amorphous silicon, CdTe, CuInSe₂ and Cu(In,Ga)Se₂ (also known as

second generation) solar cell devices were developed. These were based on thin film technology of p-n junction semiconductors for charge production and separation. The advantage of the second generation, over first was their flexibility, along with lower cost. This made it possible for light and flexible solar panels being produced that were easily used in portable devices like watches, calculators, etc. Though the two technologies have been in the market for close to four decades, their penetration to house holds especially in developing and under-developed economies is not yet fully achieved. This has been primarily due to the high installation cost as a result of the expensive production techniques that are involved.

The quest for cheaper photovoltaic devices led to new concepts of solar cells being developed that included nanostructured dye sensitized solar cells (DSCs). The technology for this type of devices is based on the mechanism of regenerative photoelectrochemical process of a large band gap semiconductor such as TiO_2 , coupled with a suitable sensitizer (O'Regan and Grätzel 1991). Others in this category are polymer solar cells and nanocrystalline solar cells. This new group of solar cells has been categorized in the third generation photovoltaics, as they are different from the first and second generation. The main difference is that the first and second-generation devices are p-n junction devices while the third generation does not necessarily rely on the p-n junction to perform charge separation.

A dye-sensitized solar cell comprises of a wide band gap semiconductor with a surface adsorbed dye sensitizer supported on a transparent conducting oxide (TCO) coated glass substrate. This forms an interface with a redox-coupled electrolyte that helps in ion diffusion and dye regeneration. This device has several advantages over the 1st and 2nd generation

technologies, one among them being that its performance is insensitive to temperature change; hence the rise in operating temperature to 60 °C (the temperature attained at full one sun illumination) has no effect on the conversion efficiency (Grätzel, 2000). It has also been shown elsewhere (Grätzel, 2005) that DSC's external quantum yield of photocurrent generation is close to one if optical losses in the conducting substrate are accounted for. The device's performance also mimics photosynthesis which is known to be a highly efficient process. With these qualities therefore, DSC have the potential to achieve high efficiencies at a lower cost compared to the 1st and 2nd generation technologies (Grätzel, 2003). Currently, the components that contribute to DSCs being uneconomical are the dye sensitizer (the ruthenium metal based complex) and the TCO substrate. Therefore the use of alternative sensitizers can lower the cost of the devices and hence be economical. The options available have been to use organic sensitizers, among them naturally occurring plant based anthocyanin pigments. Apart from cost there are other challenges that DSCs are facing, key among them being the low overall conversion efficiencies. The current record efficiencies reported of 11.1% (Chiba, *et. al.*, 2006) and more recently 11.3% (Shi, *et. al.*, 2008) using ruthenium based dye complexes are still half the efficiency for crystalline solar cells. However compared to the other technologies, DSC's entry (circled in figure 1.1), is relatively recent but the efficiencies are close to the amorphous silicon's. Some of the factors that lead to this low overall efficiency in these devices are the electron injection efficiency at the dye-semiconductor interface, charge transport in the mesoporous semiconductor film and charge collection efficiencies at the counter electrode electrolyte interface.

Best Research-Cell Efficiencies

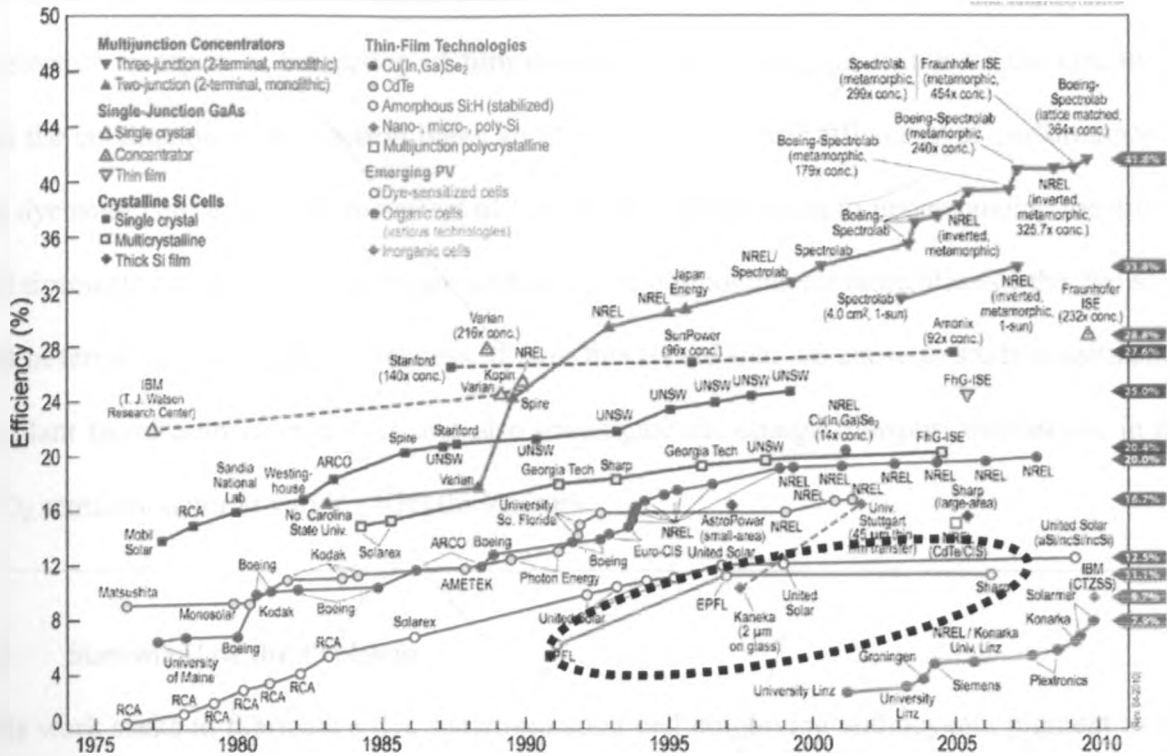


Figure 1.1: Solar cell efficiency timeline from 1975 to 2010 (Nelson, 2010). The efficiency timeline for DSC is shown with dotted circle.

In summary, dye sensitized solar cells promise a cheap source of electrical power as compared to silicon based solar cells, though they still have low conversion efficiencies. One area contributing to this low efficiency is the electron transport mechanism which is not yet fully understood, besides the need to develop cheap but stable sensitization dyes. Previous studies on anthocyanins as alternative sensitizers have shown that they have the attaching problem on the TiO₂, mainly due to protonation. Investigation of the effect of pH (hence protonation) on the absorption and current-voltage (*I-V*) properties of the dye may give information on the attaching ability of these pigments on TiO₂ and further information on the possibility of introducing attaching groups through protonation. Furthermore charge transport in semiconductor materials for DSC is not yet fully understood. Previous studies on charge

transport have not dealt with the interaction of semiconductor with redox electrolyte in terms of electron transport as a function of film thickness. Since diffusion length for the electrolyte and the conduction band electron bears an effect on the overall efficiency of performance of the dye solar cell, a study of the effect of film thickness will bring to understanding the modes and timescales of the charge transport and also give a guideline on fabrication of the dye solar cell in terms of optimal film thickness. It is in this regard that we chose to study sensitization by plant based anthocyanin dyes and also investigate the charge transport mechanism in the TiO_2 semiconductor at varying film thicknesses.

1.3 Statement of the Problem

This work seeks to fabricate a dye sensitized solar cell employing anthocyanin pigment as the dye sensitizer and study the effect of dye's pH level on charge injection efficiency. The study further seeks to analyze the effect of film thickness on charge transport in the mesoporous structure through the study of charge transport time and lifetime, charge accumulation and electrochemical potential analysis. This is in an attempt to provide an understanding on the mechanism of dye adsorption, charge transfer, charge transport and also give an option for a cheaper dye sensitized solar cell in terms of fabrication and cost.

1.4 Significance of Study

The study of alternative sensitization dyes especially the naturally occurring pigments, their interaction with the semiconductor and electrolyte is expected to contribute to the search for combining the important factors of high efficiency and stability with low cost.

This study is expected to further the understanding of the mechanism of electron transfer from surface adsorbed dye to the semiconductor. While ruthenium based dyes used to attain high efficiencies but they are difficult to synthesize, readily available natural dyes are employed to expose aspects of kinetics and energetics that determine the injection and energy conversion efficiencies. Therefore, the study of alternative sensitization dyes (mainly naturally occurring) pigments at the microscopic level may yield cheaper, readily available yet efficient sensitizers which may give hope for large scale utilization.

The electron transport mechanism in DSC is an area still under intensive investigations to establish the basis for further improvements on the efficiencies in this type of solar cells. Much as the mode of electron transfer in the semiconductor has been established, there are other factors such as the film thickness related to the electron generation, transport and collection that have not been fully investigated. Others are the interaction of the semiconductor with the redox electrolyte upon illumination. The study of electron transport in the semiconductor by the time resolved techniques will provide important information regarding the factors mentioned above where a basis towards the improvement on the film performance will be brought out.

1.5 Objectives of Study

The aim of this study is to fabricate a dye sensitized solar cell based on naturally occurring anthocyanin dye pigments, and investigate the parameters involved in the charge transfer and transport processes in dye solar cells. The specific objectives are:

- i) To study the characteristics of anthocyanin dye pigment in solution and when used for sensitization with TiO_2 .
- ii) To analyze the TiO_2 microstructure employing x-ray diffraction (XRD), scanning electron microscopy (SEM) and x-ray photoelectron spectroscopy (XPS) techniques
- iii) To characterize the fabricated solar cells employing cyclic voltametry (CV), current-voltage (I - V) and incident photon to current efficiency (IPCE) measurement techniques.
- iv) To determine the effect of film thickness on electron transport and recombination employing time-resolved photocurrent and photovoltage transient techniques. These are namely
 - Intensity modulated photocurrent spectroscopy
 - Photovoltage decay
 - Charge extraction
 - Electrochemical potential

Chapter Two

Literature Review

2.1 Introduction

A dye sensitized solar cell is a many components device comprising the semiconductor as the active material, dye for sensitization, redox coupled electrolyte and a counter electrode. It has two electrodes, the working electrode (WE) and the counter electrode (CE) with the working electrode consisting of a dye-sensitized mesoporous semiconductor on a conducting substrate (Figure 2.1).

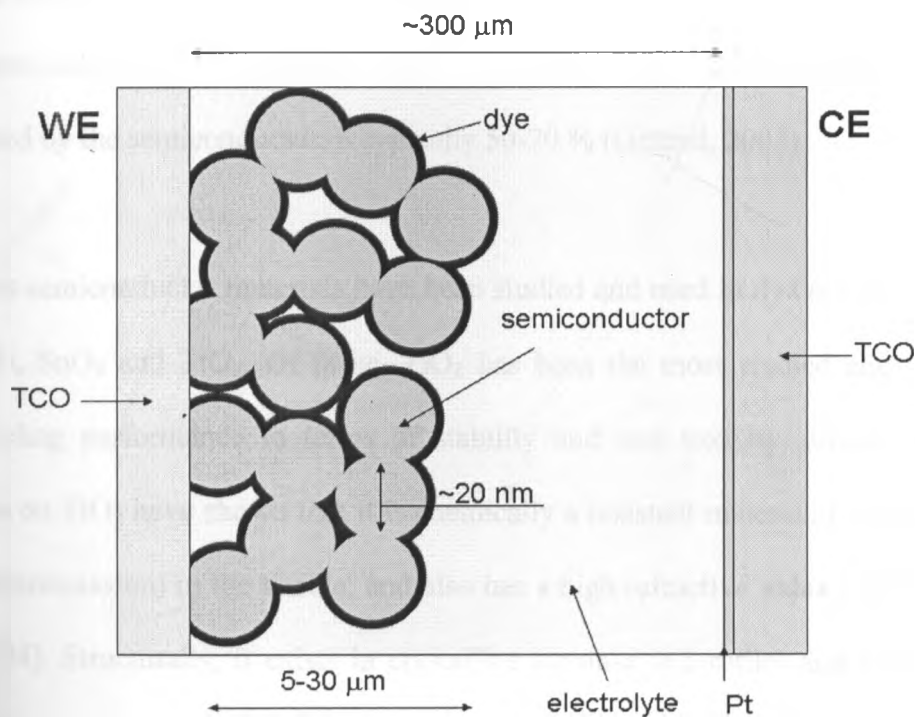


Figure 2.1: Structure of dye sensitized TiO_2 solar cell. CE is the counter electrode, WE is the working electrode and TCO transparent conducting oxide (Grätzel, 2005).

The conducting substrate is made of a thin layer of transparent conducting oxide (TCO-layer) coated on a glass plate. The TCO-layer is usually fluorine-doped tin oxide (F:SnO₂) or indium tin oxide (ITO). The counter electrode also consists of a glass plate with a TCO-layer that is further coated a thin catalytic layer of platinum (Pt).

The space between the electrodes is filled with a redox electrolyte, usually a mixture of iodine and iodide in an organic solvent. The mesoporous film is created by sputtering, sintering or pressing semiconductor nanoparticles onto the conducting substrate. The film thickness varies from a few hundreds of nanometers to 30 µm, depending on the deposition method. The porous structure of the film has a typical internal area which is 10²-10⁴ times larger than the projected cell area. The porosity of the mesoporous film, which is the volume fraction not occupied by the semiconductor, is typically 50-70 % (Grätzel, 2003).

Various semiconductor materials have been studied and used in dye sensitized solar cells such as ZnO, SnO₂ and TiO₂. Of these, TiO₂ has been the most studied and used owing to its outstanding performance in terms of stability and non toxicity, among other advantages. Studies on TiO₂ have shown that it is chemically a resistant material, highly transparent (60 – 95 % transmission) in the visible, and also has a high refractive index (Pulka, 1984; Tang, *et al.*, 1994). Structurally, it exists in crystalline (anatase and rutile) and amorphous (brookite) forms. Anatase and rutile have energy band gaps of 3.2 eV and 3.0 eV, respectively (Kim, 1996). Owing to the above qualities, TiO₂ has been the material of choice for the semiconductor in DSCs in conjunction with ruthenium complex dyes.

2.2 Historical Perspective of DSCs

Current work on dye sensitized solar cells derives its history from photography around the same time photovoltaic effect was discovered. At the time when Becquerel was discovering photovoltaic effect (Becquerel, 1848); Louis Daguerre made the first photographic image onto a mirror-polished surface of silver bearing a coating of silver halide particles (Daguerre, 1839, Bird, 1839). The halides used in photography had band gaps ranging from 2.7 to 3.2 eV hence not photoactive for light of energy less than 2.7 eV (corresponding wavelength > 450 nm). An improvement was made in 1873 by a German photochemist, Vogel via the dye sensitization of silver halide emulsions, leading to photoresponse into the red and infra-red (Sandler, 2002). However, it was not until 1960s that scientists clearly understood the operating mechanisms of electron injection from excited state of the dye molecules into the conduction band of n-type semiconductor substrates (Williams, 1960; Bourdon, 1965; Nelson, 1965). These early dye sensitized solar cells were characterized by poor dye-anchorage on the semiconductor surface and low conversion efficiencies restricted by the limited, weak light absorption of the dye monolayer on the surface. On the other hand, thicker dye layers increased the electrical resistance of the system without adding to the current generation (Bourdon, 1965). An improvement was later achieved both in chemisorption of sensitizers, electrochemistry and the choice of photoelectrode materials following the work of Tributsch and Gerischer (Grätzel, 2000) on zinc oxide. However, most of the semiconductors used at that time had serious corrosion problem. TiO_2 became a material of choice following Fujishima and Honda's demonstration of direct photolysis of water with TiO_2 (Fujishima and Honda, 1971) in which they found out that TiO_2 electrode did not decompose after irradiation, i.e., the electrode surface was not changed and no titanium ions were detected in the electrolyte solution.

Tributsch (1971) further improved on this by demonstrating the reaction of excited chlorophyll molecules at electrodes and did a comparison with photosynthesis.

The attempt to solve the problem of dye-absorption was first approached via the concept of dispersed particles to provide sufficient interface (Duonghong *et. al.*, 1984), then followed by an attempt to use photoelectrodes with high surface roughness. This was to help in having multiple reflections at a rough surface, permitting the capture of most of the incident light by a dye monolayer with a high molecular extinction. With all these researches, a breakthrough was achieved in 1991 with a nanocrystalline photovoltaic device having a conversion efficiency at that time of 7.1 – 7.9% under AM 1.5 solar illumination (O'Regan and Grätzel, 1991). The discovery of ruthenium complex dyes like $\text{RuL}_3(\text{NCS})_2$ (commonly known as N3), and $\text{RuL}'(\text{NCS})_2:3\text{TBA}$ (commonly known as black dye), as sensitizers have pushed the efficiencies well above 10% with the current efficiency recorded being 11.3% (Shi, *et. al.*, 2008). Recent achievements on long term stability with non-volatile electrolytes has increased the prospects of practical applications and put the dye sensitized solar cell on the right path for commercialization. However, there is still need to develop more sensitizers that are cheap and also strive to obtain an understanding on the mechanism of charge transfer and transport in the semiconductor, among other processes.

2.3 Basic Principles of Dye-sensitized Solar Cells

As earlier indicated, a dye sensitized solar cell is a many component device; however, the semiconductor plays a major role since it provides the medium in which the electrons travel to

deliver power in the external circuit. A complete operation scheme is presented in figure 2.2 showing the direction of flow of charge in a DSC.

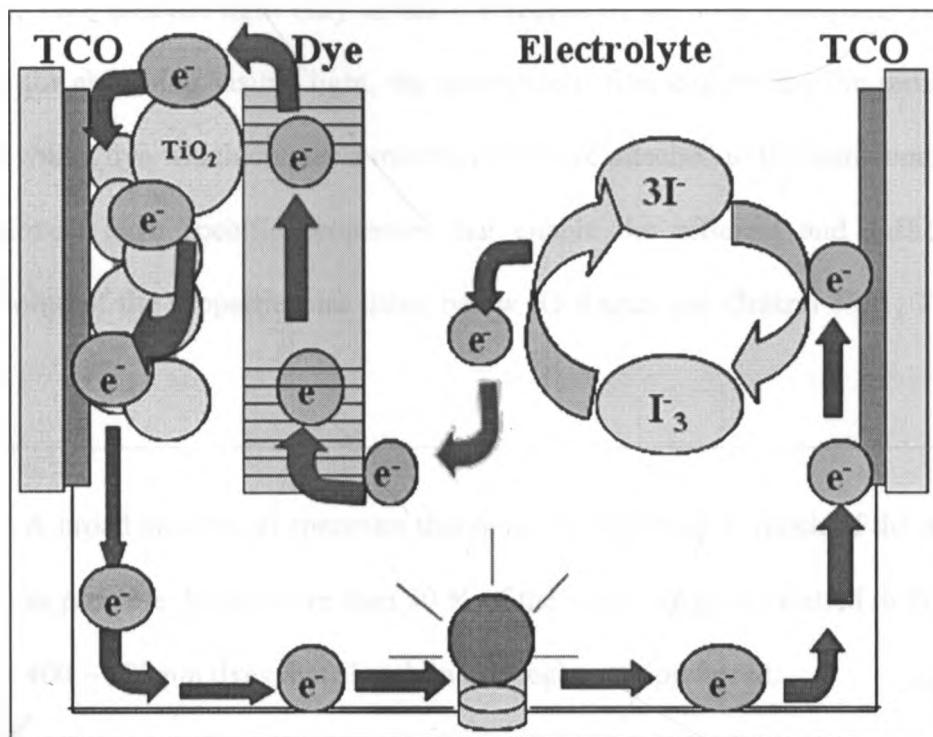


Figure 2.2: Operation scheme showing energy flow in dye sensitized solar cell.

A photocurrent is generated when a dye molecule at the TiO₂/electrolyte interface absorbs a photon and an electron from the dye molecule is injected into the conduction band of TiO₂. The negative charge injected into the semiconductor layer is compensated for by a positive charge remaining on the dye molecule, which is discharged by oxidizing a redox mediator in the electrolyte solution. After passing through the external circuit and delivering power to the load, the electrons re-enter the cell via a counter-electrode reducing the redox component. The process repeats itself, becoming self-sustaining with illumination (Smestad, 1998). Each of the components incorporated in a DSC contributes well to the overall performance of the device. For the focus of this study, the sensitizer is discussed at length.

2.3.1 The sensitizer

Due to the large energy gap of TiO_2 (~ 3.2 eV), and of other similar semiconductors (e.g., ZnO and SnO_2), TiO_2 absorbs light only in the UV region of the solar spectrum. To increase the sensitivity for absorbing visible light, the mesoporous film comprising the semiconductor, is sensitized with a dye which creates a monolayer of dye attached to the semiconductor surface. Dye sensitizers have specific properties that enable the efficient and sufficient electron transfer. Some of the properties are listed below (O'Regan and Grätzel 1991; Tennakone, *et al.*, 1997):

1. A broad absorption spectrum that helps in capturing as much of the solar radiation as possible. Since more than 50 % of the solar energy is emitted in the region from 400 – 800 nm dyes that absorb in this region are preferred.
2. The extinction coefficient of the dye molecule should be high over the whole absorption spectrum. This assists in absorption of most of the light within a monolayer of the dye because an increase of the optical density of the electrode by increasing the thickness deteriorates the photovoltage and also causes diffusion problems in the electrolyte at high current densities.
3. The excited state of the dye should lie above the conduction band of the semiconductor and its lifetime should be long enough for efficient electron injection. This guarantees fast electron injection. Since under normal electron injecting, the energy of the injecting state is that of the lowest vibrationally relaxed

excited state (which is given by the ground state oxidation potential plus the excitation energy), unless it is an extremely fast hot electron injection, energy can be lost.

4. The dye should be soluble in a particular solvent for adsorption onto the electrode and should not be absorbed by the electrolyte.

The dye has to be stable for a long-term use. The current measure of stability is based on the number of cycles a cell will undergo in twenty years without decomposition. Also, the oxidized state of the dye must have a more positive potential than the redox couple in the electrolyte.

Early researchers in the field of sensitization used chlorophyll and other naturally occurring dyes as the sensitizer (Tributsch, 1971). Although quantum efficiencies of upto 10 % were achieved, the measured photocurrents were very small due to the small light harvesting efficiency of a dye monolayer. Today, the most widely used dyes are based on inorganic ruthenium compounds, such as $\text{RuL}_2(\text{NCS})_2$ or commonly known as N3, $\text{RuL}_2(\text{NCS})_2:2\text{TBA}$ (or N719), $\text{RuL}'(\text{NCS})_3:3\text{TBA}$ (black dye) and other derivatives. L_2 , and L' are *cis*-(dithiocyanato)-*N,N'*-*bis* (2,2'-bipyridine-4,4'-decarboxylate), *tris* (2,2'-bipyridine-4,4'-decarboxylate), and *cis*-tri(thiocyanato) *tris*(2,2',2''-terpydil-4,4',4''-tricarboxylate):3TBA ligands respectively. The three derivatives are shown in Figure 2.3.

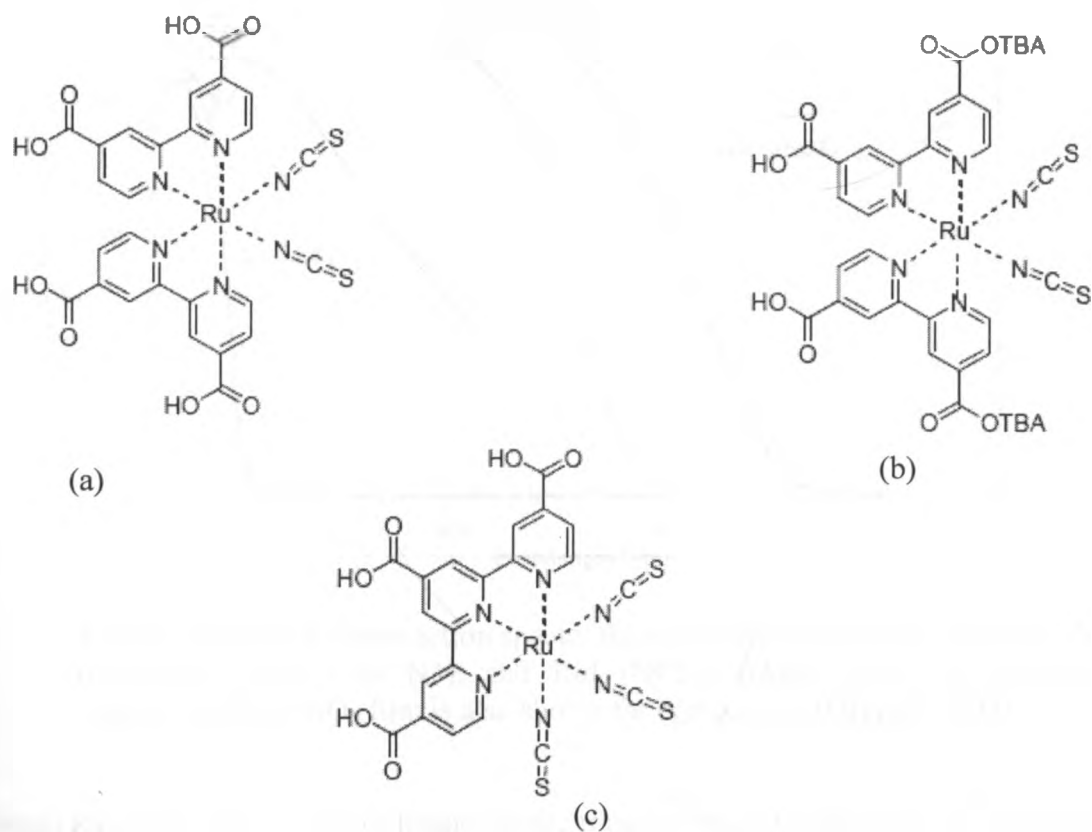


Figure 2.3: The structure of ruthenium (a) N3 dye (Grätzel, 2000; Nazeeruddin, *et al.*, 2001), (b) N719 and (c) Black dye (Grätzel, 2000; Nazeeruddin, *et al.*, 2001) complexes.

The first sensitizer for nanoporous TiO_2 electrodes was a trimeric ruthenium complex $\text{RuL}_2(\mu\text{-(CN)Ru(CN)L}'_2)_2$ dye (O'Regan and Grätzel, 1991) which was followed closely by the discovery of N3 dye in 1993 (Nazeeruddin, *et al.*, 1993) whose structure is shown Figure 2.3a.

The N3 dye complex exhibited a maximum incident-photon-to-current conversion (*IPCE*) efficiency at around 570 nm ($\text{RuL}_2(\text{NCS})_2$ in figure 2.4) but which drops below 40% at wavelengths above 700 nm.

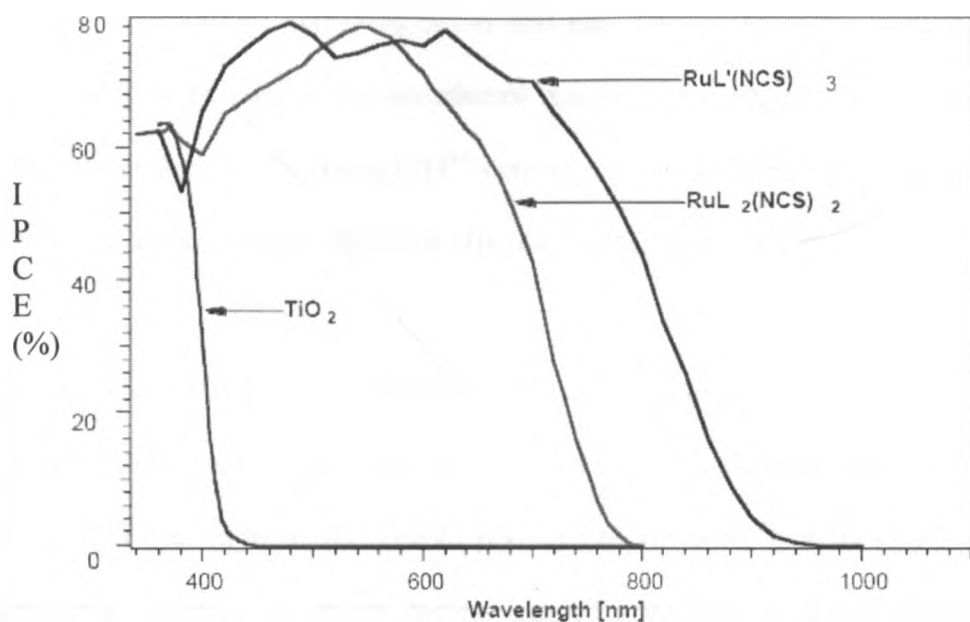


Figure 2.4: Photocurrent action spectra for ruthenium dye complexes: $\text{RuL}_2(\text{NCS})_2$ (commonly known as N3), and $\text{RuL}'(\text{NCS})_3$ (black dye). The photocurrent response of bare TiO_2 film is also shown for comparison (Grätzel, 2003).

Its optical transition has a metal-to-ligand charge transfer (MLCT) character, i.e., excitation of the dye involves transfer of an electron from the ruthenium metal to the π^* orbital of the surface anchoring carboxylated bipyridyl ligand from where it is released within femto- to picoseconds into the conduction band of TiO_2 generating electric charges with unit quantum yield (Grätzel, 2003). The N3 derivative of ruthenium exhibited outstanding sensitization properties and its photovoltaic performance has been unmatched for close to a decade by many other complexes and derivatives that have been synthesized and tested.

An improvement on the sensitizer was achieved by replacing one of the bipyridine ligands with thiocyanate yielding *cis*-(dithiocyanato)-*bis*(2,2'-bipyridyl-4,4'-dicarboxylate)-ruthenium II, also known as $\text{RuL}_2(\text{NCS})_2:2\text{TBA}$ ($\text{L} = 2,2'$ -bipyridyl-4,4'-dicarboxylic acid; $\text{TBA} =$ tetrabutylammonium) or N719 (Figure 2.3b) resulting to its *IPCE* maximum shifting to the

red with a strong shoulder extending up to 800 nm. The complex has a further advantage because it is able to be adsorbed from ethanol resulting in covalent binding of the carboxyl groups to coordinatively unsaturated Ti^{4+} centers on the TiO_2 . This has been reported to contribute to the higher electron injection efficiencies (Grätzel, 2001).

Many ruthenium complexes have been studied for sensitization but so far the black dye (figure 2.3c) has exhibited the best performance. This dye exhibits strong metal-to-ligand charge transfer (MLCT) transition in the visible part of the spectrum and its single excited state undergoes rapid deactivation to the lowest excited state due to the presence of a heavy ruthenium metal as the central frame, (Figure 2.3c). It has yielded $IPCE_{max}$ of close to 80 % at 650 nm with a shoulder extending above 40 % at wavelengths beyond 800 nm ($RuL'(NCS)_3$ in figure 2.4). The “black dye” has achieved record 10.4 % (AM 1.5) solar-to-electrical power conversion efficiency in full sunlight (Grätzel, 2001). This record has recently been broken only by using the N3 dye in conjunction with electron-rich 3, 4 ethylene dioxythiophene in its ligand increasing substantially the open-circuit voltage of the solar cell (Shi, *et. al.*, 2008). Many other complexes have been synthesized based on ruthenium as the base element (Nazeeruddin, *et. al.*, 2001).

Organic sensitizers have also been reported, such as polyene-diphenylaniline, (commonly known as D5) (Boschloo, *et. al.*, 2008) and indoline, known commercially as D149 (Ito, *et. al.*, 2006) dyes. These dyes have displayed efficient light harvesting and are promising sensitizers due to their shorter and simpler synthesis route. D5 has been found to be readily adsorbed on the mesoporous TiO_2 , giving a high $IPCE$ (72 % at 430 nm) due to its high extinction

coefficient ($33,000 \text{ M}^{-1} \text{ cm}^{-1}$ at 427 nm) (Boschloo, *et al.*, 2008). It has been proposed as good sensitizer for solid-state dye-sensitized solar cells because its triarylamine group favorably interacts with typical hole conducting materials, such as spiro-OMeTAD polymer, resulting in fast charge transfer.

Naturally occurring organic plant based dye pigments have also been studied as sensitizers (Cherapy, *et al.*, 1997; Deb, *et al.*, 1997; Tennakone, *et al.*, 1997; Smestad, 1998). CheraPy, *et al.* (1997) reported a dye sensitized TiO_2 cell utilizing flavanoid dye extract from berries. This device realized a solar light to electrical power efficiency of 0.56 % with photocurrent densities of $1.5 - 2.2 \text{ mA/cm}^2$ and V_{oc} of $0.4 - 0.5 \text{ V}$ under AM 1.5 illumination. Tennakone and coworkers reported the first isolated natural pigment of santalin from sandalwood and successfully used as sensitizer on TiO_2 . This attained 1.8 % solar energy conversion efficiency under 80 mW/cm^2 radiation (Tennakone, *et al.*, 1997).

Anthocyanin pigments (Figure 2.5) have been the front-runners in the natural organic pigments field due to their ability to perform sensitization without any synthesis. Anthocyanin pigment exists primarily in two states namely the quinoidal (acidic) and flavilium (basic in nature). Complexation studies on anthocyanin pigments have shown that the pigment chelates with metal ions of aluminum, iron, titanium and chromium (Cherapy, *et al.*, 1997 where the metal's ions compete with the dye's protons displacing them and hence shifting the anthocyanin equilibrium from quinoidal to flavilium state. The shift between the two chemical states corresponds to the shift in the absorption peak towards longer wavelengths that is observed on the absorption spectrum. A similar shift has been observed in blue-violet

anthocyanin extracts from calafate (Polo, *et. al.*, 2006). This was attributed to be as a result of alcoholic bound protons that condense with the hydroxyl groups present at the surface of nanostructured TiO₂ film stabilizing the dye's excited state.

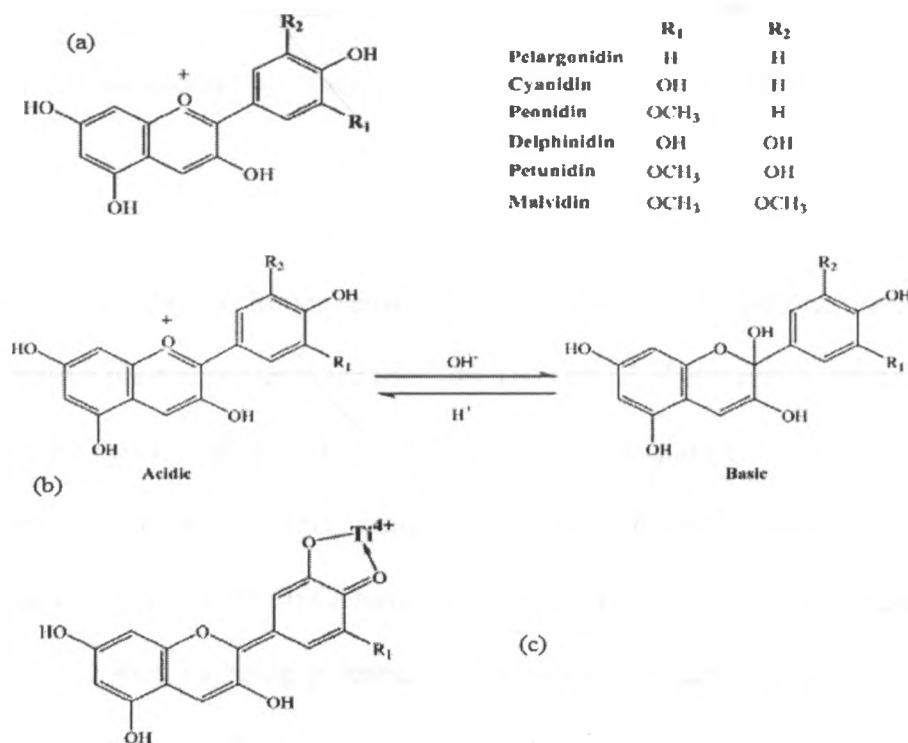


Figure 2.5: Chemical structures of the most abundant anthocyanidins. (a) basic (b) two chemical structures of anthocyanidins in acidic and basic media. (c) chelation mechanism of anthocyanidins with TiO₂ (Fernando and Senadeera, 2008).

Studies have shown that efficient sensitization requires an attaching group for the dye's adsorption on the semiconductor electrode surface acting as a bridge for electron injection (Andreas, 1994). This is because diffusion in these pigments is usually slow compared to its excited state lifetime hence a quick electron injection is required for efficient sensitization. The attaching problem was dealt with in synthetic sensitizers by Grätzel's group who developed carboxylic groups present in bipyridine ligands to perform the attaching function (Nazeerudin, *et. al.*, 1993) on the basis that the ligand provided a covalent bonding by a π -system

conjugating with the chromophore. It has been observed in anthocyanin pigments that hydroxyl groups present do not form chemical bonding with TiO_2 (Hao, *et. al.*, 2006). There is also the presence of long alkane chains of chlorophyll and carotenoid in some pigments that prevent the dye molecules from arraying on TiO_2 film efficiently. These two factors are responsible for the low absorption observed in sensitization using anthocyanin pigments.

Although highly efficient cells have been shown to operate with power conversions above 10 % using nanoporous TiO_2 electrodes sensitized with ruthenium complexes, there remains the need for alternative photosensitizers for use with TiO_2 -based photovoltaic devices. Therefore, investigation of low cost, readily available dyes as efficient sensitizers for DSCs still remains a scientific challenge. In this context, naturally occurring pigments such as anthocyanins, carotenoids and chlorophylls for DSCs have several advantages over rare metal complexes and other organic dyes, such as being potentially efficient (due to their close resemblance with photosynthesis in operation). Others are their availability, easy extraction into cheap organic solvents, application without further purification, broad absorption over the visible spectrum, environment-friendliness and considerably reduced cost of the devices.

Previous researches on anthocyanins as sensitizers have been concentrated on current – voltage characteristics and absorption properties. Though low overall conversion efficiencies have been reported in these pigments, to our knowledge, few have suggested the causes to the observation, instead have gone ahead to conclude that natural pigments can be used as alternative sensitizers. It is known that low efficiency observed in natural sensitizers is due to poor complexation between the dye and the semiconductor, but the change in absorption

characteristics when the pigment complexes with TiO_2 is not reported. Since anthocyanin pigments exist in the acid and basic states, the investigation of effect of pH on absorption characteristics has a direct link to the attaching ability of the pigment at different pH levels. It is in this context that we undertook to investigate the characteristics of anthocyanin dye pigment as the sensitizer for TiO_2 dye solar cell with emphasis on the attaching ability of the dye molecule on the TiO_2 semiconductor.

2.4 Efficiency Limiting Processes in DSC

There are several processes that have a direct effect on the performance of the dye solar cell as illustrated in Figure 2.6.

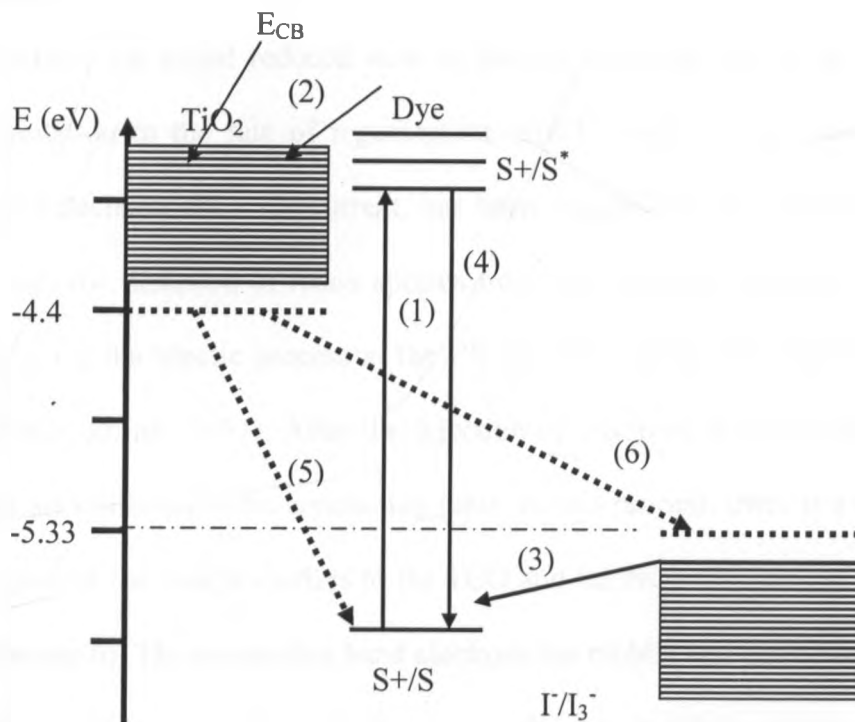


Figure 2.6: Principle of operation and energy level scheme of the dye-sensitized nanocrystalline solar cell showing the processes an electron goes through. The energy scale is versus the vacuum level (Ferber, *et. al.*, 1998).

The first step a cell goes through is light absorption (process 1 in Figure 2.6) where the dye layer absorbs photons from the solar spectrum. This depends on the absorption spectrum of the dye and it is directly related to the absorption efficiency, which is defined by the extinction coefficient, the concentration of the dye and the thickness of the film. Secondly electron injection into TiO_2 (process 2) occurs before the excited dye relaxes to its ground state (process 4), or recombines with electrons in the semiconductor or the redox couple (process 6). The efficiency of injection is given by the driving force in free energy and the orbital overlap between the excited state of the dye (S^*) and the conduction band of the TiO_2 surface. The dye gets oxidized (state S^+) after the electron injection and a charge separation is thereby achieved, resulting in a potential difference. In order for the dye to be able to absorb further photons and excite another electron, the initial reduced state of the dye molecule has to be regenerated (process 4). A limitation to the rate of regeneration, which would increase recombination reactions and hence decrease the photocurrent, has been suggested to be caused by several factors, such as the slow diffusion of redox species from the working electrode (WE) to the counter electrode (CE), the kinetic process at the CE and the regeneration kinetics from the redox species (Kuang, *et. al.*, 2007). After the injection of electrons into the semiconductor film, the electrons are collected at the conducting glass. In this process, there is a competition between the transport of the charge carriers to the TCO and the recombination of electrons to the electrolyte (process 6). The conduction band electrons are mobile and can be trapped in the semiconductor material due to defects or impurities. In the trapping model, there is an exchange of electrons between the conduction band level and the traps (Frank, *et. al.*, 2004). The assumption is normally that trapped electrons cannot recombine with the electrolyte's redox species and will therefore neither decrease nor increase the cell efficiency.

This competition between electron transport in the TiO_2 film and recombination with the redox electrolyte leads to the charge-collection efficiency, which is related to the diffusion coefficient (D) and the electron lifetime. This collection efficiency has an effect on the photocurrent produced by the device. The processes discussed above have been measured and found to have different time constants (Figure 2.7) and they compete and together have an impact on the overall efficiency of the cell (Grätzel, 2005).

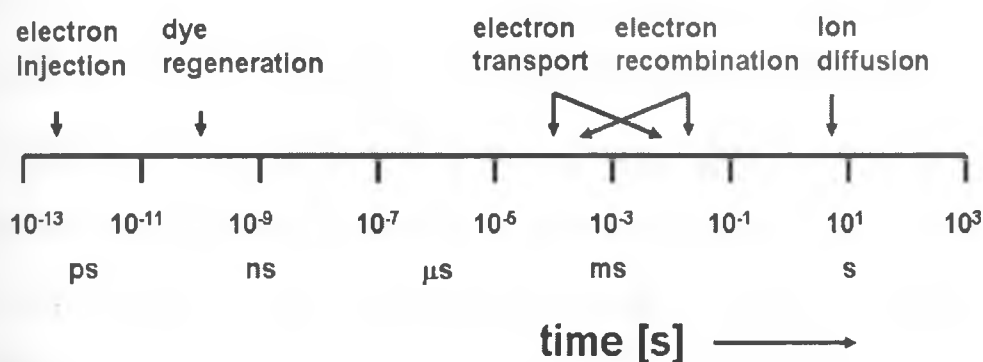


Figure 2.7: The dynamics of the processes in the DSC (Grätzel, 2005)

Electron transport and recombination go hand in hand and are among the most crucial processes in the operation of the solar cell and hence are discussed in detail. Electron transport in electrolyte filled nanoporous oxides has been extensively studied using intensity-modulated photocurrent spectroscopy (IMPS) (O'Regan, *et al.*, 1990; Cao, *et al.*, 1996; de Jongh and Vanmaekelbergh, 1996; de Jongh and Vanmaekelbergh, 1997; Dloczik, *et al.*, 1997; Schlichthorl, *et al.*, 1999; Peter and Wijayantha, 1999; de Jongh, *et al.*, 2000; Van de Lagemaat and Frank, 2000; Eppler, *et al.*, 2002; Yoshida, *et al.*, 2002; Kambe, *et al.*, 2002; O'Regan and Lenzmann, 2004) and time-of-flight (TOF) (Solbrand, *et al.*, 1997; Kopidakis,

et. al., 2000) techniques. The general consensus has been that electrons move through the nanoporous TiO₂ film by diffusion rather than by drift. This has been attributed to the high conductivity of the electrolyte in the pores supporting only a few millivolts of voltage drop under the relatively low current densities in normal sunshine conditions. It has also been held that, in standard electrolytes, electron diffusion in TiO₂ is the limiting charge-transport rate as opposed to ion diffusion in the electrolyte. From IMPS and TOF studies, the time constants for both are found to depend on light intensity, with increasing illumination intensity, decreasing the time constants. This decrease has been ascribed to trap filling. Because of the large surface area of the nanoporous films, these traps are assumed to be located primarily at the particle surface. Evidence for an exponential distribution of surface states has been obtained from intensity modulated photovoltage spectroscopy, (IMVS) (Schlichthorl, *et. al.*, 1997) and TOF (Nelson, 1999; Kopidakis, *et. al.*, 2000) measurements with low values of diffusion constants being attributed to electrons spending a large fraction of their transit time in traps.

There have been a number of routines that have been developed to study electron transport and recombination in DSCs, based on small amplitude perturbations of the illumination that are either periodic (IMPS or IMVS) (Schlichthorl, *et. al.*, 1997) or pulsed (Duffy, *et. al.*, 2000a). The perturbations are superimposed on a much larger steady state illumination component. Although small amplitude methods are powerful, they linearise the system response in a way that may obscure the transport mechanism and kinetics.

A charge extraction method was developed by Duffy's group to study the electron transport, trapping and back reaction of photogenerated electrons in DSCs (Duffy, *et. al.*, 2000b). This

was based on large amplitude technique that provided information about the mechanism and kinetics of the back reaction of electrons with tri-iodide species. It provides direct access to the electron density as a function of illumination intensity and decay time, such that the kinetics of the back reaction of electrons with tri-iodide species can be studied as well. The method was also found to allow a direct correlation to be made between the photovoltage and the total electron density, whose analysis leads to the density of states function for trapping states. The distribution functions obtained in this way have been used to model trap controlled electron transport in the nanocrystalline oxides (Peter, *et. al.*, 2002). The modeled results were compared with the intensity dependent behaviour revealed by small amplitude perturbation methods and showed consistency with the large amplitude responses.

Time-resolved photocurrent transients induced by laser pulse have also been used to study charge transport (Hagfeldt, 1995; Solbrand, *et. al.*, 1999; Van de Lagemaat and Frank, 2001; Nissfolk, *et. al.*, 2006). This was by excitation of the cell with monochromatic light of lower photon energy than the band gap energy of TiO_2 in order to ensure that only electrons injected from the dye contribute to the photocurrent. The laser pulse induced distribution of excited electrons was described by an exponential decay due to the absorption of the dye which enabled the diffusion equation to be solved numerically for this case. The charge transport was found to be highly dependent on the electrolyte composition with a high concentration of I_3^- giving a high photocurrent and addition of an inert salt raising the photocurrent amplitude (Solbrand, *et. al.*, 1999). In this study, analytical expressions describing electron transport in DSCs were derived and verified by the experimental studies. It was confirmed that the electron-transport rate in DSCs displays a nonlinear (power law) dependence on the electron

concentration which is attributed to the exponential distribution of surface states in the TiO₂ semiconductor.

Recombination studies on working solar cells have indicated that electron transport limits recombination with the redox electrolyte (Kopidakis, *et. al.*, 2003). A remarkable property of DSCs, which is key to their relatively high efficiency, is that recombination of photoinjected electrons with I₃ in the liquid electrolyte is extremely slow (Kopidakis, *et. al.*, 2003; Schlichthorl, 1997). Moreover, the rate of recombination depends nonlinearly on the electron concentration (Schlichthorl, *et. al.*, 1997; Schlichthorl, *et. al.*, 1999; Fisher, *et. al.*, 2000; O'Regan and Lenzmann, 2004) as in the case of the electron transport dynamics, which leads to an electron collection efficiency and electron diffusion length that are almost independent of light intensity (Fisher, *et. al.*, 2000). In the absence of redox species in the electrolyte, the recombination of photo-injected electrons takes place via the oxidized dye molecules instead of iodine and follows nonlinear kinetics, a phenomenon that has been attributed to transport-limited recombination in which transport is slowed by the presence of exponentially distributed traps. However, in a working DSC, incorporating a redox electrolyte, the recombination of photoinjected electrons with oxidized dye molecules is negligible except at high electron densities produced by very negative applied biases (Haque, 1998) or very high light intensities (Haque, *et. al.*, 2000).

Electron transport and recombination studies on DSC in working condition have yielded information regarding the Fermi level of the cell under working conditions (Nissfolk, *et. al.*, 2006). From these studies, it was observed that the electron lifetime was shorter in working

condition than in open circuit (OC) and further decreases with intensity. This was attributed to the fact that at open circuit conditions, electrons are approximately uniformly distributed in TiO₂ film giving a constant quasi-Fermi level (nE_f), but under operating conditions, there is a distribution in electron density and hence a gradient in nE_f is formed. Since electron lifetime is determined by nE_f , it is therefore less than that at open circuit (Nissfolk, *et. al.*, 2006). Electron transport studies in working condition on the other hand have shown an increase in nE_f with increase in biasing potential leading to an increase in effective diffusion coefficient. This was attributed to the multiple trapping (MT) model of electron transport in TiO₂ film. However, slow electron transport time observed with increased biasing is contrary to the MT model which predicts faster transport when nE_f is increased. This is still an area that is unresolved yet.

The concept of traps, *i.e.*, energy states below the conduction band, was introduced to explain the illumination intensity dependence of electron transport (de Jongh and Vanmaekelbergh, 1996; Dlockzik, *et. al.*, 1997; Van de Lagemaat and Frank, (2000); Kambili, *et. al.*, 2002; Nelson, *et. al.*, 2002; Frank, *et. al.*, 2004) Despite the fact that energy states below the conduction band have been found experimentally, the physical analogue of the exponential trap distribution remains under investigation. It has been suggested by many research groups that electron transport occurs predominantly in the conduction band, whereas most electrons reside in trap states. At first sight, this might seem to limit the performance of the DSC, but it has been estimated from the electron diffusion length, L , that the electron collection efficiency remains fairly constant over a broad illumination intensity range (Peter and Wijayantha, 1999).

While most of the studies on transport and recombination have been by IMPS and IMVS that are time consuming, in this study, we employ the time-resolved photocurrent and photovoltage transient techniques that are time-saving to study electron transport and back reactions incorporating a number of routines to compare the results. The routines are V_{oc} and I_{sc} vs intensities, short circuit photovoltage charge (Q_{sc}) vs intensity, short-circuit voltage V_{sc} , V_{oc} decay and transport time and lifetime measurements. These routines are carried out on varying film thickness to study the effect of film thickness on trap distribution and electron transport.

Chapter Three

Theoretical Background

3.1 Introduction

In this chapter, the theory underlying dye-sensitized solar cell's working and characterization is presented. In the first part the interface between a semiconductor and an electrolyte is presented, showing how the structure of the interface defines the relationship between charge and potential. The process of charge transfer at the interface is also presented. In the second part, the theory on various characterization techniques like X-Ray Diffraction (XRD), I - V characterization, photocurrent and photovoltage spectroscopy is also presented.

3.2 Semiconductor Electrochemistry

3.2.1 Semiconductor-electrolyte interface (SEI)

A semiconductor material consists of a valence band and a conduction band with the energy band gap separating the two. Semiconductors have a relatively small band gap which allows for the possibility of electrons jumping from the valence band to conduction band. Once in the conduction band, the electrons become free and conducting. An illustration of the differences between an insulator, semiconductor and metal is presented in figure 3.1.

In a semiconductor the Fermi-level for electrons is determined by the density of the conduction band electrons (n_c), and the effective density of conduction band states (N_c). The distribution of states in the conduction band is given by equation 3.1, i.e. (Sze, 1981),

$$N_e(E) = \frac{\sqrt{2}(m_{dos}^*)^{3/2}(E - E_c)^{1/2}}{\pi^2 \hbar^3} \quad (3.1)$$

where E is the energy of the state, E_c is the conduction band edge energy and m_{dos}^* is the effective mass of the electron.

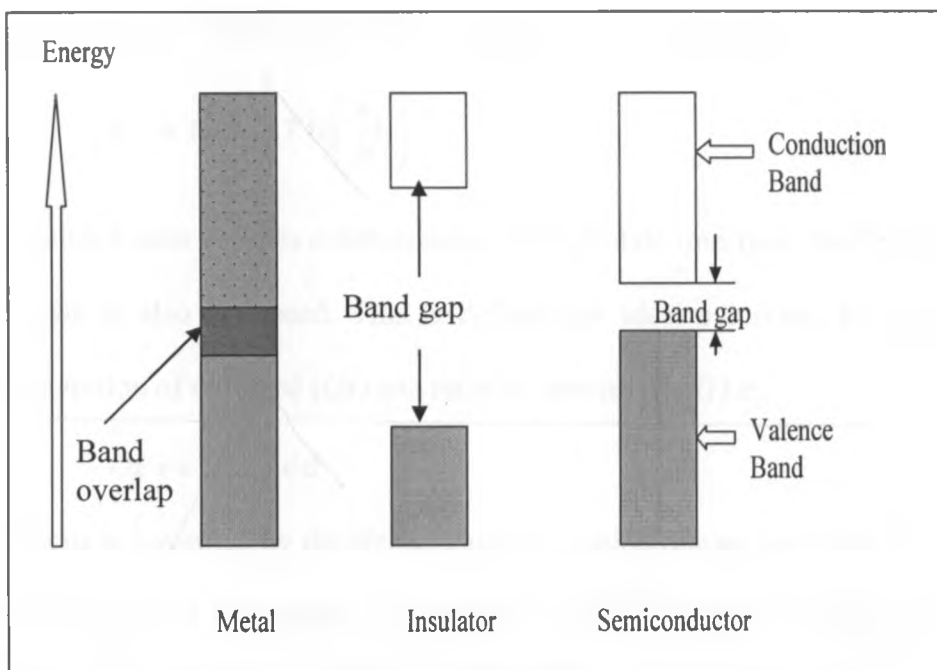


Figure 3.1: Energy levels for a metal, an insulator and a semiconductor.

The probability of an electron occupying an energy level E is given by the Fermi-Dirac distribution function (Shockely and Read, 1952; Sze, 1981),

$$f(E) = \frac{1}{1 + e^{(E-E_f)/k_B T}} \quad (3.2)$$

where E_f is the energy of the Fermi level. Integrating the product of equations (3.1) and (3.2) gives the density of the conduction band electrons in the semiconductor, i.e. (Shockely and Read, 1952),

$$n_c = \int_{E_c}^{\infty} N_c(E) f(E) dE = \frac{\sqrt{2}(m_{dos}^*)^{3/2}}{\pi^2 \hbar^3} \int_{E_c}^{\infty} \frac{(E - E_c)^{1/2}}{1 + e^{(E-E_f)/k_B T}} dE \quad (3.3)$$

For low densities, the unity in the Fermi function can be ignored, leading to

$$n_c = N_c e^{\frac{E_f - E_c}{k_B T}} \quad (3.4)$$

where N_c is the effective density of states. The energy of the Fermi level in the bulk semiconductor can therefore be determined from equation (3.4), giving

$$E_f = E_c + k_B T \ln\left(\frac{n_c}{N_c}\right) \quad (3.5)$$

Since the dye sensitized solar cell has a semiconductor-electrolyte interface, the Fermi level in the redox electrolyte is also discussed. This is defined for ideal solutions, by the relation between the concentration of oxidized (*Ox*) and reduced species (*Red*) i.e.,



This type of reactions is governed by the Nernst equation, which relates the Fermi level of the redox electrolyte, $E_{f, redox}$ with its reduced, C_{red} , and oxidized, C_{ox} , species in solution, given a standard electrode potential, E° (Bard and Faulkner, 2000), i.e.,

$$E_{f, redox} = E^\circ + k_B T \ln\left(\frac{C_{ox}}{C_{red}}\right) \quad (3.7)$$

The standard reference electrode usually used in electrochemical studies is the saturated calomel electrode (SCE), which is made up of Hg/Hg₂Cl₂/KCl saturated in water. Another common reference electrode is normal hydrogen electrode, commonly known as NHE. Subtracting (3.7) from (3.5) gives the difference in Fermi level between the semiconductor and the redox electrolyte which is related to a potential gradient referred to as the potential, V given by (Memming, 1980; Grätzel, 2005; Nissfolk, 2009),

$$V = \frac{E_f - E_{f, redox}}{e} \quad (3.8)$$

This is the thermodynamic driving force for electrons to have a net flux at the interface between the materials. This potential is also the V_{oc} of the cell when the cell is in open circuit mode and the maximum V_{oc} a cell can attain is determined by the difference between the Fermi

levels (i.e., the quasi Fermi level of the semiconductor and the redox potential of the electrolyte).

The processes that occur at the semiconductor/electrolyte interface (SEI) and in the bulk of electrolyte are mainly:

- (i) mass transfer processes which involve the movement of electrons under the influence of potential gradient,
- (ii) movement of redox species under the influence of concentration gradient and
- (iii) movement of fluids because of convections caused by density gradients.

These processes are summed up in the transport equation (Bard and Faulkner, 2000);

$$J_i(x) = -D_i \frac{\partial C_i(x)}{\partial x} - \frac{z_i F}{RT} D_i C_i \frac{\partial \phi(x)}{\partial x} + C_i v(x) \quad (3.9)$$

where $J_i(x)$ is the flux of species i ($\text{mol sec}^{-1} \text{cm}^{-2}$) at a distance x from the surface, D_i is the diffusion coefficient (cm^2/sec), $\partial C_i(x)/\partial x$ is the concentration gradient at a distance x , $\partial \phi(x)/\partial x$ is the potential gradient, z_i and C_i are the charge and concentration of species i , respectively, and $v(x)$ is the velocity (cm/sec) with which a volume element in solution moves along the axis. The three terms on the right hand side of equation (3.9) represent the contributions of diffusion, migration and convection, respectively, to the flux.

The common technique applied in the study of electrochemical processes is cyclic voltametry (CV) whose set up (figure 3.2) consists of a potentiostat and a cell that holds the analyte to be

studied. The cell consists of three electrodes namely the working (WE), reference electrode (RE) and counter electrode (CE).

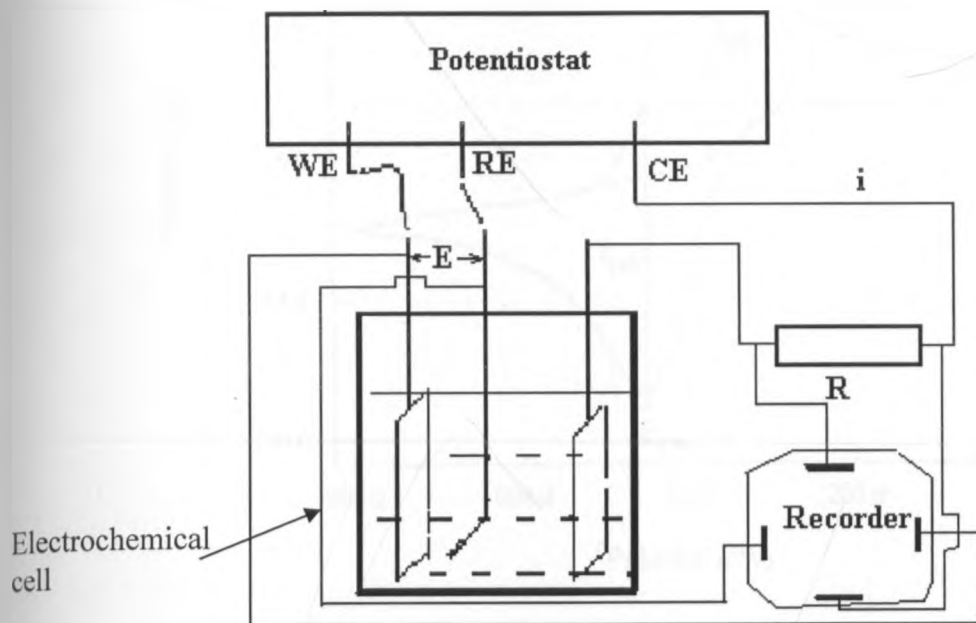


Figure 3.2: Electrochemical measurement system showing the working electrode (WE), reference electrode (RE) and counter electrode (CE).

The potential is applied between the WE and RE and the current flow is measured between the WE and CE. The working electrode provides the surface for electron transfer to occur for the system under investigation. The potential of the electrode (versus NHE via RE) is cyclically scanned typically with a rate of 1 – 100 mV/s between two end points and the resulting current is monitored. This way, it is possible to observe at which potential an electrochemical reaction occurs in terms of a current peak. A typical CV profile for a system whose concentration of species is described by the Nernst equation is shown in figure 3.3 with the important parameters labeled.

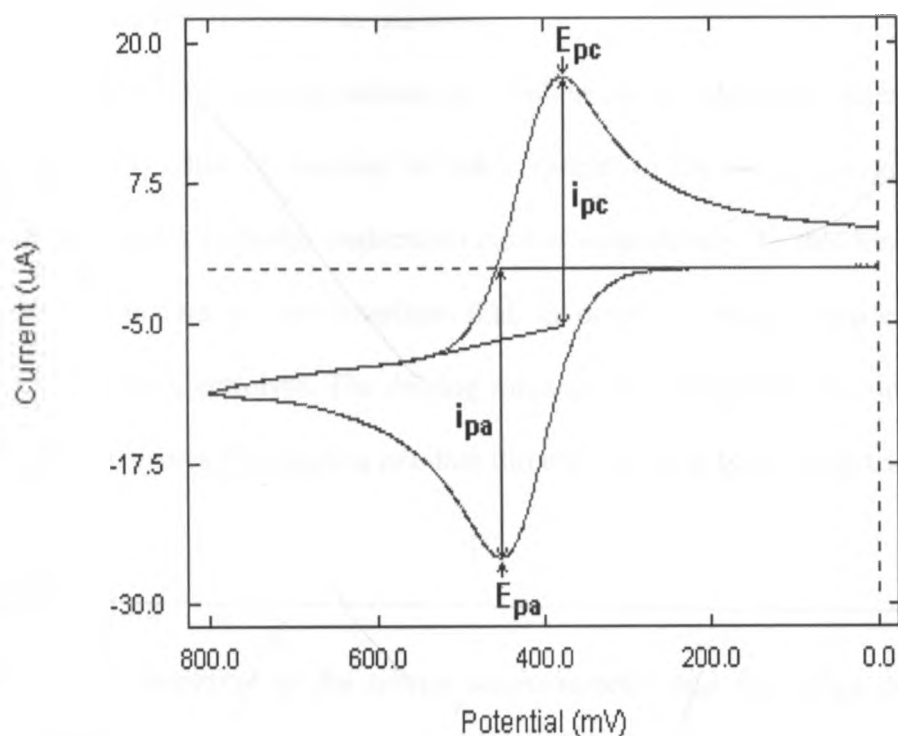


Figure 3.3: An ideal cyclic voltammogram for a reversible single electrode transfer reaction showing important peak parameters. E_{pc} and E_{pa} are cathodic and anodic peak potentials, respectively while i_{pc} and i_{pa} are cathodic and anodic peak currents respectively.

In order to derive the redox potential E° of the solution, an interpolation is made between the cathodic peak potential (E_{pc}) and the anodic peak potential (E_{pa}) which are oxidation and reduction peaks, respectively. Further information that can be derived from a cyclic voltammogram is the reversibility and kinetics of the system. There are various causes in electrochemical reactions that will result in a voltammogram being different from the typical one shown in figure 3.3. Among them are:

- (i) when the redox reaction is not reversible,
- (ii) when the reaction is slow due slow diffusion
- (iii) when there are several reactions going on simultaneously

3.2.2 Charge transfer processes at the SEI

Processes involving charge transfer across the semiconductor-electrolyte interface are in the form of oxidation or reduction reaction of redox species in the electrolyte giving rise to an anodic (oxidation) and a cathodic (reduction) current respectively. In this kind of process, a chemical reaction occurs at the interface that involves a charge transfer between the semiconductor and the electrolyte. The driving force for the charge net flow at the SEI is the bias potential which drives the reaction in either direction leading to a charge transfer process.

3.2.3 Band bending

The Fermi-level of electrons in the n-type semiconductor and the redox potential in the electrolyte are same between the semiconductor and the electrolyte at equilibrium (figure 3.4).

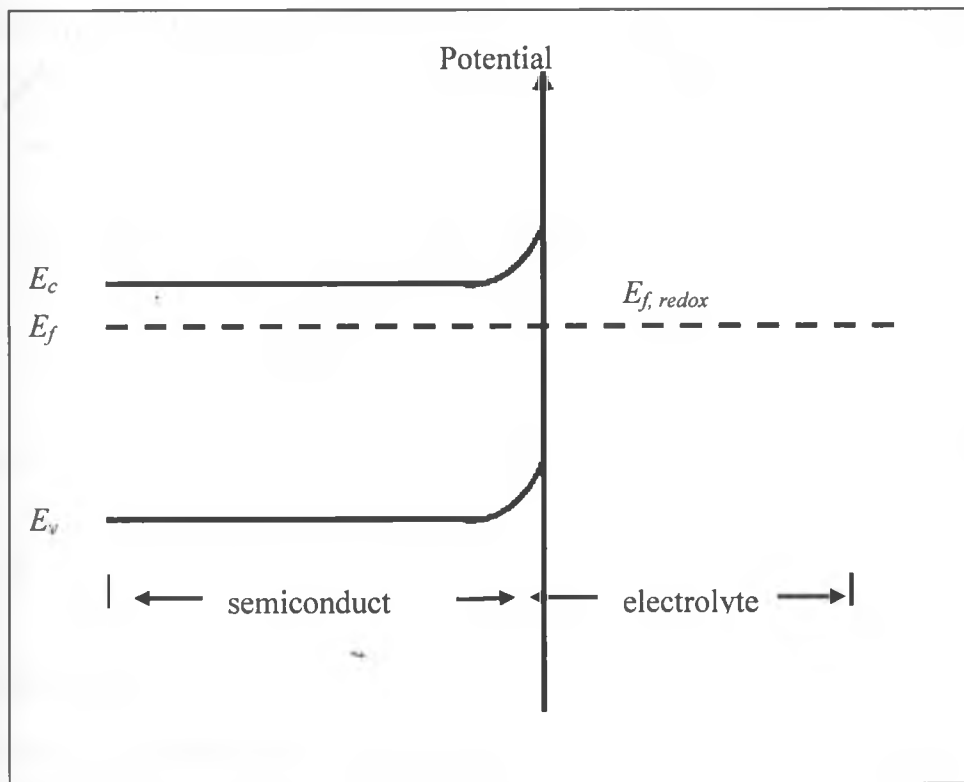


Figure 3.4: Band bending at the semiconductor-electrolyte interface for n-type semiconductor (Memming, 1980).

At equilibrium, electrons can be transferred from the semiconductor to the electrolyte by diffusion process. This leads to a build-up in an electric field at the SEI, forming a depletion layer which prevents a further transfer of electrons to the electrolyte. The energy of the electrons close to the semiconductor-electrolyte contact is affected by the electrical field in the depletion layer, with those close to the interface having a stronger effect, a condition that leads to band bending (figure 3.4), (Memming, 1980; Södergren, *et. al.*, 1994).

At the Fermi level, E_f , the depletion layer disappears leading to flat-band potential. For nanometer size particles, the distances are too short within the particle for the depletion to build up hence a constant potential within the particle is assumed. The potential distribution for a spherical particle was first solved by Albery and Bartlett (1984) who estimated the total band bending for small particles of radius r , by

$$\Delta\phi_{sc} = \frac{k_B T}{6e} \left(\frac{r}{L_D} \right)^2 \quad (3.10)$$

where e is the electron charge. L_D is the Debye length given by

$$L_D = \sqrt{\frac{\epsilon\epsilon_0 k_B T}{2e^2 N_D}} \quad (3.11)$$

where ϵ_0 is the permittivity in free space and ϵ is the dielectric property and N_D is the donor density.

3.2.4 Dye sensitization

For a non-sensitized photoelectrochemical solar cell (discussed above), electrons are excited from the valence band to the conduction band when light is absorbed in the semiconductor creating electron-hole pairs. The absorbed light energy is converted to electrical energy when

the generated charges are separated at the SEI. However, in the case of dye sensitized solar cell, charge carriers are not generated by band gap excitation but by electron (or hole) injection from the excited dye. The energy scheme and its working principle are described in figure 3.5.

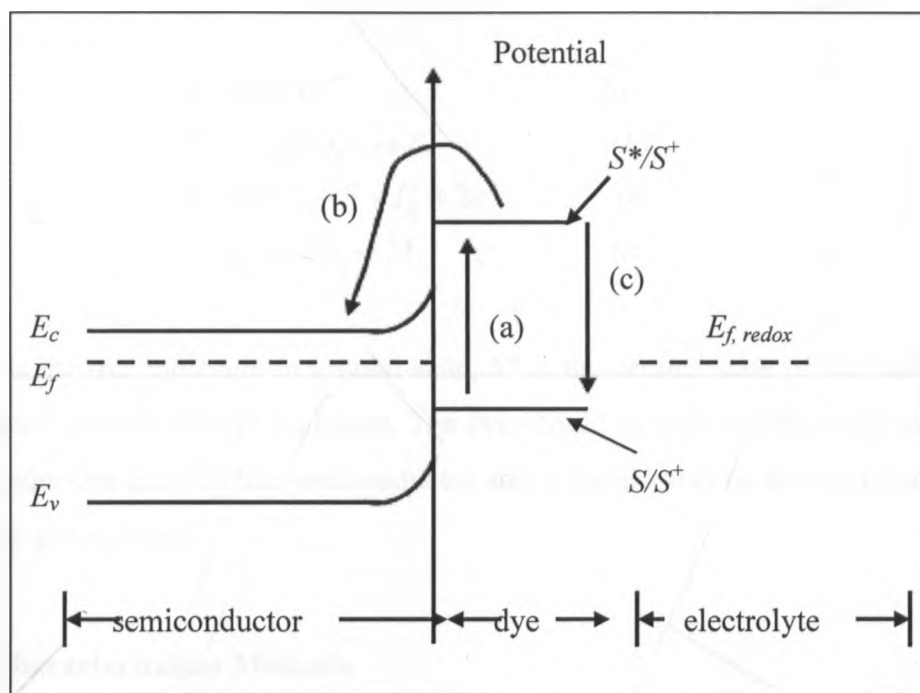
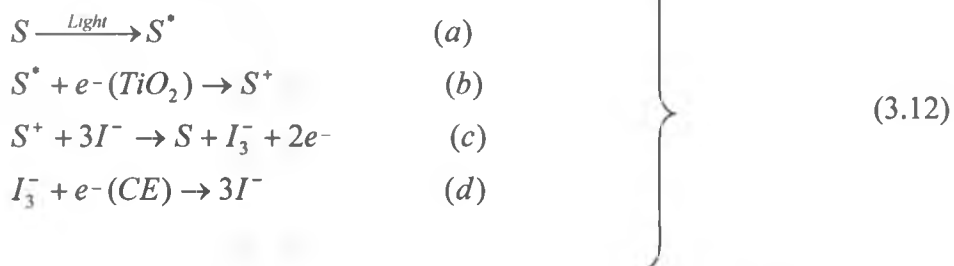


Figure 3.5: Semiconductor-electrolyte interface when the electrode is dye sensitized and under illumination

In the case of n-type semiconductor (for example TiO_2), upon illumination, the dye gets excited from its ground state S to S^* (reaction (a) in figure 3.5 and equation 3.12a). In the excited state S^* , the dye molecule injects an electron into the conduction band of TiO_2 (reaction (b) and equation 3.12b) and in the process it gets oxidized (S^+). The dye molecule's oxidized state is reduced to ground state (reaction (c) and equation 3.12c) by the redox couple present in the electrolyte through the process of accepting the electron from the counter electrode.

Reaction (b) takes place if the dye is in close contact with the semiconductor surface during the excited state lifetime and also if the dye lies energetically above the conduction band of the semiconductor. The chemical reaction processes discussed above are summarized in equation (3.12):



where S is the dye molecule in ground state, S^* is the excited state of the molecule and S^+ is the oxidized state of the dye molecule. The dye should be able to efficiently inject an electron in the conduction band of the semiconductor and it should also be able to be regenerated by I^- back to its ground state.

3.3 Characterization Methods

3.3.1 X-ray photoelectron spectroscopy (XPS)

In XPS, electrons are emitted from the sample as a response to incoming x-ray photons as illustrated in figure 3.6. The electrons acquire enough energy from the photons to enable them escape from the atom and its environment. If the energy of the electron is well defined ($h\nu$), the kinetic energy of the emitted electron (E_K) can be used to determine the electron binding energy, E_B^V via the photoelectric effect law (Verma, 2007):

$$E_K = h\nu - E_B^V \quad (3.13)$$

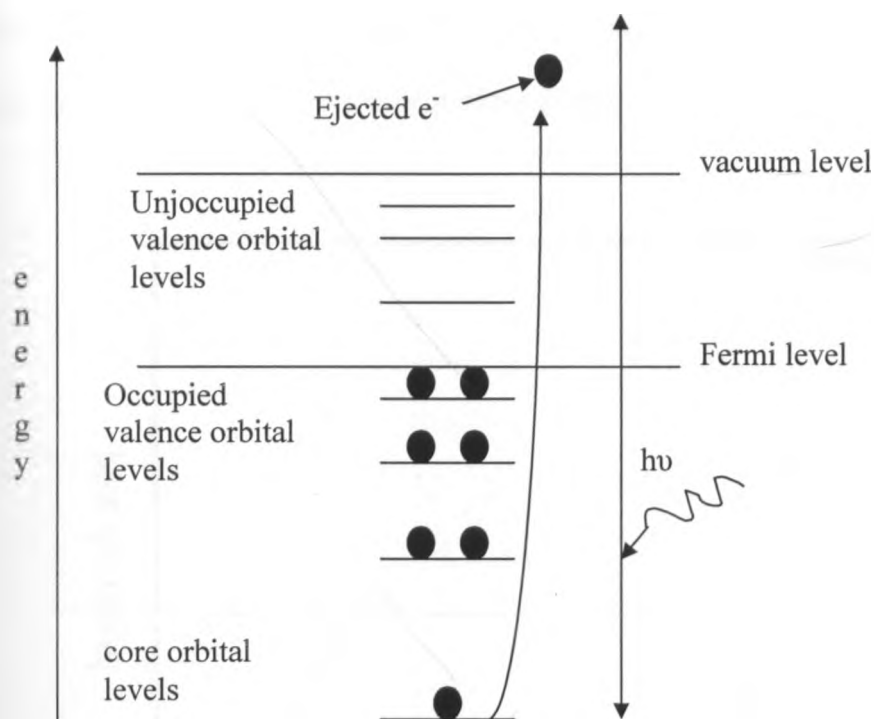


Figure 3.6: An illustration showing x-ray photons with enough energy to remove the core electrons of a material, i.e., to lift them energetically above the vacuum level (Verma, 2007).

With the knowledge of the electron binding energy, one can map all the occupied electronic levels reachable with the photon energy used, from the innermost core orbital to the outermost valence orbital. From equation (3.13), the intensity of the emitted electrons is plotted as a function of the binding energy resulting in a spectrum similar to the one presented in figure 3.7. Since the binding energies of core levels are not involved in molecular or solid state bonding, they are always atom specific and as such these energies can be used to make elemental compositional analysis of the sample. The core levels however, vary in binding energy depending on the chemical environment (also known as chemical shift). The chemical shift may be explained in terms of the changes in electrostatic potential of the core orbital upon

chemical changes. On this basis therefore, the chemical shifts provide information on the oxidation state and chemical environment of the atoms.

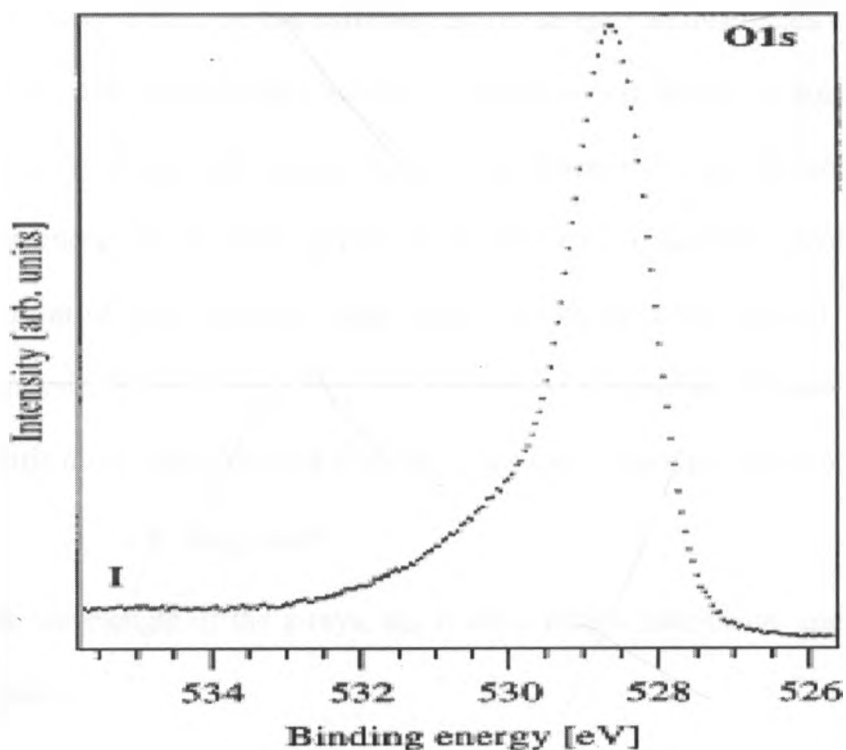


Figure 3.7: Typical XPS spectra showing characteristic O1s core level peak in TiO_2 (Rensmo, *et. al.*, 1999).

The system used in XPS studies consists of an x-ray source of specific wavelength incident on a sample and a detector that detects the emitted photoelectrons. The electrons are emitted from the atom in all directions and they undergo inelastic collision inside the chamber. Before being detected the electrons are focused by an electron lens system and then dispersed in terms of kinetic energy by a hemispherical electrostatic analyzer.

3.3.2 X-ray diffraction (XRD).

X-rays are high energy electromagnetic radiation, having energies ranging from about 200 eV to 1 MeV. X-rays are produced in an x-ray tube consisting of two electrodes in a vacuum chamber. If an incident electron has sufficient energy to eject an inner-shell electron, the atom will be left in an excited state with a hole in the electron shell. When the hole is filled from an outer shell, an x-ray photon with energy equal to the difference in the electron energy levels is produced. The energy of the x-ray photon is characteristic of the target material and will be displayed in form of high intensity peaks (known as characteristic peaks) that are used for diffraction analysis. When these x-rays are focused on a material, they get scattered by the atoms in specific directions according to Bragg's law (Suryanarayana and Norton, 1998):

$$\lambda = 2nd_{hkl} \sin \theta \quad (3.14)$$

where λ is the wavelength of the x-rays, d_{hkl} is the crystal's inter-planar spacing and θ is the angle of incidence.

Equation (3.14) is used in the analysis of the diffraction patterns of sample material and hence is used for elemental identification and also the kind of crystal orientation. The diffraction pattern of the sample is obtained by plotting the peak intensity on the y-axis and the measured diffraction angle (2θ) on the x-axis. A typical x-ray diffraction pattern is shown in figure 3.8.

The diffraction pattern consists of a series of peaks which corresponds to x-rays diffracted from a specific set of planes in the specimen. The pattern shown in figure 3.8 is the powder diffraction file (PDF) standard from the reference library for Barium Titanate (Remel, *et al.*, 1999). The positions of peaks depend on the crystal structure (shape and size of the unit cell) of the material that enables the determination of structure and lattice parameter of the

material. The actual patterns obtained may vary slightly from the standard ones and the main variation arises from the peak broadening that is mainly caused by the size of the crystal and the overlapping of peaks.

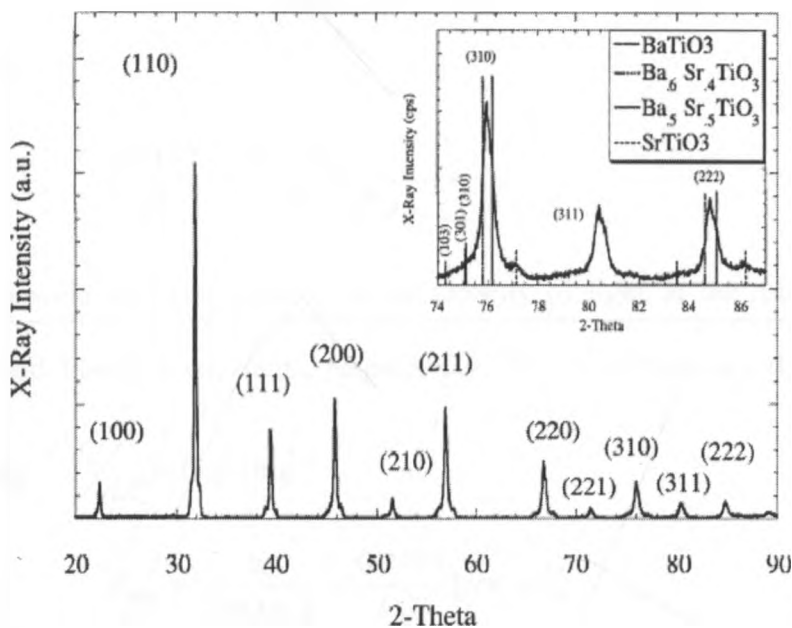


Figure 3.8: A typical XRD pattern of barium titanate (Remel, *et. al.*, 1999).

Apart from identifying peaks, XRD also gives information about the crystal sizes of the samples. This is determined from the Scherer's formula given by (Suryanarayana and Norton, 1998)

$$Crystal\ size = \frac{180}{\pi} \frac{\kappa \lambda}{\cos \sqrt{(FWHM)^2 - S_i^2}} \quad (3.15)$$

where κ is the Scherer constant ($= 0.89$), this is the ratio between full width at half maximum ($FWHM$) and integral breadth, S_i is the instrument broadening (assumed to be $= 0$), λ is the wavelength of the incident radiation (which is equal to 1.54 \AA for the instrument used).

3.3.3 Current-voltage (*I-V*) characterization

Solar energy consists of an electromagnetic spectrum of different wavelengths ranging from ultraviolet (*UV*), visible and infra red regions. From the theory of blackbody radiation, the energy density per wavelength, $\frac{de_r}{d\lambda}$, can be expressed as a function of wavelength (λ) as (Würfel, 2005),

$$\frac{de_r(\lambda)}{d\lambda} = \frac{2hc_0 d\Omega}{d\lambda} \frac{1}{e^{\frac{hc}{\lambda k_B T}} - 1} \quad (3.16)$$

where $d\Omega$ is a solid angle element, c is the velocity of light in the medium, k_B and h are Boltzmann's and Planck's constants, respectively. The maximum density per wavelength is

found by taking $\frac{d^2 e_r}{d\lambda^2} = 0$ giving

$$\lambda_{\max} = \frac{hc}{4965k_B T} = \frac{0.2497}{k_B T} [\mu m, eV] \quad (3.17)$$

The power density at the sun's surface is 62 MWm^{-2} and it reduces to 1353 Wm^{-2} just outside the earth's atmosphere. On passing through the atmosphere, the spectrum is partially attenuated by the absorption of O_2 , Ozone, water vapor, CO_2 and methane. This attenuation is described by the 'Air Mass' (AM) factor since the absorption increases with the mass of air through which radiation passes. AM is given by the ratio l/l_0 where l_0 is the thickness of the atmosphere, l is the path length through which the radiation passes at an incident angle α relative to the earth's surface normal. Therefore l is given by

$$l = l_0 / \cos \alpha \quad (3.18)$$

The spectrum outside the atmosphere is AM0 and that on the earth's surface for perpendicular incidence is AM1. The standard spectrum for moderate weather is AM1.5, which corresponds

to a solar incident angle of 48° relative to the surface normal, giving a mean irradiance of 1000 Wm^{-2} .

I - V measurement determines the current-voltage response of the device, i.e., I - V characteristics in the dark and under different light intensities. In the dark, the solar cell device is modeled as an ideal diode where the applied voltage (known as bias voltage) on the device generates current in the direction opposite to that of light generated current. This current is known as dark current and is given by (Sze, 1981)

$$I_{\text{dark}} = I_s \left(\exp\left(\frac{eV}{kT}\right) - 1 \right) \quad (3.19)$$

where I_s is the saturation current, V is the applied voltage and e is the elementary charge.

Under illumination, the I - V characteristics are of the form:

$$\begin{aligned} I &= I_{ph} - I_s \left(\exp\left(\frac{eV}{kT}\right) - 1 \right) \\ &= I_{ph} - I_s \left(\exp\left(\frac{V}{V_T}\right) - 1 \right) \end{aligned} \quad (3.20)$$

where I_{ph} is the photo-generated current and V_T is the thermal voltage ($= k_B T / e$).

For non-ideal devices, the ideality factor, m is used to describe the dependence of dark current on voltage, giving the equation (Nelson, 2003),

$$I = I_{ph} - I_s \left(\exp\left(\frac{V}{mV_T}\right) - 1 \right) \quad (3.21)$$

Equation 3.21 can be obtained experimentally by plotting photocurrent as a function of applied bias resulting in a typical curve known as the current- voltage (I - V) characteristics curve (Figure 3.9).

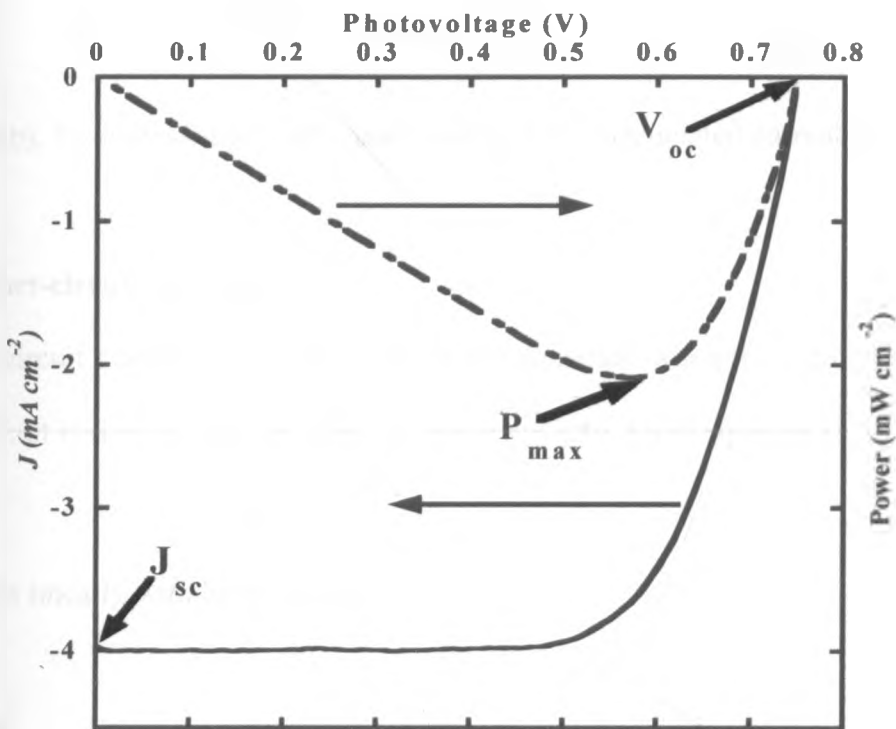


Figure 3.9: A typical I - V curve showing variation of current with voltage and corresponding power curve (Nelson, 2010).

From the I - V curve, important parameters namely open circuit photovoltage (V_{oc}), short circuit photocurrent (I_{sc}), fill factor (FF) and overall conversion efficiency can be determined.

3.3.3.1 Open-circuit voltage (V_{oc})

V_{oc} is measured under the condition when the circuit is open (external load is infinite and zero power). In this state, there is no external current flow between the two terminals, i.e. $I = 0$ and $V = V_{oc}$. From equation (3.21), V_{oc} can hence be determined by (Nelson, 2003),

$$I_{ph} - I_s \left(e^{V_{oc}/mV_T} - 1 \right) = 0 \quad (3.21a)$$

$$V_{oc} = mV_T \ln \left(\frac{I_{ph}}{I_s} + 1 \right) \equiv mV_T \ln \left(\frac{I_{ph}}{I_s} \right) \quad (3.22b)$$

From (3.21b), V_{oc} increases logarithmically with the photogenerated current and light intensity.

3.3.3.2 Short-circuit current (I_{sc})

The short-circuit current (I_{sc}) is measured at the condition when the applied voltage is zero, i.e., the circuit is shorted, and the load and power are zero. From equation (3.22a),

$$I_{sc} \equiv I_{ph} \quad (3.23)$$

I_{sc} increases linearly with light intensity.

3.3.3.3 Fill factor (FF)

The output power from the solar cell is the product of photocurrent and the applied voltage. At short-circuit and open-circuit the output power is zero, which is the case in which no external work can be performed. At a certain potential between short-circuit and open circuit, a maximum output power (P_{max}), will appear, (figure 3.9), where the device delivers the highest power output with the voltage, V_{mp} and the current I_{mp}

$$V_{mp} = V_{oc} - mV_T \ln \left(\frac{V_{mp}}{V_T} + 1 \right) \quad (3.24)$$

FF is defined as the ratio

$$FF = \frac{V_{mp} I_{mp}}{V_{oc} I_{sc}} \quad (3.25)$$

which describes how the maximum power rectangle fits under the I - V characteristics. A combination of equations (3.24) and (3.25) gives the approximation for FF as in equation (3.26).

$$FF = \frac{V_{oc}/mV_T - \ln\left(1 + V_{oc}/mV_T\right)}{1 + V_{oc}/mV_T} \quad (3.26)$$

Typical FF values for DSC range from 0.6 to 0.8 depending on the device. Generally the FF is influenced by the series resistance (R_s) arising from the internal resistance and resistive contacts of the cell, and shunt resistance (R_{sh}) arising from the leakage of current. Figure 3.10 shows an equivalent circuit for a solar cell showing R_s and R_{sh} .

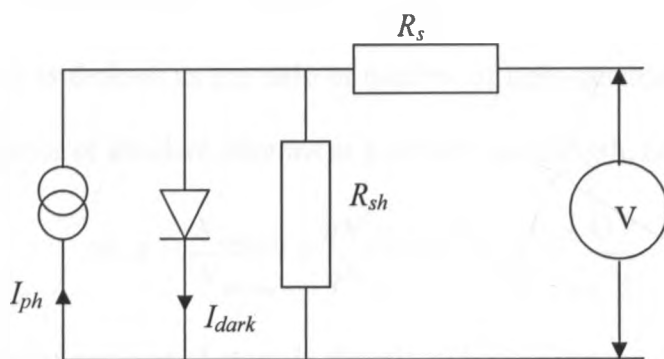


Figure 3.10: An equivalent circuit for a solar cell showing the series (R_s) and shunt (R_{sh}) resistances

3.3.3.4 Solar-to-electric power conversion efficiency (η)

This is a parameter that is associated with the overall performance of the device. This is defined as the ratio of the maximum power (P_{max}) to the power of incident radiation (P_{in}). It is given by

$$\eta = \frac{V_m I_m}{P_{in}} = \frac{V_{oc} I_{sc} FF}{P_{in}} \times 100\% \quad (3.27)$$

P_{in} is set to standard test condition at AM1.5 spectrum illumination and incident power density of 100 mWcm^{-2} at 298 K.

3.3.4 Incident photon to current conversion efficiency (IPCE) characterization

IPCE which stands for incident photon-to-current conversion efficiency and it helps in the analysis of the efficiency of a solar cell's conversion of light with a specific wavelength to a photocurrent. It can be performed under monochromatic light in which the photocurrent is measured for each wavelength. Generally, the IPCE can be expressed as the product of the absorption (η_{abs}), injection (η_{inj}) and collection efficiencies (η_{coll}).

Experimentally, it is defined as the ratio of number of light-generated electrons in the external circuit to the number of incident photons at a certain wavelength, i.e.,

$$IPCE = \frac{N_{electron}}{N_{photon}} = \frac{qN_{electrons}/s}{qN_{photons}/s} = \frac{I_{ph}(A)}{qN_{photon}/s} \quad (3.28)$$

The rate of arrival of incident photons is directly related to the incident power as follows

$$P_{in}(Watt) = P_{in} \left(\frac{\text{Joule}}{s} \right) = \frac{N_{photon}}{s} h\nu = \frac{N_{photon}}{s} \frac{hc}{\lambda} \quad (3.29)$$

With Equation (3.29), (3.28) can then be written as

$$IPCE = \frac{I_{ph}}{\frac{qP_{in}\lambda}{hc}} = \frac{I_{ph}}{P_{in}} \frac{hc}{q\lambda} = \frac{I_{ph}}{P_{in}} \times \frac{1240}{\lambda(nm)} \times 100\% \quad (3.30)$$

For dye sensitized solar cells the customary expression is

$$IPCE(\%) = \frac{1240J_{sc}(mAcm^{-2})}{\lambda(nm)P_{in}(mWcm^{-2})} \times 100\% \quad (3.31)$$

J_{sc} is the short circuit photocurrent density (measured by a source meter), λ is the wavelength of incident light, (obtained from the lamp that is set at a particular wavelength by the monochromator) and P_m is the incident radiation at a particular wavelength (obtained by an optical power meter and a detector). A plot of equation (3.31) gives a graph of *IPCE* (%) at different wavelengths (λ). The process of obtaining *IPCE* can be automated through various steps using a data acquisition and instrument control software (see appendix II for program) or manually obtained.

3.4 Charge Transport and Recombination

Charge transport and recombination studies are done by electron transport and lifetime measurements respectively. Lifetime measurement helps to analyze the recombination process in the DSC. Both electron transport and lifetime studies can be performed by applying a small square light modulation under a bias illumination giving a response similar to one in figure 3.11. The response (photocurrent or photovoltage) profile follows the square wave light modulation (lines with dots in figure 3.11) from which the amplitude (which is ΔJ or ΔV) and response time (which is transport time, t_{tr} or recombination time, t_{rec}) of the transient, is calculated. For photovoltage transient, the response time is attributed to the electron lifetime (which is also recombination time rate t_{rec}) of the system. This is highly dependent on the bias illumination level and therefore on the open circuit voltage.

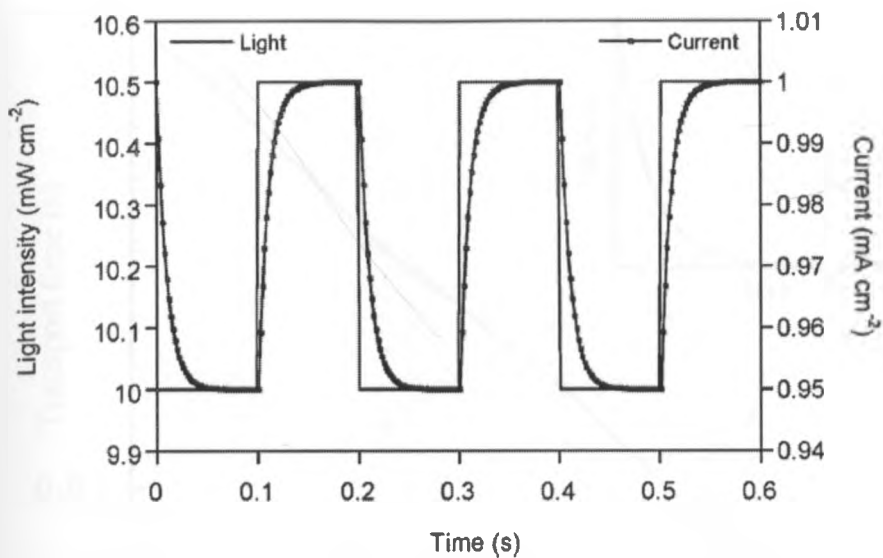


Figure 3.11: The photocurrent response to a small-amplitude square waveform perturbation. The solid line is the square pulse while the dotted line is the response (Boschloo, *et. al.*, 2006).

Electron transport measurement is performed in order to analyze the conduction of electrons in the porous semiconductor. The measurement is performed during a modulation of the light under a bias light condition and while recording the photocurrent response. Normally, the measurement is performed in short circuit mode. The perturbations are performed with a frequency resolved method, intensity modulated photocurrent spectroscopy.

The photocurrent responses for both methods are analyzed to estimate a transport time. Typical photocurrent transients and the resulting transport time are shown in figure 3.12.

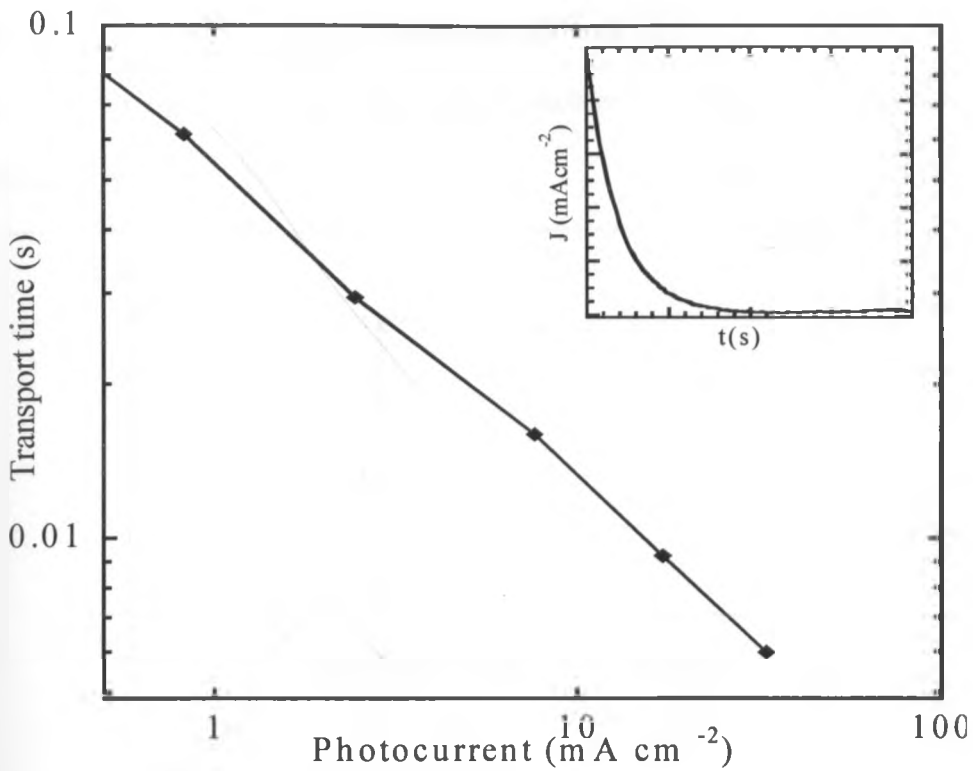


Figure 3.12: Typical responses showing transport time plotted as a function of photocurrent. Inset is the photocurrent decay for a single bias intensity (Boschloo, *et. al.*, 2006).

Photocurrent transients (inset of figure 3.12) and their corresponding transport times have similar profiles like for photovoltage but the difference is their magnitudes. To obtain information about transport and recombination, the current and voltage responses are fitted to first order exponential functions as expressed in equations (3.32) and (3.33), respectively (Van de Lagemaat and Frank, 2001) to give the profile in figure 3.12.

$$J_{sc} = J_{sc,0} + \Delta J e^{-\frac{t}{t_{tr}}} \quad (3.32)$$

$$V_{oc} = V_{oc,0} + \Delta V e^{-\frac{t}{t_{rec}}} \quad (3.33)$$

The constants $J_{sc,0}$ and $V_{oc,0}$ represent V_{oc} and J_{sc} without modulations, ΔJ and ΔV are the modulation magnitudes, and t_{tr} and t_{rec} the time constants for transport and recombination,

respectively. Normally, only one time constant is seen and this is related to the transport time or lifetime. Consider figure 3.13 showing typical photocurrent decay from a single value of modulation intensity.

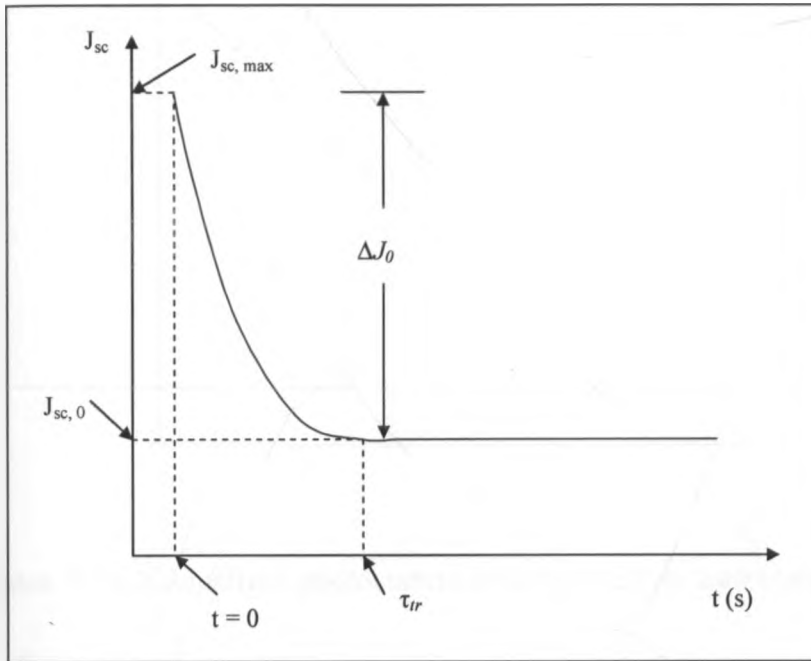


Figure 3.13: A sketch of photocurrent decay for one value of modulation intensity.

The time constants of the electron transport times and lifetimes are plotted against the photocurrent at different bias light intensities on a logarithmic scale giving a straight line for both transport time and lifetime. The decay follows the model presented in equation (3.32) with the parameters present indicated on the sketch. Transport time constant (t_{tr}) is approximated to be the time just at the onset of constant current density and ΔJ_0 being the difference between the initial transient current ($J_{sc,max}$) and the constant current (offset current, $J_{sc,0}$). To obtain a fit to the above transient, equation (3.32) is linearised and invoking initial conditions leads to the normalized current transient equation (3.34),

$$\ln\left(\frac{\Delta J}{\Delta J_0}\right) = -\frac{t}{t_{tr}} \quad (3.34)$$

whose plot on a semi logarithmic scale gives a linear plot of the form shown in figure 3.14.

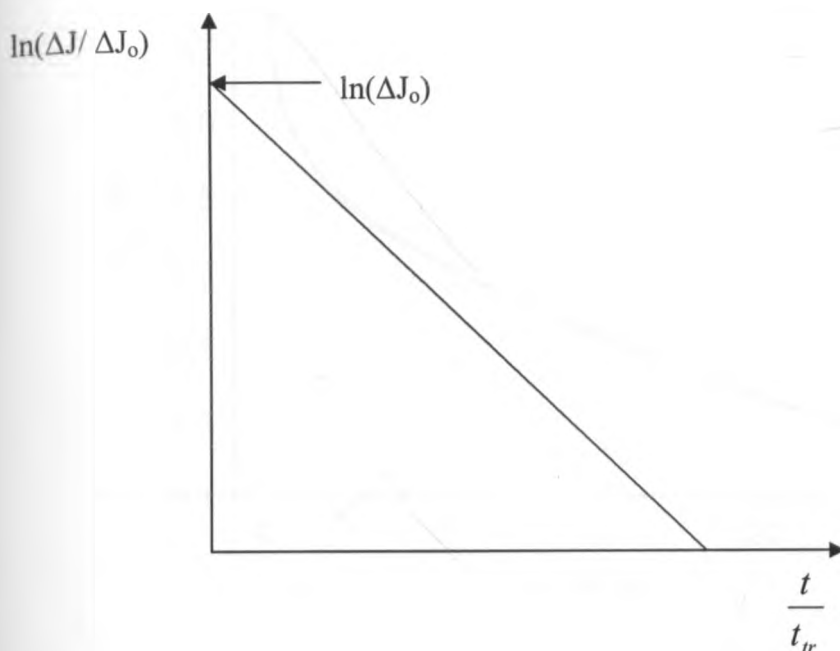


Figure 3.14: Normalized photocurrent decay plotted on logarithmic scale.

From the sketch, information about the kind of transport that takes place in the electrode can be obtained, i.e., whether the decay has a single exponential or more.

3.4.1 Photovoltage decay

The voltage decay analysis provides information about the electron recombination processes in DSCs. When the cell is illuminated in open circuit mode for some time then switched to the dark, the decay follows the profile shown in figure 3.15.

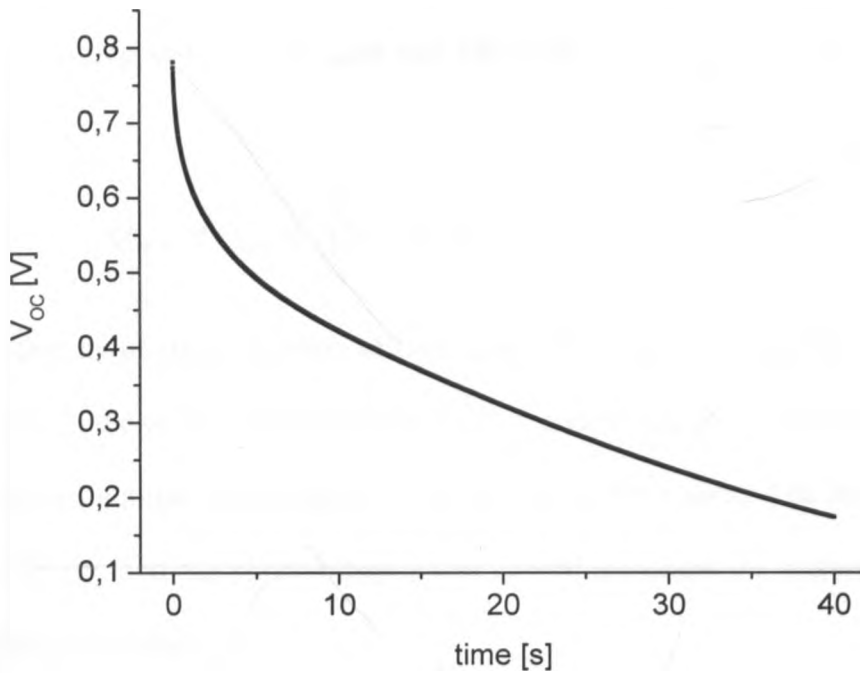


Figure 3.15: V_{oc} decay with respect to elapsed time in the dark.

Since no current is extracted, the decrease in V_{oc} can only be attributed to recombination processes in the cell. Therefore the electron lifetime t_e in the semiconductor (e.g. TiO_2) can be determined using the following relation (Zaban, *et. al.*, 2003):

$$t_e = -\frac{k_B T}{e} \left(\frac{dV_{OC}}{dt} \right)^{-1} \quad (3.35)$$

where k_B is boltzmann's constant, T is temperature and the rest bear their usual meanings.

3.4.2 Charge extraction

When the cell is illuminated while in open circuit mode, it reaches a point when a steady state is arrived, i.e. a point where the rates of photogeneration and back reaction of electrons with tri-iodide are equal. If the illumination is interrupted at this point, and the electron density allowed to decay for a given time in the dark before short circuiting the cell, then the current

measured will correspond to the remaining charge in the film. This method can offer information on the trap states in the solar cell where the charge is given by (Duffy, *et. al.*, 2000a)

$$Q_{photo} = Q_{trap} = \int_{E_f}^{nE_f} N_{trap}(E) dE \quad (3.35)$$

$N_{trap}(E)$ is the density of states function of traps ($\text{cm}^{-3} \text{ eV}^{-1}$), E_f is the equilibrium dark Fermi level of electrons in the oxide, determined by the Γ_3/Γ couple and nE_f is the quasi Fermi level of electrons under illumination. Equation (3.35) also provides a direct link between the total stored charge density and the photovoltage under conditions where the majority of electrons are located in trapping states.

3.4.3 Electrochemical potential characterization

When a solar cell is illuminated for a short time while it is in short circuit mode then followed with switching simultaneously to open circuit and in dark, the voltage rises to a maximum value after a certain time, t_{max} then slowly decays to zero. The maximum voltage that is reached, hereafter referred to as the maximum short-circuit voltage ($V_{sc, max}$), is related to the charge that is left in the nanostructured semiconductor. The value of $V_{sc, max}$ gives an indication of the position of the quasi-Fermi level inside the nanostructured TiO_2 film. Typical results are shown in figure 3.16.

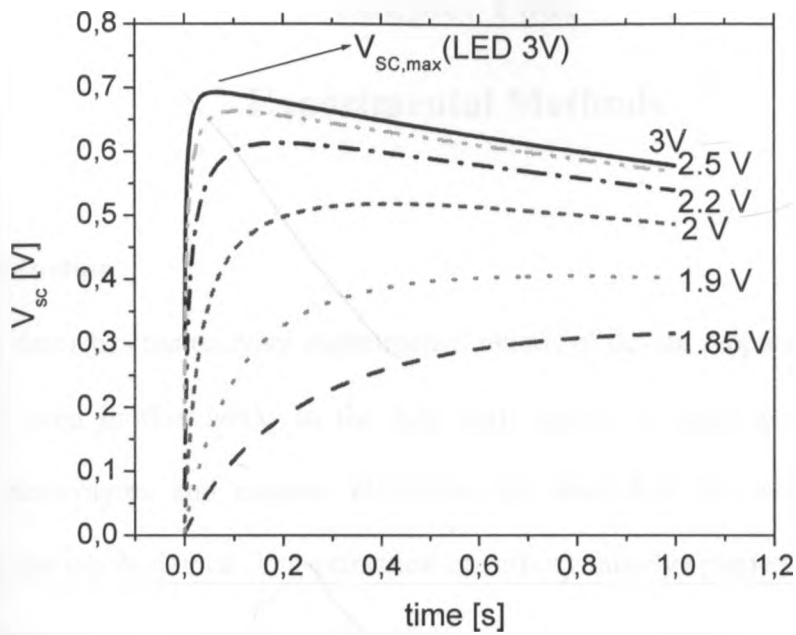


Figure 3.16: A sketch of internal voltage decay (V_{sc}) at different diode bias illumination (Boschloo, *et. al.*, 2006).

As t_{max} corresponds to the time required to obtain a uniform distribution of the electrons in the film (assuming that recombination occurs uniformly in the film), it can be considered as a transport time (Boschloo, *et. al.*, 2006).

Chapter Four

Experimental Methods

4.1 Introduction

This chapter describes the relevant experimental details of device preparation, characterization and analysis used in this work. In the first part, details of glass substrates, TiO₂ pastes, sensitizers, electrolytes and counter electrodes are described, as well as the assembling procedure of the whole device. The extraction of anthocyanin dye pigment is also discussed, as well as preparation of ruthenium dye complex. In the second part, setups of spectroscopic methods such as x-ray photoelectron spectroscopy (XPS) and SEM, current-voltage characterization, *IPCE*, electrochemical measurements, photo-transient voltage and current decay experiments, are explained. All reagents and solvents used in this work were of analytical grade and were supplied by Sigma Aldrich unless stated otherwise, ruthenium complex dyes were acquired from Solaronix SA, Switzerland. The F:SnO₂ conducting glasses used as substrates for photo and counter electrodes were TEC 8 from Pilkington Inc, USA coated with fluorine doped tin oxide (sheet resistance = 8 Ω/cm²). The solar cells used to study current-voltage characteristics for anthocyanin dye pigment had 6.5 μm film thickness and exposed area of 0.48 cm² while the ones used to study film thickness related electron transport had 3.0 μm, 6.0 μm, 12.8 μm, 23.5 μm and 25.3 μm film thicknesses and exposed area of 0.48 cm².

4.2 Sample Preparation

4.2.1 Dye preparation

The anthocyanin dye pigment was extracted from *viola odorata* (common name sweet violet) flower in ethanol/water (at ratio 1:1) at room temperature. The solid residues were filtered out and the natural dye pigments concentrated by a rotary evaporator at 40 °C. The extract was then dried over magnesium sulphate to form pellets. The pellets were then centrifuged at a rate of 1800 rpm for 15 minutes at room temperature then dissolved in 10% acetonitrile, 0.1% TFA eluent. Ruthenium complex dye was prepared by dissolving 0.0315g of cis-di(thiocyanato)bis((2,2'-bipyridyl-4,4'- decarboxylate)-ruthenium II (commonly known as N719) complex in 50 ml 99.5 % ethanol. The resulting dye solution of 0.5 mM concentration was stirred for 3 hours and kept in a cool dark place ready for dye sensitization.

4.2.2 Dye characterization

Anthocyanin dye pigment was characterized using Metrohm 654 pH meter (Metrohm, Switzerland) calibrated with buffer 1 (pH 4.5) and buffer 2 (pH 9.0) for dissociation characteristics. The dye's pH was increased by addition of 10.0 µl, 0.01M dropwise as the pH was read off from the pH meter. To obtain the dye's pH below 2.50, 10.0 µl of concentrated hydrochloric acid was introduced in the dye as the pH was monitored.

The dye's absorption characteristics were studied using UV-Vis spectrophotometer at wavelengths 400 nm to 800 nm. The absorption characteristics were recorded for anthocyanin dye in solution and also for photoelectrodes sensitized with anthocyanin pigment at different pH levels. The empty cuvette was used as a reference for studies on dyes in solution while the

unsensitized TiO₂ photoelectrode was used as reference for the dye sensitized film. In both cases, the respective spectra recorded were subtracted from the reference spectra.

4.2.3 TiO₂ paste preparation

The materials for preparation of TiO₂ paste were P25 (30 nm by Brunauer-Emmett-Teller (BET), 80% anatase (d = 21 nm) and 20% rutile (d = 50 nm)) from Degussa AG, Germany, ethyl cellulose (5 – 15 mPas at 5% in Toluene:Ethanol/80:20 at 25°C).

6.0 g of P25 Degussa was mixed with 1.0 ml acetic acid and ground in a mortar for five minutes. This was followed by addition of 5.0 ml de-ionized water dropwise while grinding in a mortar for another five minutes. 30.0 ml of ethanol was then added in steps of 5.0 ml with continuous grinding and finally 100.0 ml of ethanol added. The paste was transferred to a 250.0 ml beaker then stirred for 2 minutes followed by sonication using Branson model 240 Digital Sonicator horn, (Branson Ultrasonics Corp, USA) and stirred again for another 2 minutes. The colloid in ethanol was then mixed with 20.0 g of tarpineol and followed by further stirring – sonication – stirring process. The same process was repeated after addition of 10% ethyl cellulose (Fluka GmbH, Germany) in ethanol to the colloid and then concentrated in a rotor vapour and collected in a reagent bottle. The resulting paste of about 21% by weight of TiO₂ was run through a three-roll miller and collected in a bottle.

4.2.4 Thin film deposition

The TiO₂ paste was used to coat films on F:SnO₂ conducting glass substrate by screen printing method. The mesh size was 6x8 mm and one frame had 20 mesh openings that gave a total of

20 films at a single coating. To coat subsequent layers, the coated film was heated at a temperature of 150 °C for five minutes and left to cool to room temperature then another coat applied until the required number of coatings was achieved. The films were then sintered in air for one hour at 450 °C and left to cool to room temperature. The film thicknesses were determined by Alpha Step 200 surface profilometer (Tencor Instruments Inc, USA). These films were either used for XRD, SEM and XPS analysis or assembled into complete solar cells for *I-V*, and transport/recombination analysis, after determining the film thickness.

4.2.5 Counter-electrode preparation

Pre-drilled F:SnO₂ conducting glass substrates were cut into 1.5 x 1.5 cm sizes and cleaned in the ultrasonic bath using ethanol, water and acetone for 10 minutes in each following that order. The cleaned glass substrates were then dried in hot air gun for 30 minutes at a temperature of 400 °C and cooled to room temperature. 10.0 μl/cm² of 4.8 mM hexachloroplatinic acid (H₂PtCl₆) in ethanol was spread on the conducting side of the glass substrate and heated again in a hot air gun for 30 minutes at a temperature of 400 °C. The counter electrodes were then cooled in air before using them.

4.2.6 Electrolyte preparation

The electrolyte used in this study is composed of 0.5 M tetrabutyl ammonium iodide (TBA-I), 0.5 M 4-tert-butyl pyridine (4-TBPy), 0.1 M lithium iodide and 0.1 M iodine dissolved in 3-methoxypropionitrile (3-MPN), also known as the standard electrolyte. The electrolyte was prepared as follows: 0.069 g lithium iodide, 1.108 g TBA-I, 0.369g TBPy and 0.126 g of iodine crystals were weighed using a high precision analytical balance and transferred in a

dark bottle in that order. 5ml of 3-MPN was used to dissolve the mixture to make the required concentration which was followed by stirring for 3 hours. The electrolyte was then stored at room temperature and used when needed.

4.2.7 Complete solar cell assembly

TiO₂ coated films that were used for dye sensitization were cooled to 80 °C after sintering and then immersed in the dye (anthocyanin or ruthenium complex) that was at room temperature, for 12 hours. The samples were subsequently rinsed in acetonitrile, dried briefly on a hot plate and then thermally fused together with 25 µm thick thermoplastic surlyn frame (Dupont Inc, USA) on a hot plate. The electrolyte was introduced through the holes on the counter electrode by applying a few drops using a micropipette until the electrolyte was completely filled inside the cell. The cell was then placed in a vacuum sealed bell jar followed by air extraction leaving the electrolyte only in the cell. The cell was removed from the bell jar and the excess electrolyte wiped away and further sealed with surlyn and microscope cover glass. Silver contact paint was finally applied on the edges of the working and counter electrodes to offer less resistance contact for the solar cells.

4.3 Thin Film Characterization

4.3.1 Scanning electron microscopy (SEM)

SEM was used to study the morphological characteristics of the films. This was done using Carl ZeissTM LEO 1550 scanning electron microscope with Gemini column at 20kV electron source. The SEM micrographs were taken using a CCD (charged coupled device) camera

interfaced to a computer. Different micrographs were taken at different magnifications that ranged from X10,000 to X200,000.

4.3.2 X-Ray Diffraction (XRD)

X-ray diffraction was obtained by means of Siemens D5000 Diffractometer (Bruker AXS GmbH, Germany) with θ - 2θ parallel beam geometry. The range was from 10° to 80° with detector type of scan at a scan speed of $0.6^\circ/\text{min}$ and step size of 0.01° . The stage was set to rotate at 15 rotations per minute. XRD peak references were obtained from International Centre for Diffraction Data, USA.

4.3.3 X-Ray Photoelectron spectroscopy (XPS)

XPS spectra were recorded using Quantum 2000 scanning ESCA μ -probe (Physical Electronics Inc., USA) with Al K_α x-ray source with photon energy of 1486.6 eV. The equipment uses a rotating anode high power x-ray source and a quartz crystal monochromator delivering Al K_α radiation. The instrument has a 300 mm radius hemispherical electron energy analyzer and a swift sample transport system from air to ultra high vacuum chamber.

4.4. Solar Cell Characterization

4.4.1 *I-V* characterization

Current-voltage (*I-V*) characteristics were obtained using a set up (Figure 4.1) consisting of Newport solar simulator model 91160 (Oriel Instruments, USA) that was set to give an irradiation of $100 \text{ mW}/\text{cm}^2$ (equivalent of one sun at AM 1.5) at the surface of the solar cells. All the solar cells characterized in this work had an active area of 0.48 cm^2 . A dark frame was

placed on the solar cell sample to ensure that only the solar cell's active area was illuminated. The current-voltage characteristics under these conditions were obtained by applying an external potential bias to the cell and measuring the generated current with a Keithley 2400 digital source meter (Keithley, USA).

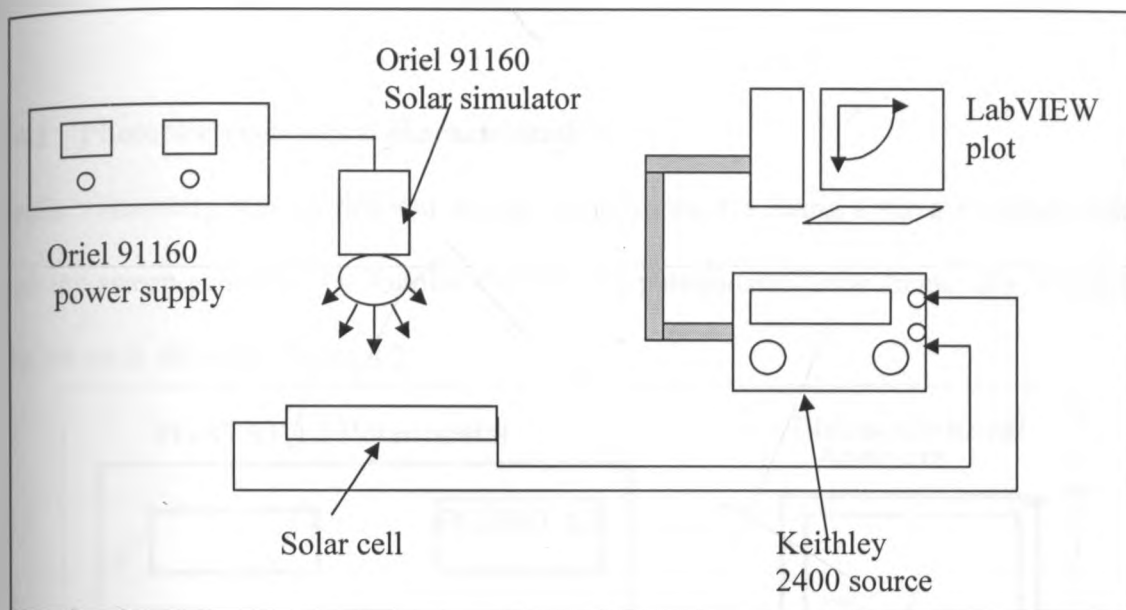


Figure 4.1: Block diagram of the current-voltage characterization set up.

The solar cell's cathode (working electrode) and anode (counter electrode) were connected to the negative and positive terminals of the Keithley 2400 source meter respectively, which was connected to the computer via GPIB interface. The bias was from short circuit to open circuit and was obtained automatically using LabVIEW™ software from National Instruments Inc, USA (see appendix I for details on automation in LabVIEW). From the data, an *I-V* curve was plotted in real time and the parameters V_{oc} , J_{sc} , FF , P_{max} and η were calculated and displayed automatically and saved as an excel file. *I-V* characteristics for anthocyanin dye sensitized solar cells were obtained for films sensitized with the dye pigment at pH 1.80, 2.00, 5.17 and

8.34 and all were $6.5 \pm 0.5 \mu\text{m}$ film thickness. $I-V$ characteristics for anthocyanin sensitized solar cells and ruthenium N719 sensitized solar cells were compared using cells of film thickness $3.0 \mu\text{m}$ and 0.48cm^2 exposed area. For thickness dependent $I-V$ characteristics, $I-V$ was recorded for solar cells at varying film thicknesses of $3.0 \mu\text{m}$, $6.0 \mu\text{m}$, $12.8 \mu\text{m}$, $23.5 \mu\text{m}$ and $25.3 \mu\text{m}$ film thicknesses and sensitized with ruthenium N719 dye.

4.4.2 Photoelectrochemical characterization

Cyclic voltametry was carried out on the anthocyanin dye using a three-electrode cell setup with the sweep generated by Autolab PGSTAT12 potentiostat (Echochemie BV, Netherlands).

The set up is shown in figure 4.2.

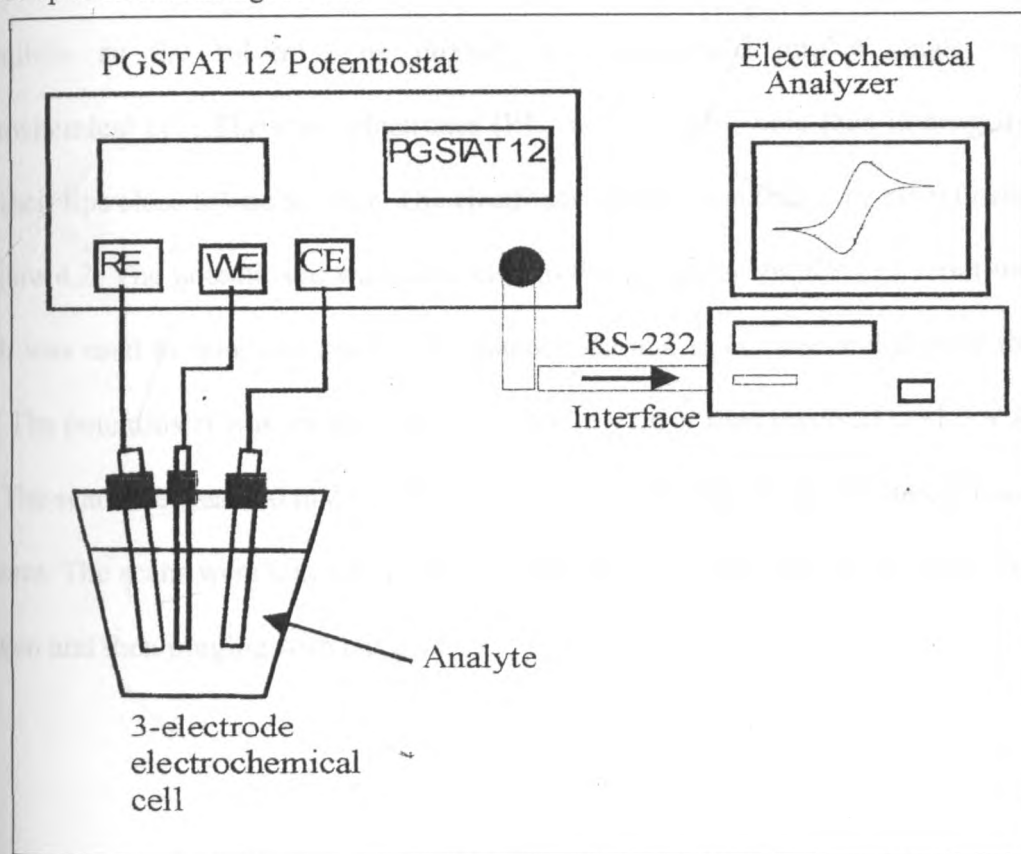


Figure 4.2: Set up for cyclic voltametry (CV) studies. RE is reference electrode, WE is the working electrode and CE is the counter electrode.

The electrodes were silver/silver chloride reference electrode, glassy carbon working electrode and platinum counter electrode. The base solvent was acetonitrile with lithium iodide salt to provide the ions. Before the study was done on the dye, the potentiostat was calibrated by using the dummy cell used in place of the electrochemical cell. The dummy cell has three electrodes (WE, RE and CE) which were connected to the potentiostat and a test run taken. Thereafter the electrodes to be used in the experiment were rinsed in de-ionized water and a calibration run done using ferrocene. Ferrocene was dissolved in acetonitrile and used as the analyte with the three electrodes immersed in the single compartment electrochemical cell in the positions indicated in figure 4.2. The resulting scan was compared with the standard scan. Anthocyanin dye pigment was then mixed with 0.1 M LiI as the supporting electrolyte in acetonitrile as the solvent. The mixture was transferred into a single compartment electrochemical cell. The three electrodes (RE, WE and CE) were then immersed in the cell with their tips close to one another. The electrodes were connected to the potentiostat as shown in figure 4.2. The potentiostat was connected to the computer via RS 232 serial interface bus which was used to remotely control the potentiostat and to analyze and display the resulting scan. The potentiostat was set to sweep from 0 V to +1.6 V then reversed to -1.5 V and back to 0 V. The scan rate was 200 mV/s and the voltamogram plotted by the electrochemical analyzer software. The scans were taken in various conditions beginning with steady state, purging with nitrogen and then purging with oxygen.

4.4.3 Incident Photon-to-Current conversion Efficiency (*IPCE*).

IPCE was measured using a set up consisting of a white light source, ARC SpectraPro 150 monochromator (Princeton Instruments), Oriel OPM 70310 optical power meter (Oriel Instruments) and collimators (schematic set up shown in figure 4.3).

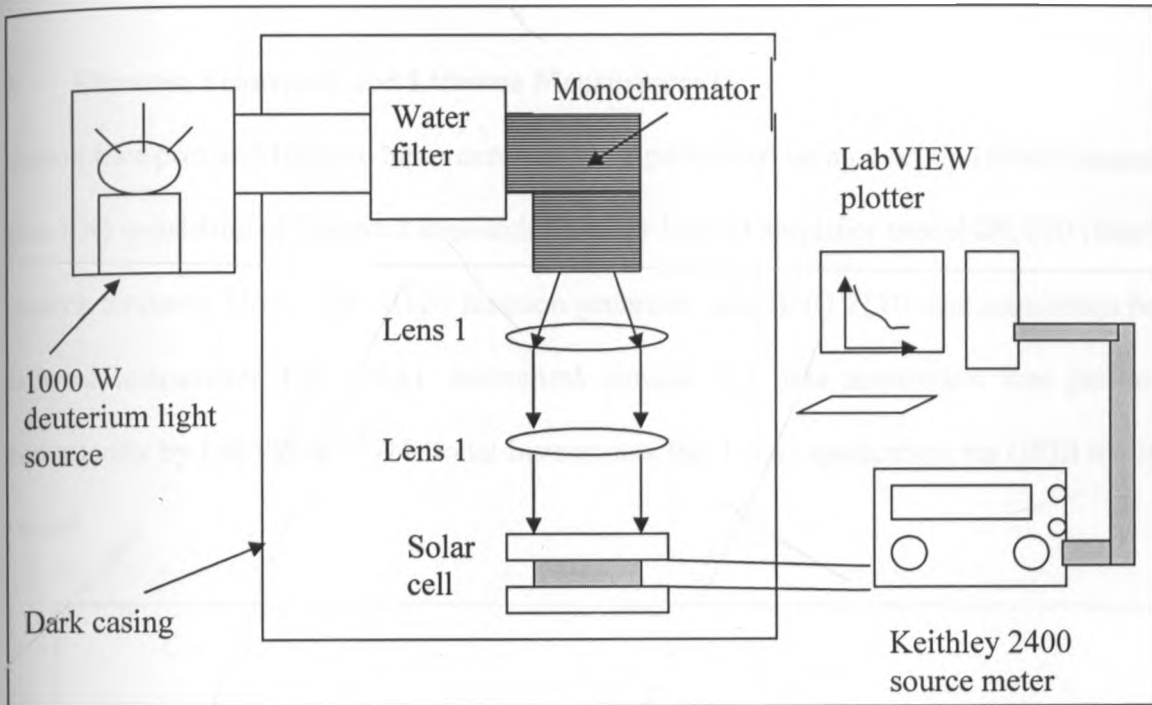


Figure 4.3: Schematic set up for *IPCE* characterization.

The monochromator, optical power meter and the source meter were connected to the computer and controlled automatically by LabVIEW program (see appendix II for details of the development). Before an *IPCE* was run, the monochromator power was calibrated using a photodiode in place of the solar cell. The photodiode was illuminated by a collimated light from the monochromator and the incident power measured by the optical power meter connected to the photodiode. This was recorded for wavelengths between 300 nm and 800 nm at steps of 20 nm. The recorded power was used as power of incident radiation (P_m) during the calculation of *IPCE*. The photodiode was then replaced with the solar cell and the terminals

connected to the Keithley 2400 source meter, which recorded the current generated at each wavelength. The monochromator was set to scan the wavelength from 300 nm to 800nm in steps of 20 nm. The measured current and incident power were used to calculate the *IPCE* at each wavelength and plotted on a graph.

4.5 Electron Transport and Lifetime Measurements

Electron transport and lifetime measurements were performed using a set up (block diagram in figure 4.4) consisting of Stanford Research Systems lock-in amplifier model SR 570 (Stanford Research Systems, USA), HP 33120 function generator, and BNC 2110 data acquisition board (National instruments Inc, USA). Instrument control and data acquisition was performed automatically by LabVIEW™ (National Instruments Inc, USA) application via GPIB interface protocol.

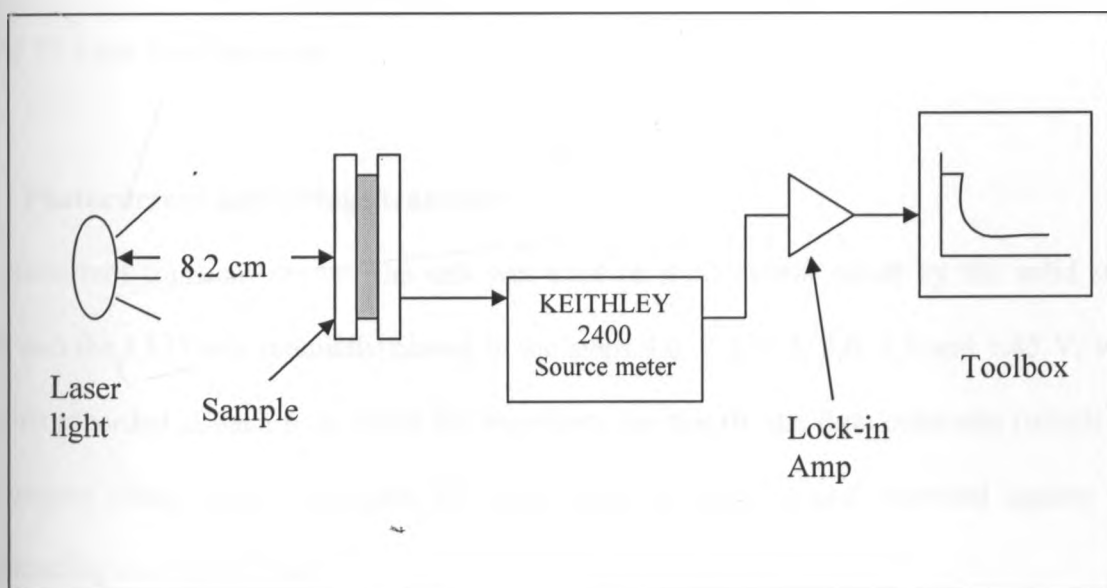


Figure 4.4: Block diagram of the transport and lifetime studies set up.

The light source was from a square pulsed laser diode (LabLaser, Coherent LabLaser, USA) with λ_{max} 635 nm biased with voltages 3.0, 2.5, 2.2, 2.0, 1.9 and 1.85 V giving light intensities of 15.5, 9.01, 5.07, 2.44, 1.15 and 0.51 mWcm^{-2} , respectively. Switching from potentiostatic (to measure in short circuit) and galvanostatic (in open circuit) was achieved by use of a solid state switch.

A small square wave modulation (<10% intensity, 0.1 – 2 Hz) was added to the base light intensity. The solar cell response (I or V transients) was fitted to exponential rise or decay function using a nonlinear least-squares fit. Traces were averaged 10 times for transport and 2 times for recombination studies. The set up described above was used to perform photocurrent transient spectroscopy (for electron transport studies), photovoltage transient spectroscopy (for electron lifetime studies) photovoltage decay studies, charge extraction experiments and electrochemical potential analysis for complete solar cells at 3.0 μm , 6.0 μm , 12.8 μm , 23.5 μm and 25.3 μm film thickness.

4.5.1 Photocurrent and voltage transient

In photocurrent transient set up, the cell was kept in short circuit mode by the solid state switch and the LED was manually biased in the steps 3.0, 2.5, 2.2, 2.0, 1.9 and 1.85 V, with transients recorded at each bias. From the transients and the fit, the time constants (which are the transport times) were calculated for each value of intensity and recorded against the corresponding current constant.

Photovoltage transient routine was similar to photocurrent's but the cell was set to open circuit for measurement of photovoltage decay. The time constants were calculated for each value of intensity and recorded against the corresponding photovoltage value. The illumination was done for substrate-electrode (SE), also known as backside, and electrolyte-electrode (EE) also known as front side illumination, modes and data recorded for each.

4.5.2 Photovoltage decay measurement

In this set up, the cell was illuminated under open circuit mode for some time then the laser was switched off. The voltage decay was monitored and recorded over time and used to calculate the electron lifetime from the relation earlier given in section 3.4.1, i.e.,

$$\tau_e = -\frac{k_B T}{e} \left(\frac{dV_{OC}}{dt} \right)^{-1} \quad (5.1)$$

for film thicknesses 3.0, 6.0, 12.8, 23.5 and 25.3 μm .

4.5.3 Charge extraction

In the charge extraction experiment, the solar cell was illuminated with a pulsed laser light in short circuit mode for 2 seconds then switched to dark. The current decay transient that followed was measured and integrated over a period of 10 s. The integration gave the quantity of charge that remained in the solar cell and was studied against the varying intensities and film thicknesses.

4.5.4 Electrochemical potential analysis

In this study, the solar cell was illuminated under short-circuit conditions for 2 seconds then the laser was switched off and the cell switched to open circuit, simultaneously. The voltage

change was then recorded over time. This was done at different laser biasing giving the incident illumination intensities 15.5, 9.01, 5.07, 2.44, 1.15 and 0.51 mWcm^{-2} for each film thickness. The maximum voltage ($V_{sc, max}$) and the time (t_{max}) at which it was attained were recorded.

Chapter Five

Results and Discussion

5.1 Introduction

In this chapter, structural (SEM, XRD and XPS) characteristics of TiO_2 photoelectrodes coated by screen printing method are discussed and analyzed. This is followed by analyzing the results from the dye pigment's absorption spectroscopy; *IPCE* and *IV* characteristics of the solar cell sensitized with anthocyanin dye compared with ruthenium complex dye. The chapter ends with the analysis of charge transport properties in these films of varying film thicknesses employing various routines like photovoltage decay, time resolved photocurrent spectroscopy and charge extraction among others.

5.2 Structural Characterization

SEM micrographs for films produced by screen printing method and doctor blade technique are presented in figure 5.1.

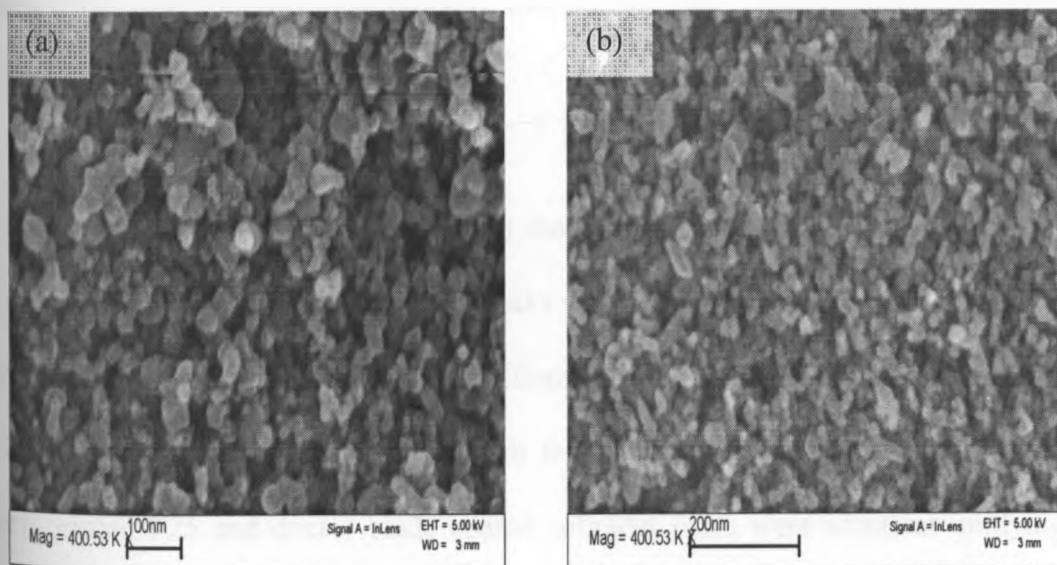


Figure 5.1: SEM micrograph for (a) screen printed TiO_2 film with P25 as the starting material (b) coated by doctor blade with titanium tetrachloride as the starting material.

The micrographs show that screen printing method produced films with nanometer sized particles, varying in sizes between 15 nm and 40 nm (Figure 5.1a). This is in agreement with the composition of P25 where 70 % is anatase (smaller particles) and 30 % is rutile (larger particles). Comparing with the micrograph of TiO₂ film made of colloids prepared from titanium isopropoxide synthesis coated by doctor blade technique (Figure 5.1b), the P25 film (Figure 5.1a) appeared more homogeneously dispersed. The particle sizes for TiO₂ colloids prepared from titanium isopropoxide (Figure 5.1b) appeared to be of smaller size (average particle size for these films was between 10 and 20nm) as compared to the screen printed films. The difference may be attributed to the synthesis method employed in preparation of the colloidal paste from titanium isopropoxide especially at the autoclave stage. The particle size has been studied elsewhere and found to depend on the autoclave temperature (Barbe, *et. al.*, 1997; Ito, *et. al.*, 2007) for the colloidal paste. The dependence of particle size to autoclave temperature was explained by Barbe's group to be due to sedimentation of TiO₂ particles during the hydrothermal synthesis. Autoclaving temperature helps in the growth of the primary particles by dissolution-re-precipitation mechanism that occurs under the hydrothermal conditions.

X-ray diffraction (XRD) scans (Figure 5.2) showed that the films produced were crystalline in nature (an observation of strong distinct peaks with different crystal orientations). Strong TiO₂ anatase peaks with crystal orientation directions (101) were observed for both films. The other peaks (200), (211), (112) and (105) are all for anatase phase. The scans for the films from screen-printed P25 and doctor blade coated colloidal paste were identical implying that the screen-printing method produced TiO₂ paste with similar characteristics as the colloidal one

except for the variation in particle sizes. The colloidal film had slightly broader peaks (as determined by Scherrer's formula, implying smaller particle size), corroborating the SEM results.

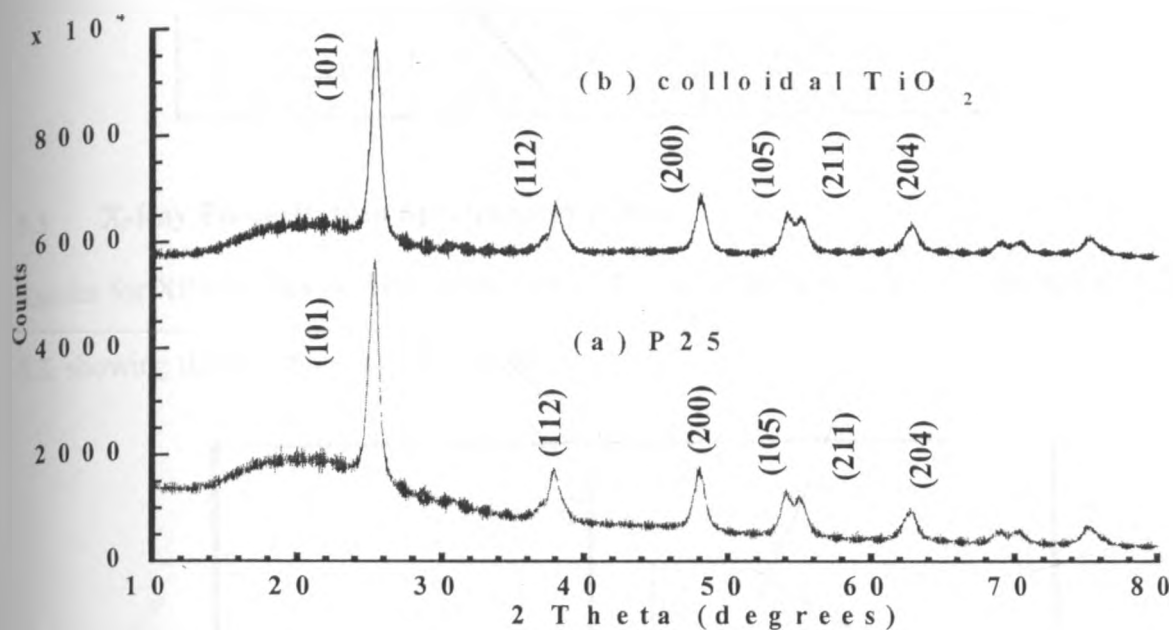


Figure 5.2: XRD surface scans for TiO_2 films made from (a) P25 by screen printing and (b) colloidal TiO_2 by doctor blade techniques.

Analysis of the peaks of XRD scans for the screen-printed film using Scherrer's formula showed that anatase particles had particle sizes ranging from 13 nm to 25 nm when calculated at a diffraction angle of 25 – 53 degrees (Table 5.1). This is close to the results obtained from SEM micrographs. The particle size could not be approximated for peaks at 53.98° and 55.17° because the peaks were not distinctive enough, i.e., the peaks were too broad hence could not give a good approximation.

Table 5.1: Table showing peak list and particle size for TiO₂ film made from P25

Peak Pos. (2Theta)	h k l	Type	FWHM (2Th.)	d-spacing (Å)	Particle size (nm)
25.2500	1 0 1	anatase	0.6047	3.52720	13.5
37.8742	1 1 2	anatase	0.3064	2.37555	27.4
47.9700	2 0 0	anatase	0.5791	1.89654	15.01
53.9800	1 0 5	anatase	0.0010	1.69872	-
55.1700	2 1 1	anatase	0.0010	1.66486	-
62.8600	2 0 4	anatase	0.3512	1.47843	25.38

5.3 X-Ray Photoelectron Spectroscopy (XPS)

Results for XPS studies on TiO₂ films with P25 as the starting material, are presented in figure 5.3, showing the complete XPS spectrum.

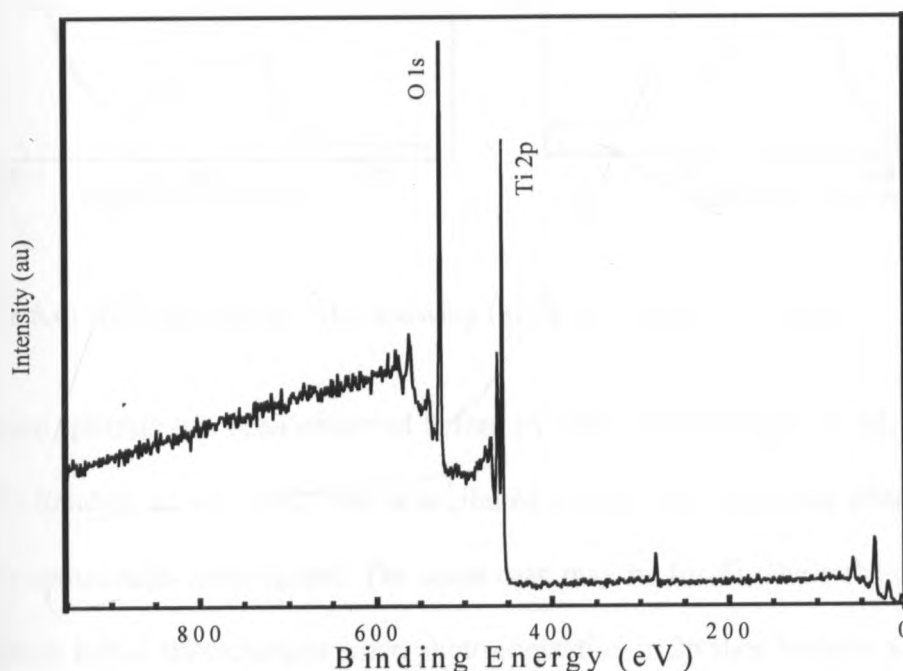


Figure 5.3: XPS spectra for screen printed TiO₂ film showing Ti 2p and O 1s peaks for titanium and oxygen species respectively.

In the spectrum, strong O 1s peak for oxygen and Ti 2p for titanium were observed at binding energies (BE) 530 eV for O 1s and 460 eV respectively. Closer inspection of the spectrum showed that Ti 2p level was split into closely spaced photoemission doublet. This was seen

clearly when the spectrum in the region of Ti 2p was expanded giving rise to two distinct peaks at 461.5 eV and 467.0 eV of binding energy (BE) (Figure 5.4a). Similar expansion for O 1s showed only one distinct peak at 529.9 eV as shown in figure 5.4b. The two peaks for Ti 2p photoemission had intensity ratio of 1:3 for 467 eV and 461.5 eV, respectively.

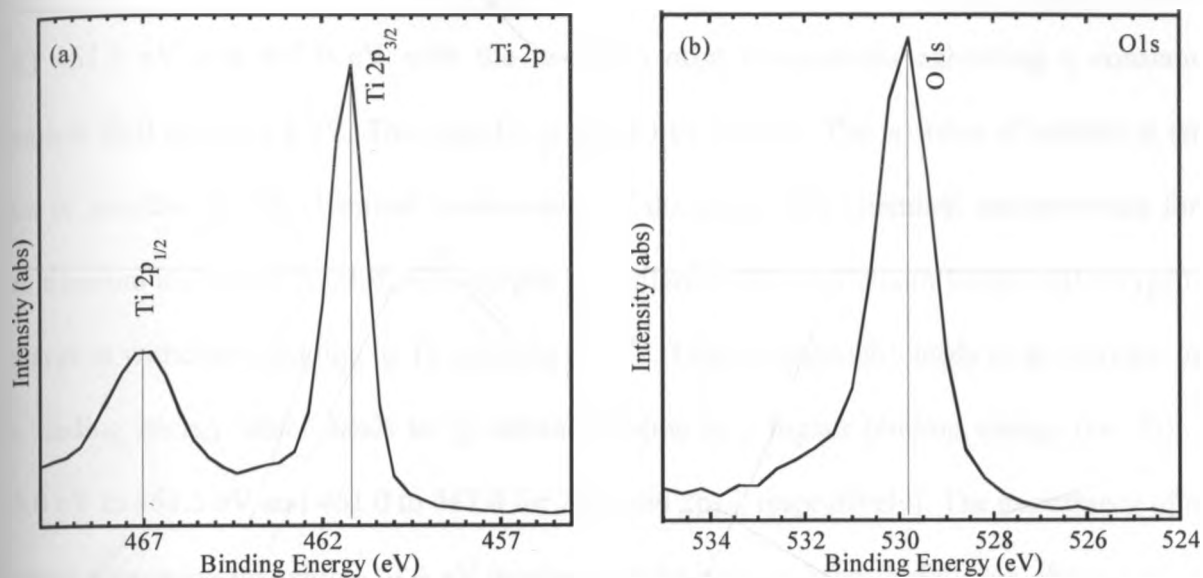


Figure 5.4: XPS spectra for TiO₂ showing (a) Ti 2p and (b) O 1s peaks.

Photoemission splitting has been observed before by other groups (Ingo, *et. al.*, 1993; Reddy, *et. al.*, 2001; Sandell, *et. al.*, 2002) and is attributed to spin-orbit coupling effects in the final states of the compounds investigated. The same case may be for Ti where the core electronic configuration in initial state changes when photo-ionization in 2p state leads to a removal of an electron changing the configuration in the final state. From the intensity ratio of 1:3 the degeneracies of the final states were deduced to be $\frac{1}{2}$ and $\frac{3}{2}$ giving rise to states Ti 2p_{1/2} and Ti 2p_{3/2}, respectively. The spin-orbit splitting was not observed at s-level for oxygen. The appearance of only one distinct peak for O 1s peak at 529.9 eV (Figure 5.4b) implied that Ti was completely oxidized in this film with only one oxygen species. Another case that was

noted was the peak shift in Ti 2p states for titanium (Figure 5.4a). Previous studies by other groups (Ingo, *et. al.*, 1993; Reddy, *et. al.*, 2001; Sandell, *et. al.*, 2002; Sandell *et al.*, 2003) on titanium have shown that it exhibits large chemical shifts between different oxidation states of the metal. Standard XPS studies on pure titanium has shown the 2p_{1/2} and 2p_{3/2} states to be at 455.0 eV and 461.0 eV. In the present study, the two states were observed at binding energy (BE) 461.5 eV and 467.0 eV with the two spin orbit components exhibiting a constant chemical shift of about 6 eV. This may be explained as follows: The position of orbitals in an atom is sensitive to the chemical environment of the atom. The chemical environments for pure titanium and when bonded with oxygen are different. When titanium bonds with oxygen, a charge is withdrawn leading to Ti reducing to Ti⁴⁺. This consequently leads to an increase in the binding energy which leads to 2p orbital relaxing to a higher binding energy (i.e. from 455.0 eV to 461.5 eV and 461.0 to 467.0 for 2p_{1/2} and 2p_{3/2}, respectively). The appearance of a constant relaxation magnitude of 6 eV implies that the process is an initial state effect, a case that is observed in core levels of solids.

5.4 Dye Characterization

Figure 5.5 shows the titration curve for anthocyanin pigment for determining the dissociation point of the dye molecule. Between pH 2.10 and pH 3.50, the dye solution retained its violet color but as the pH increased towards pH 4.00, the dye pigment turned colorless. The colorless appearance lasted in the range between pH 4.06 and pH 4.70 then it gradually turned green as pH reached 5.70. The solution retained the green color from pH 5.70 to 9.80 then gradually turned yellowish orange. From the plot of the titration curve (Figure 5.5), violet dye had a point of inflexion at pH 4.50 (the same pH value the solution turned from colorless to green).

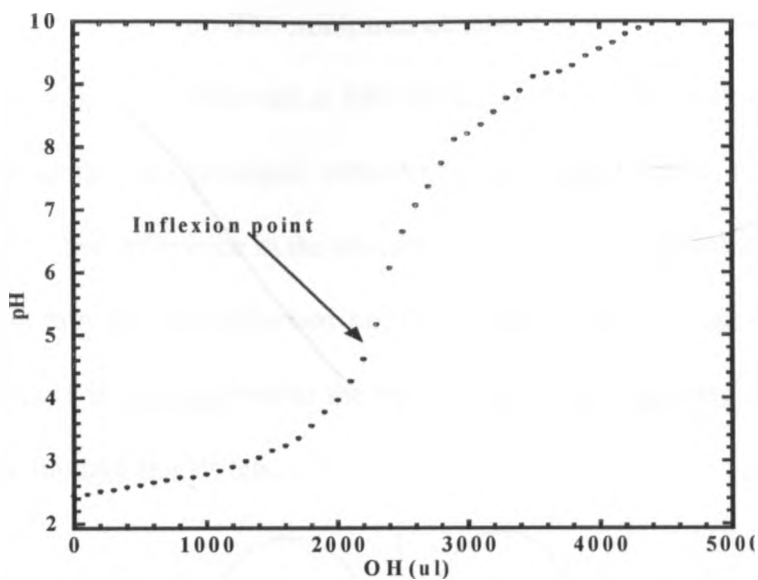


Figure 5.5: Titration curve for violet dye using 0.01M NaOH.

Results for absorption characteristics are given in figure 5.6 showing the absorption characteristics for the dye pigment before and after adsorption on the TiO_2 photoelectrode.

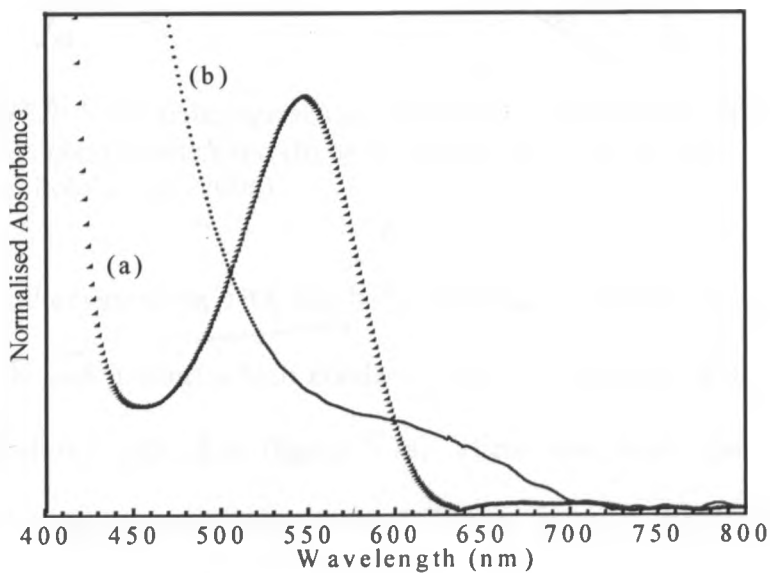


Figure 5.6: Absorption spectra for anthocyanin dye pigment (a) before and (b) after being adsorbed on TiO_2 photoelectrode.

From the figure, before sensitization, an absorption maximum was observed at 550nm (curve a) but upon sensitization, there was reduction in absorption intensity which broadened towards

the longer wavelength (curve b). The minimum observed at 450 nm represents the solution's baseline while the maximum observed at 550 nm for plot (a) is consistent with that reported for delphinidin molecule, the principal anthocyanin compound found in *hibiscus sabdariffa* (Polo, *et. al.*, 2006). The difference in the absorption intensity and broadening between the dye extract in solution and the one adsorbed on TiO_2 could be due to the effect of binding of anthocyanin molecule in the pigment to the oxide surface (as suggested in figure 5.7) and to the kind of charge transfer transitions.

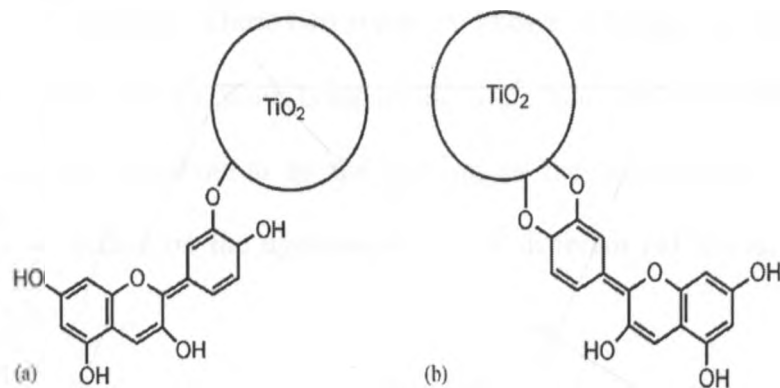


Figure 5.7: Schematic representation of anthocyanin attachment (a) by alcoholic condensation and (b) by chelating effect on the TiO_2 surface (Polo, *et. al.*, 2006).

Chemisorption of anthocyanins on TiO_2 has been reported by Hao, *et. al.*, (2006) to be as a result of alcoholic bound protons which condense with the hydroxyl groups present at the surface of nanostructured TiO_2 film (figure 5.7a). There also exists the binding of these molecules on TiO_2 by the chelating effect to the Ti^{4+} ions, (figure 5.7b) (Garcia, *et. al.*, 2003; Tennakone, *et. al.*, 1997). This attachment to the TiO_2 surface stabilizes the excited state, thus shifting the absorption maximum towards the lower energy of the spectrum. Wongcharee, *et. al.*, (2007) studied the absorption characteristics on blue pea extract and did not observe any shift in the absorption maximum. The absence of the shift could imply that there was no

effective adsorption which was attributed to the kind of structure in blue pea. In their study, Wongcharee, *et. al.*, (2007) observed that the blue pea had strong presence of ternatuin molecule that is known to have long OH groups. These long OH groups may prevent anthocyanin from forming a bond with the oxide surface and also from arraying to the TiO₂ film effectively. In the present study therefore, the shift implies that there is no such hindrance to the bonding of the OH group with the oxide surface. The shift is also attributed to the changing of the anthocyanin molecule from the more stable flavilium state to the unstable quinoidal state upon chelation. These two states are known (Cherapy, *et. al.*, 1997) to exist at two different pH levels with flavilium being acidic while quinoidal form being basic. In order to effectively link this observation to the shifting in the anthocyanin states, absorbance characteristics were studied on the dyes in solution at different pH levels, whose results are shown in figure 5.8.

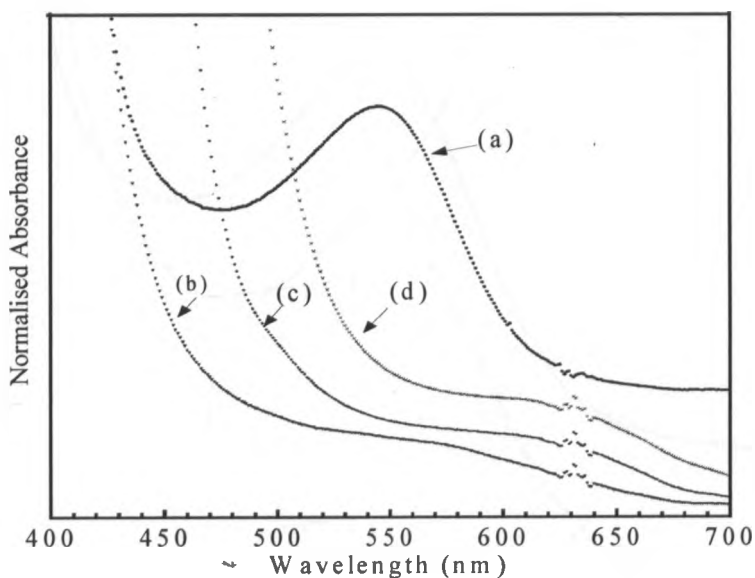


Figure 5.8: Absorption spectra for anthocyanin dye in solution at (a) pH 2.00 (b) pH 5.17 (c) pH .07 and (d) pH 8.34.

It is observed that the peak that appeared at pH 2.00 disappeared as the pH increased beyond pH 2.00, being replaced with low absorption intensity and broadening (figures (b), (c) and (d)). The appearance of a kink at 630 nm on all plots is the effect of detector change over. The broadening towards the longer wavelength is quite similar to the spectrum for dye-sensitized photoelectrode (plot b in figure 5.6). Comparing observations in figures 5.6 and 5.8, it may also be confirmed that upon sensitization, the anthocyanin molecule shifts from the flavilium to quinoid state which are acidic and basic, respectively. The quinoid states are quite unstable, a feature that exhibits very weak absorption maxima when the dye is attached on TiO_2 . An attempt to lower the pH of the dye sensitized film (by fuming HCl over it) showed the re-appearance of the absorption maximum, almost matching the one for the un-sensitized dye molecule (Figure 5.9).

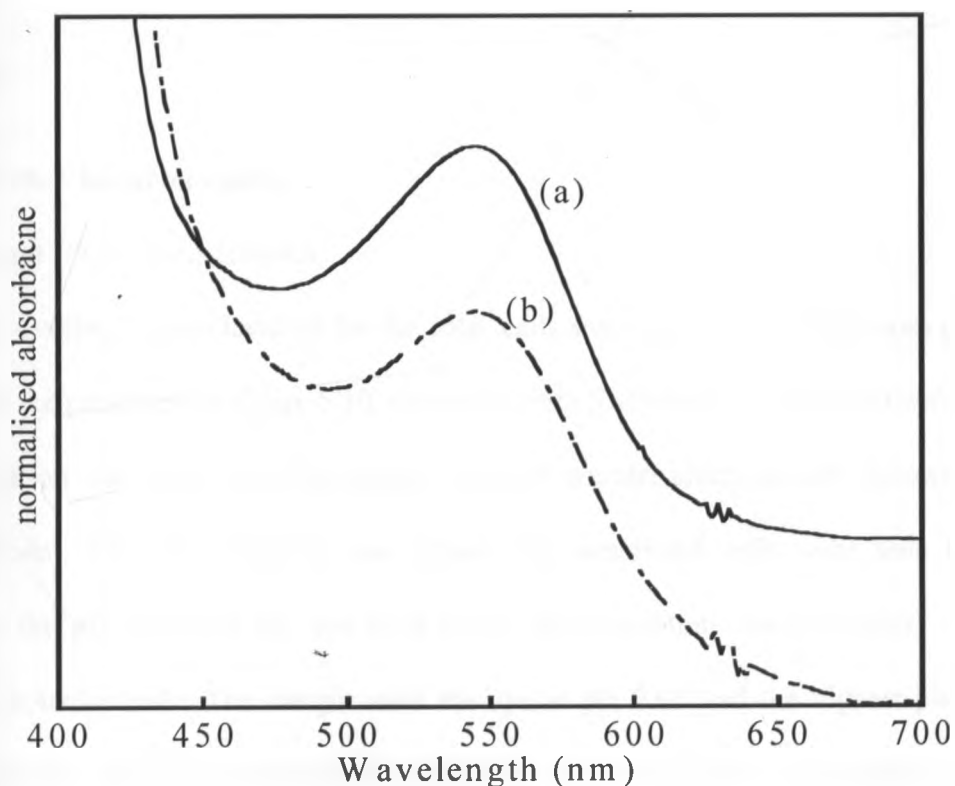


Figure 5.9: Absorption spectra for anthocyanin dye pigment (a) before and (b) after sensitization with TiO_2 photoelectrode and fumed with HCl.

It is further noted that the absorption maximum increases and shifts slightly to the red (plot (b)) which shows that there is the evidence of chelation between the dye molecule and the Ti^{4+} . As earlier mentioned, band shifts could be attributed to the molecular transitions that take place when the dye molecule chelates with TiO_2 . Anthocyanin pigments exhibit $\pi - \pi^*$ orbital transition which is attributed to the 552 nm peak (curve b, figure 5.9). Wang, *et. al.*, (2007) in their study of sensitization using coumarin dye observed that the introduction of one more carbon-nitrogen (CN) ligand group into the molecular frame of coumarin decreased the gap between the highest occupied molecular orbital (HOMO) and lowest unoccupied molecular orbital (LUMO), thus extending the maximum absorption from 511 to 552 nm. In the present study, the shift upon sensitization may be similarly attributed to the $\pi - \pi^*$ orbital transition within the dye molecule upon sensitization, also the lowering of the gap between HOMO and LUMO.

5.5 Solar Cells Characterization

(a) *I-V* and *IPCE* characteristics

The current - voltage characteristics for the solar cells sensitized with anthocyanin pigment at different pH are presented in figure 5.10, compared with Ruthenium N719 sensitized solar cell. The illumination was incident on the sample from the counter electrode side (known as SE or backside mode). The characteristics for anthocyanin sensitized cells were seen to depend strongly on the pH levels of the dye (and hence the absorption characteristics) of the dye sensitized photoelectrode. The sample with the dye at pH 2.00 had the highest photocurrent density (and also highest overall efficiency) while the one at pH 1.8 recorded the lowest efficiency (see summary in Table 5.2).

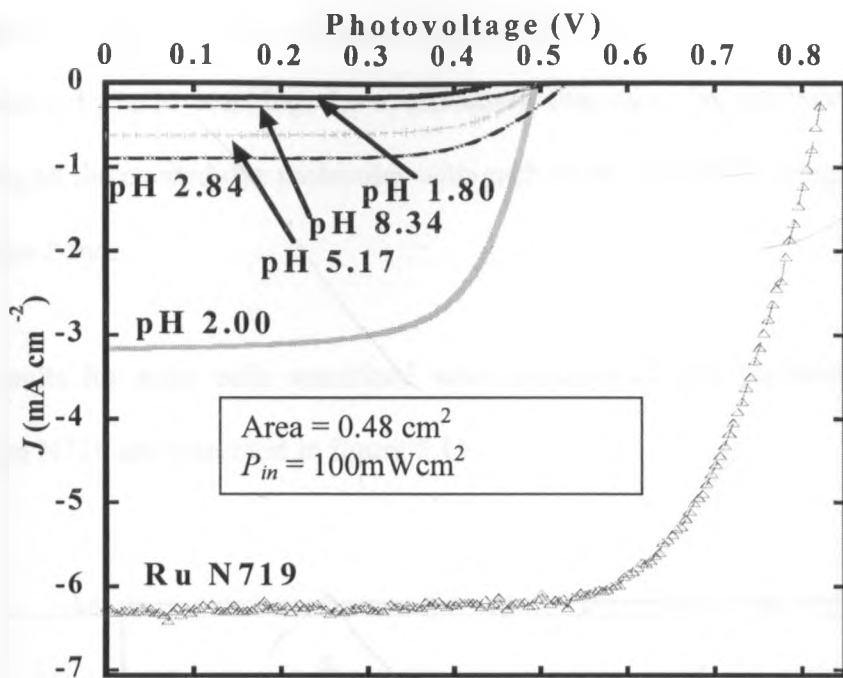


Figure 5.10: I - V curves for anthocyanin sensitized solar cells at different pH levels compared with Ru N719 sensitized solar cell.

Table 5.2: Summary of IV characteristics for anthocyanin sensitized solar cells at different pH levels

pH	V_{oc} (V)	J_{sc} (mAcm ⁻²)	FF	η (%)
1.80	0.44	0.17	0.66	0.05
2.00	0.49	3.17	0.66	1.04
5.17	0.50	0.63	0.65	0.20
8.34	0.51	0.3	0.57	0.08

The low efficiency observed for anthocyanin sensitized cells at pH 5.17 and above may be attributed to the fact that an increase in pH hydrated the anthocyanin molecule to quinoid state which is unstable compared to the lower pH flavilium state. In this scheme, the increase in pH (more OH groups introduced in the dye) leads to the prevention of anthocyanin molecule from forming bonds with the oxide surface and also from arraying to the TiO₂ film effectively. This in turn affects the efficient charge transfer from the excited state of the dye molecule to the conduction band of TiO₂. On the other hand it is observed that efficiency dropped

tremendously when pH was lowered from 2.00 to 1.81, the drop could be due to cell deterioration by acid leaching. Low efficiency may also be attributed to energy loss via quenching of the excited dye molecules with each other, instead of being injected into the TiO_2 conduction band.

IPCE results for solar cells sensitized with anthocyanin dye pigment at different pH and ruthenium N719 are presented in figure 5.11.

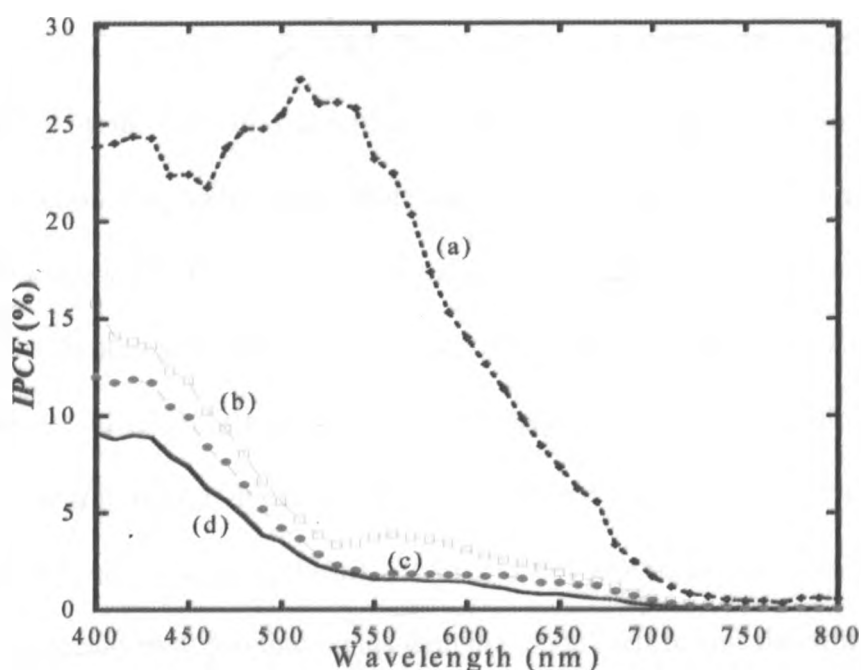


Figure 5.11: *IPCE* for solar cells sensitized with (a) ruthenium N719 and anthocyanin pigment at (b) pH 2.00 (c) pH 8.34 and (d) pH 5.17.

Solar cells sensitized with anthocyanin pigment recorded low *IPCE* in the visible spectrum compared to the one sensitized with ruthenium N719. The $IPCE_{max}$ of about 4% was observed at 560 nm for the anthocyanin sensitized cell at pH 2.00 (curve (b), figure 5.11), which lowered as the spectrum extended towards the infrared. This was the highest $IPCE_{max}$ observed in all the anthocyanin sensitized solar cells characterized. Further observation was that

$IPCE_{max}$ reduced and red-shifted as the pH increased from acidic to basic (curves c and d, figure 5.11). This observation is consistent with absorbance characteristics (figure 5.8) whose maximum also shifted from shorter wavelengths towards the red as the pH changed from acidic to basic. Since $IPCE$ consists of injection, transport and collection efficiencies, the low $IPCE$ reported here could have the contributions from all the three processes but the injection efficiency could have the most effect. Low injection efficiencies could be due to improper matching of the dye's HOMO level (optimal levels are -3.5 to -3.8 eV on vacuum scale) (De Angelis, *et. al.*, 2008) with the semiconductor's conduction band (typical levels -4.0 - -4.5 eV on vacuum scale for TiO_2) (Grätzel, 2003; De Angelis, *et. al.*, 2008). The kind of adsorption of the dye molecule on the TiO_2 may contribute to the low $IPCE$ values recorded here. As earlier discussed in section 5.4, anthocyanin molecules chelate with Ti^{4+} centres and consequently shift from the more stable flavilium state to the unstable quinoidal state upon chelation. These two states exist in acid and basic forms, respectively. The optimal pH of 2.00 shows that at that pH, there are sufficient OH groups that offer adequate chelation in acidic medium leading to an improvement in charge injection efficiency from the dye molecule to the TiO_2 . Whereas at higher pH (in basic or quinoid form), the excess OH groups present lead to prevention of anthocyanin molecule from forming bonds with the oxide surface and also from arraying to the TiO_2 film effectively hence lowering the charge injection efficiency.

The characteristics for anthocyanin sensitized film at pH 2.00 that exhibited the best performance are compared with ruthenium N719 sensitized cell in table 5.3 in summary form. From the summary, it can be seen that values for the fill factor for both cells are very close,

implying that electrical losses due to series and shunt resistances were very minimal in both cells.

Table 5.3: A comparison of *IV* and *IPCE* characteristics between anthocyanin sensitized solar cell at pH 2.00 and ruthenium N719 sensitized solar cell

Parameters	Anthocyanin sensitized	Ruthenium N719 Sensitized
V_{oc} (V)	0.49	0.83
J_{sc} (mA/cm ²)	3.17	6.16
<i>FF</i> (%)	66	65
η (%)	1.04	3.29
$IPCE_{max, \lambda}$ (nm)	560	540
$IPCE_{max}$ (%)	4	25.5

Other parameters like V_{oc} , J_{sc} and overall efficiency for anthocyanin sensitized solar cell were in general half the parameters for ruthenium N719 sensitized solar cell. However, there was a large difference in the $IPCE_{max}$ with anthocyanin sensitized solar cell recording a maximum of 4% compared to above 26% for ruthenium N719. The difference in $IPCE$ maximum could be attributed to the kind of charge transfer transitions that take place between the dye molecule and the semiconductor where ruthenium sensitizer performs the metal to ligand charge transfer (MLCT) while anthocyanin performs the ligand to ligand transfer. MLCT transfers are more efficient than the ligand-ligand transfers and their time constants have been measured and found to be in orders of picosecond (Grätzel, 2005).

(b) Photoelectrochemical characterization

The results of cyclic voltametry on anthocyanin dye pigment are shown in figure 5.12. The scans show a deviation from a pure Nernstian profile for a reversible system. Scan (a) was

recorded after stirring the solution and letting it return to equilibrium. This was because a test run taken showed that the solution had very slow diffusion hence the need to stir.

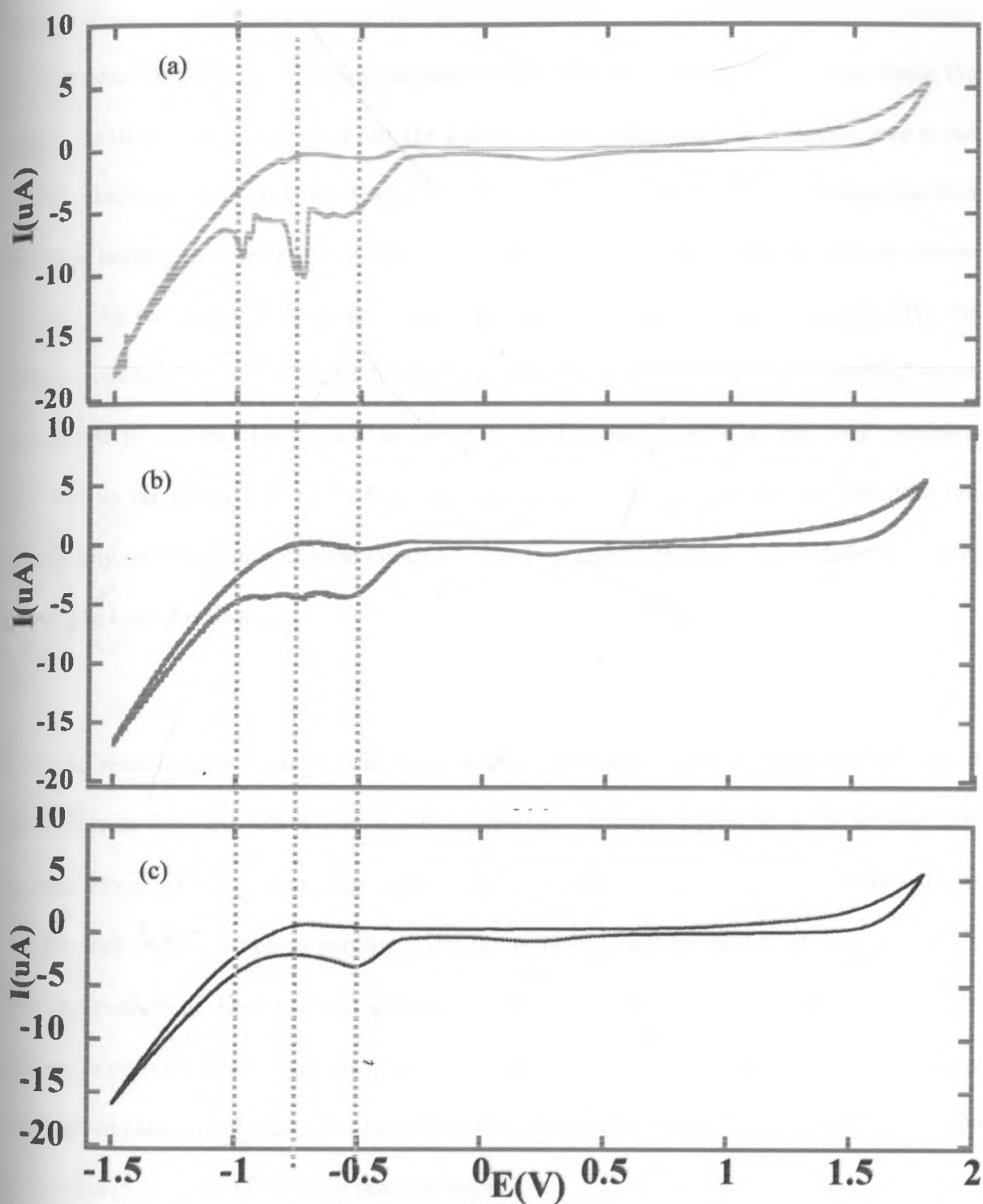


Figure 5.12: Cyclic voltammograms on anthocyanin dye pigment in different environments where (a) the solution is stirred, (b) N_2 purged and (c) Ar bubbled.

As the potential sweep increased from 0 V at the working electrode, the counter electrode showed a slow current response which increased exponentially to a maximum as the potential sweep reached +1.6V. On reversing the sweep towards 0 V, the current response decreased again exponentially but not retracing the path for potential rise. During this process when the applied positive potential sweep is run, the concentration of the iodide species decrease at the working electrode surface which leads to a higher concentration gradient between the two electrodes leading to a more flux to the surface which leads to the exponential rise in current observed. As the potential is reversed from the switching point (+1.6 V) towards 0V, the surface concentration begins to rise hence decreasing current. The behaviour described above is observed in all the three scans in figure 5.12. The half oxidation and half reduction discussed so far (from 0 V to +1.6 V and back to 0 V) shows that the reaction does not undergo any oxidation or reduction (since no peak is observed between 0 V and the switching potential in both directions).

When the reverse scan is swept past 0 V towards -1.5 V an observation of a sudden rise of anodic current between -0.5 V and -1.0 V suggesting a reduction process of the anthocyanin pigment. However, on purging, the peak disappeared (scans (b) and (c)). This may indicate that the peak observed before purging is for impurities present in the analyte and not due to oxidation process of the dye. Purging process removed any impurities that were present in the analyte (oxygen included). The absence of the peak implies that dye pigment does not undergo reduction-oxidation and hence it depends on the electrolyte's redox species for regeneration via process (5.2c) in the following reaction steps:



That is, the dye molecule is reduced to ground state by accepting an electron from $3I^-$ which itself gets oxidized to I_3^- (reactions 5.2c and d).

5.6. Effect of Film Thickness on Electron Transport

The results in this section are for TiO_2 films sensitized with ruthenium N719 dye complex and studied at film thickness 3.0 μm , 6.0 μm , 12.8 μm , 23.5 μm and 25.3 μm .

5.6.1 I - V characteristics versus film thickness

Figure 5.13 shows I - V characteristics of the solar cells at varying film thicknesses. It is observed that open circuit photovoltage decreases with increase in film thickness. The film with lowest thickness (3.0 μm) gave the highest V_{oc} of 0.855 V while the thickest (25.3 μm) had 0.751 V (Table 5.4). The corresponding short circuit current densities for these films were 3.24 mA/cm^2 and 7.57 mA/cm^2 yielding FF of 0.699 and 0.643, respectively.

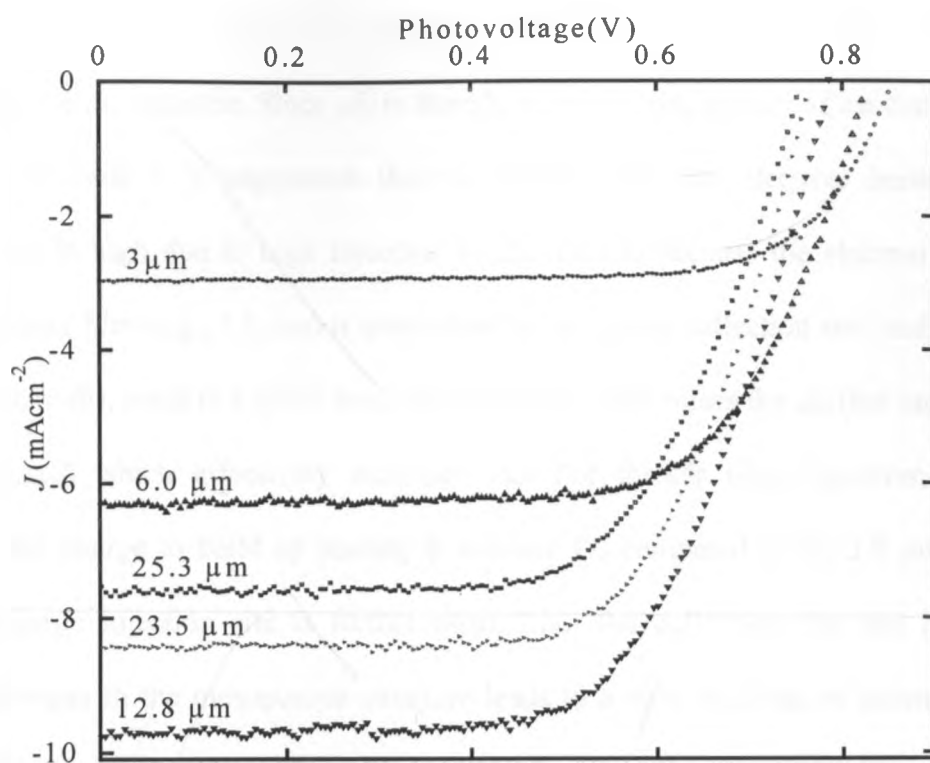


Figure 5.13: I - V characteristics of sealed solar cells from screen printed TiO_2 films of varying thicknesses.

Table 5.4: I - V characteristics for solar cells sensitized with ruthenium N719 at varying film thickness

Sample Thickness (μm)	V_{oc} (V)	J_{sc} (mA/cm^2)	FF	Efficiency (%)
3.0 ± 0.2	0.835	3.24	0.699	1.89
6.0 ± 0.2	0.825	6.16	0.649	3.29
12.8 ± 0.2	0.778	9.75	0.625	4.74
23.5 ± 0.2	0.759	8.39	0.653	4.16
25.3 ± 0.2	0.751	7.57	0.643	3.66

As earlier discussed in section 3.2.1, the V_{oc} of an electrochemical cell is determined by the difference between the Fermi level of the semiconductor and the redox potential ($E_{f,redox}$) of the redox electrolyte. Therefore the high V_{oc} observed for $3.0 \mu\text{m}$ thick film may imply that the difference in the Fermi level is large for this film as compared to the $25.3 \mu\text{m}$. Since the electrolyte used in this study was same all through (implying that the redox potential was same

in all the cells), it leads to a suggestion that film thickness has an effect on the quasi Fermi level (nE_f) of the semiconductor. Since nE_f is directly related to the density of conduction band electrons (n_c), it leads to a suggestion that in thinner films, the electron density in the conduction band is high due to high injection levels. This is because the electron injection point in the thinner film (e.g., 3.0 μm) is quite close to the charge collection site (and since the cell is in open circuit), leads to a quick build-up of charges. This raises the nE_f (but maintaining a constant $E_{f,redox}$) which effectively increases V_{oc} . For thicker films however, it takes sometime for the charge to build up leading to a lower V_{oc} compared to the 3.0 μm . This is because the charge injection site is further away from the collection site and hence the diffusion of charges in the mesoporous structure leads to a slow build-up of potential. This effectively leads to a lower value of V_{oc} measured in the cell.

Short circuit photocurrent density exhibited a different relationship with the film thickness (figure 5.14). It was observed that short circuit photocurrent density increased with film thickness to an optimal value of thickness of 12.8 μm then it reduced again as with increase in film thickness. The variation of photocurrent density with film thickness may imply that electron recombination with the redox electrolyte plays a role in cells at short circuit mode, as herein discussed in the next paragraph.

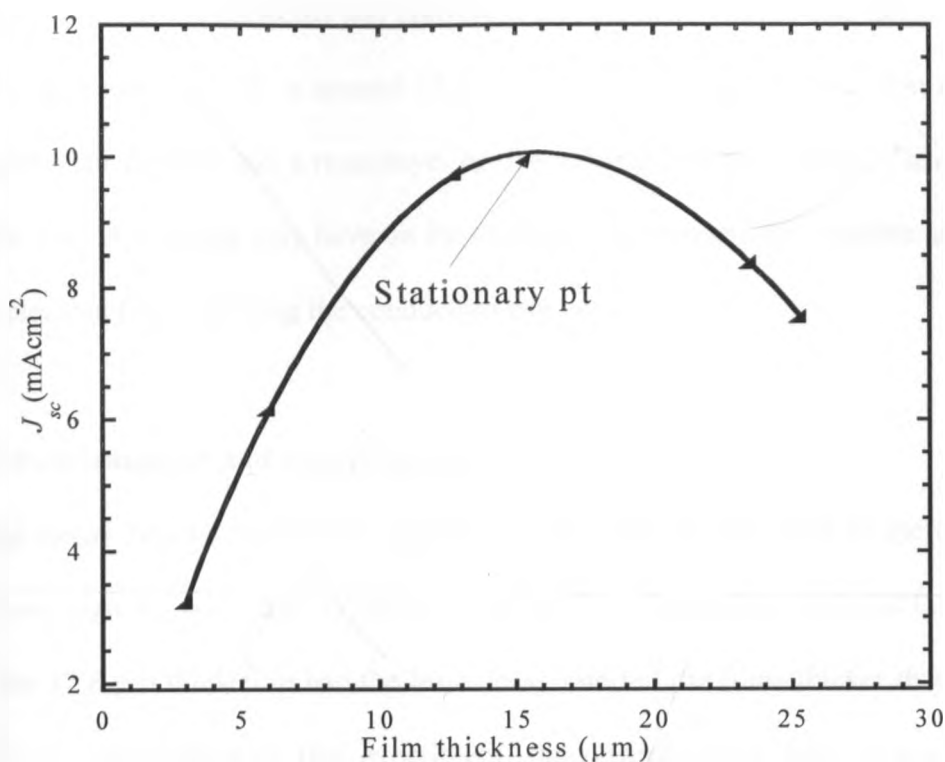


Figure 5.14: Relationship between film thickness (d) and short circuit photocurrent density (J_{sc}).

The observation depicted in fig 5.14 may imply that in the 3.0 μm thick film, both electron recombination via redox electrolyte and collection at the TCO are high in the film leading to very low J_{sc} . However, as the film thickness increases and more electrons are generated, more are collected and less recombine. A balance between recombination and collection is attained at film thickness of around 12 – 15 μm (stationary point on the plot in figure 5.14) then beyond that there is a decrease in J_{sc} with further increase in film thickness. This may mean that at film thicknesses beyond 12.8 μm , the cell experiences more recombination via the redox electrolyte as compared to charge collection at the TiO_2/TCO interface. This leads to less charge collection at the interface leading to low J_{sc} . A case worth noting is that the overall efficiency varies just as the variation of J_{sc} , due to the fact that J_{sc} has a direct connection to the overall efficiency in a DSC. That is, the overall efficiency of a solar cell is to a large extent dependent

on the amount of electrons collected and converted into electricity. This also suggests that the optimal film thickness for DSC is around 12.0 to 15.0 μm . The above discussion is based on the assumption that the film has a monolayer of dye adsorbed on the surface. This eliminates the influence thick dye layers may have on the electron injection and the possible screening of the excited electron from reaching the conduction band of TiO_2 .

5.6.2 Electron transport and recombination studies

Photovoltage decay results depicted in figure 5.15 show that at the onset of the decay, very thin films have high V_{oc} compared to thicker ones but the voltage decay is quite fast. It is also noted that the 12.8 μm thick film had the least decay rate but the films thicker than that again had high decay rates. Since in this experiment, the recombination path is assumed to be through the conduction band electrons recombining with redox species (that is, when the cell is in open circuit mode), it implies that from above results, thinner films have high recombination rates than thicker ones. In very thin films, the high V_{oc} , combined with high decay rate may be explained with the aid of figure 5.16, which shows the V_{oc} decays for the first 0.2 s (5.16a) and in the longer time scale (between 1 and 3 s) of the decay (5.16b). For the thinnest film and at the onset of illumination (Figure 5.16a), there is a high concentration of charges in the film, which leads to a high V_{oc} being measured. However, when the cell is in the dark and since the same charges are very close to the redox electrolyte, they readily recombine leading to the cell having lowest V_{oc} at the longer time scales (figure 5.16b). In both cases (under illumination and in dark), the path traveled by the charges is very short hence the high values of V_{oc} at the onset and high decay rate at longer timescales are observed.

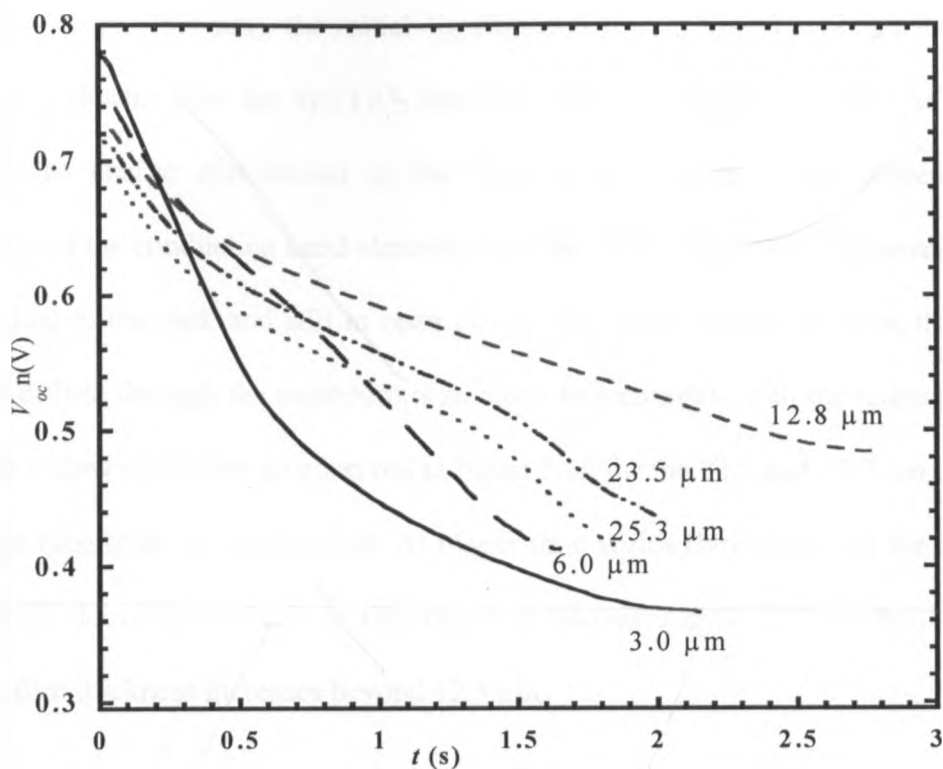


Figure 5.15: V_{oc} decay profile of TiO_2 solar cells of varying film thicknesses at 15.6 mWcm^{-2} illumination intensity.

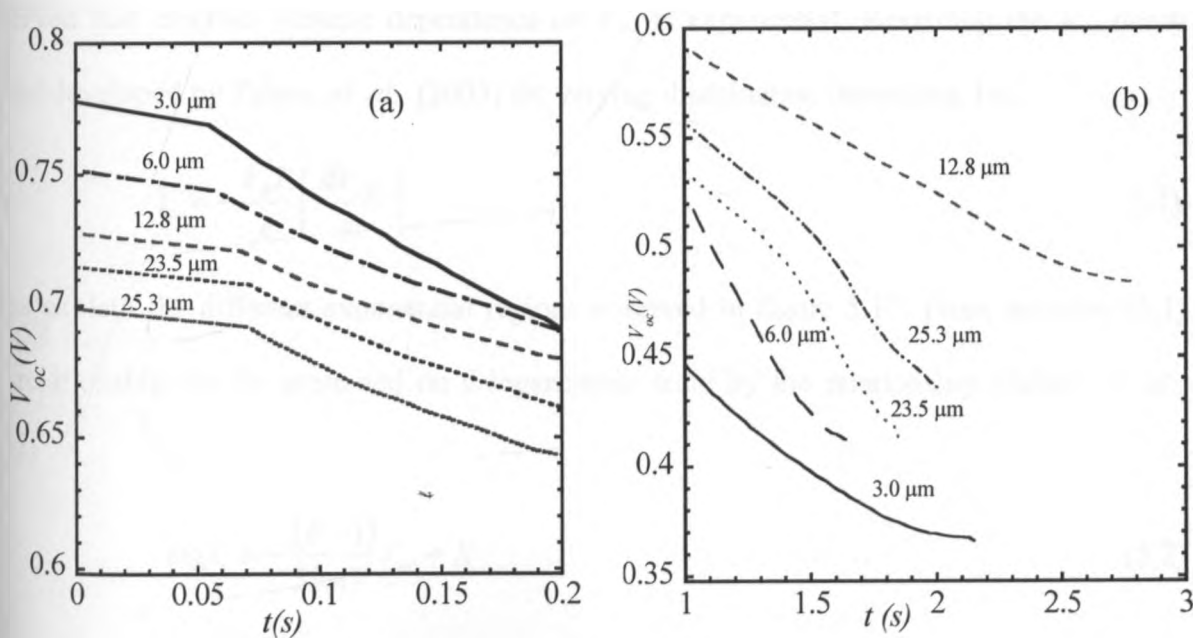


Figure 5.16: V_{oc} decay profiles for TiO_2 solar cells at varying film thickness showing (a) decay curves at the shorter time scale and (b) at the longer time scale.

For thick films (e.g., 25.3 μm), the initial V_{oc} (figure 5.16a) is low. This is attributed to the slow electron diffusion from the dye/TiO₂ interface to evenly distribute within the TiO₂ film. The process of charge distribution in the film is to a lesser extent affected by the recombination of the conduction band electrons with the redox electrolyte. However, when the cell is switched to the dark and still in open circuit, the decay is slow as again the electrons take time to diffuse through the mesoporous structure to recombine with the redox electrolyte. This leads to a slow decay rate as observed in figure 5.15 for the 23.5 and 25.3 μm thick films, and at longer time scale in figure 5.16b. At longer time scales (beyond 1 s of the decay), the trend is that the decay rate reduces as film thickness increases until 12.8 μm then it increases again as the film thickness increases beyond 12.8 μm .

A plot of electron lifetime (t_e) against the V_{oc} (figure 5.17) reveals that the photovoltage decay in dye sensitized solar cells is exponential with different rates. From the figure it can be observed that electron lifetime dependence on V_{oc} is exponential. Revisiting the V_{oc} decay model developed by Zaban, *et. al.*, (2003) for varying illumination intensities, i.e.,

$$t_e = -\frac{k_B T}{e} \left(\frac{dV_{oc}}{dt} \right)^{-1} \quad (5.1)$$

helps explain the different exponential regions observed in figure 5.17. From equation (5.1) the relationship can be presented on a logarithmic scale by the relationship (Zaban, *et. al.*, 2003)

$$\log t_e = -\frac{(\beta - 1)}{59\text{mV}} V_{oc} + K \quad (5.2)$$

Where $\frac{k_B T}{e} = 59\text{mV}$, K is a constant and β is a constant that gives the exponential term.

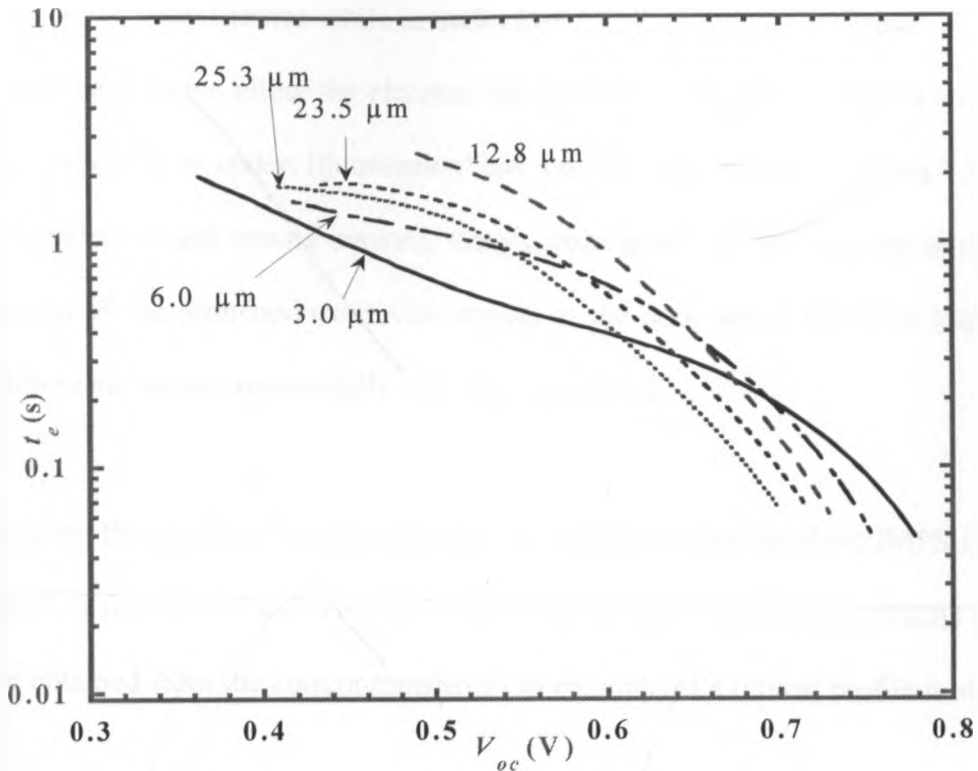


Figure 5.17: Calculated electron lifetime from V_{oc} decay curves in figure 5.15 for varying film thickness.

Equation 5.2 shows that for $\beta \neq 1$ the lifetime takes a bi-exponential relationship with V_{oc} which agrees with the experimental results in figure 5.17. The plots in figure 5.17 each have two regions presented by different values of gradient. Zaban's group used this model in equation 5.1 to study V_{oc} decay at varying illumination intensities (Zaban, *et. al.*, 2003) and observed that V_{oc} decay increased with initial illumination intensity. It was concluded that recombination in DSCs has contributions from trapping, detrapping and charge transfer mechanisms. In the present study the observation at constant illumination intensity also shows a bi-exponential profile, implying that recombination process across all thicknesses has contributions from trapping-detrapping as well as charge transfer mechanisms. In general, the electrons have shorter lifetimes at higher V_{oc} and longer lifetimes at lower V_{oc} . This is possible because at higher V_{oc} , the electron concentration is high and hence the mean free paths are

quite short hence the short lifetime while in under low V_{oc} , the lifetimes are longer because. It can also be attributed to the effect the electron injection from the dye and the recombination via the redox electrolyte under illumination has on the free electron density. When at equilibrium (generation and recombination), the V_{oc} corresponds to the increase in the quasi Fermi level (nE_f) of the semiconductor with respect to the dark which therefore implies the electron lifetime also varies exponentially with the Fermi level.

Figure 5.18 shows the results of charge transport as studied by time resolved IMPS in which the exponential fit for short circuit current is plotted as a function of transport time (5.18a). The fits were obtained from the current transients (an example of a typical profile is shown in the inset).

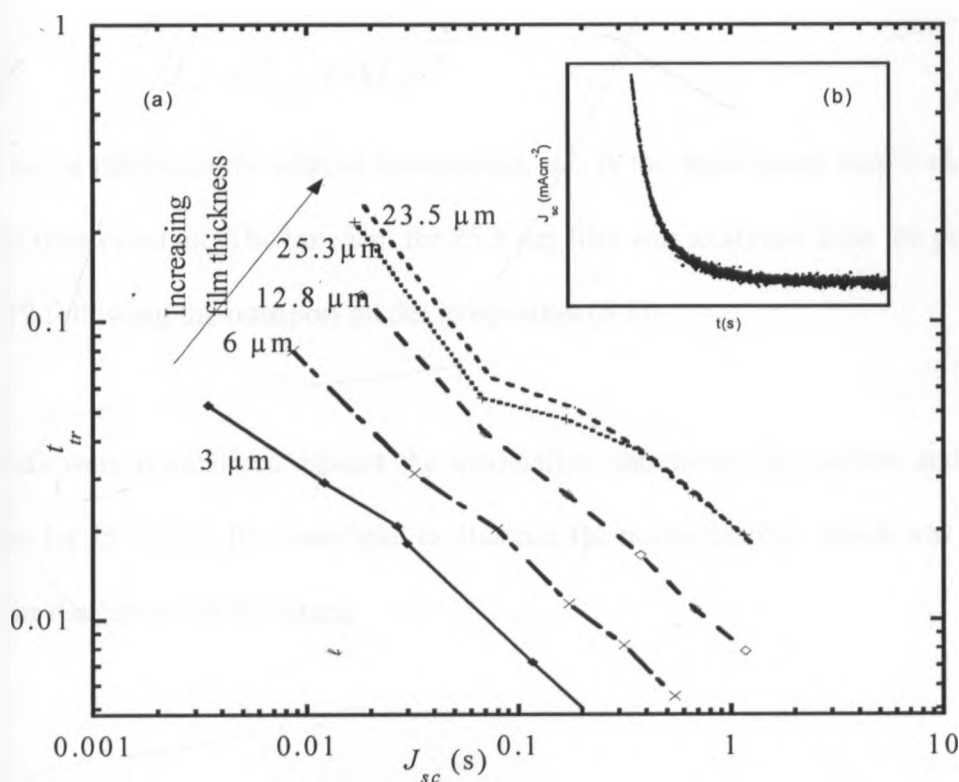


Figure 5.18: (a) Electron transport time (t_{tr}) as a function of short circuit current (J_{sc}) for samples of varying thickness on logarithmic scale and (b) typical current transient plot from which the transport time and offset current (j_{sc}) are obtained and plotted in (a).

It is observed that the transport time increased with the film thickness implying that thicker films had longer paths for electrons to traverse and hence increased total transport of the electrons to the collection point. As expected, thinner films had a short transport time owing to the fact that charge generation and collection are close and hence the photogenerated electrons do not travel long before they are collected. It can also be observed from figure 5.18a that the plots for all the samples had almost same gradient (plots are almost parallel) affirming the fact that all the films have a common rate constant for electron transport. It is the time at which the rate constant is attained that varies with film thickness. To get a clear analysis of this charge transport property as related to film thickness, electron transport of two samples (3.0 μm and 25.3 μm) are compared herein. First the transients were analyzed using the electron transport model (stated earlier in section 3.4):

$$J_{sc} = J_{sc,0} + \Delta J_0 e^{-\frac{t}{\tau_r}} \quad (5.3)$$

where $J_{sc,0}$ is the photocurrent without modulation, ΔJ_0 is the modulation amplitude and τ_r is the transport time constant. The transient for 25.3 μm film was analyzed from the presentation in figure 5.19 following the transport model in equation (5.3).

The transients were normalized against the modulation parameters for current and for time. The transient for 25.3 thick film was used to illustrate the normalization, which was applied to the results for the rest of the thickness.

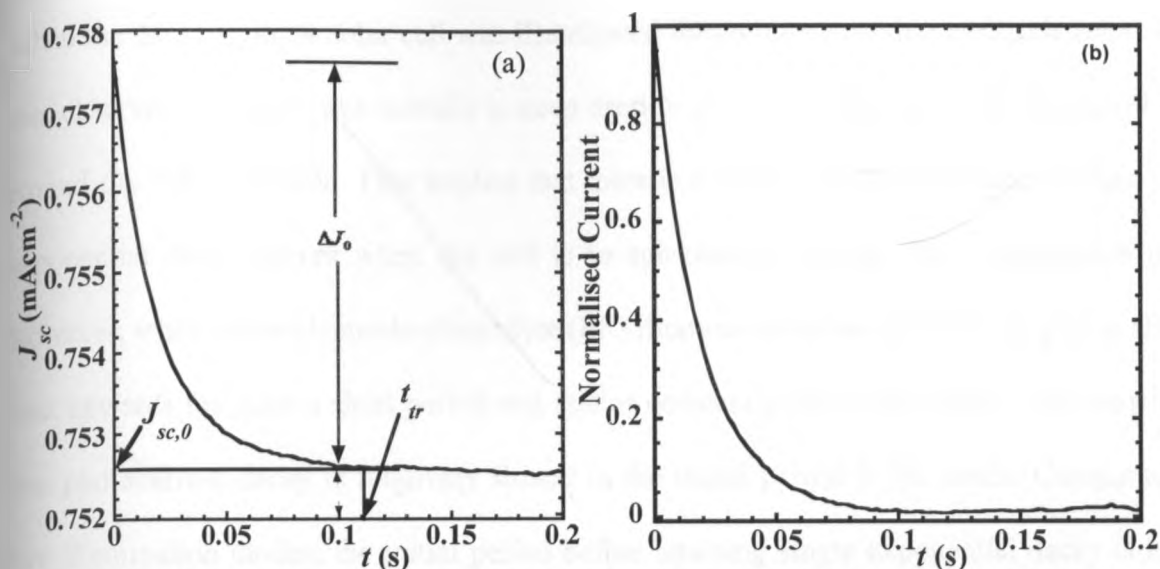


Figure 5.19: Current transients for 25.3 μm thick film at 15.6 mWcm^{-2} illumination intensity. (a) is the raw data and (b) is obtained from (a) by normalizing it with respect to parameters $J_{sc,0}$, t_{tr} and ΔJ_0 .

Figure 5.20 shows the normalised transients for 3.0 μm and 25.3 μm film thickness and plotted on a logarithmic scale.

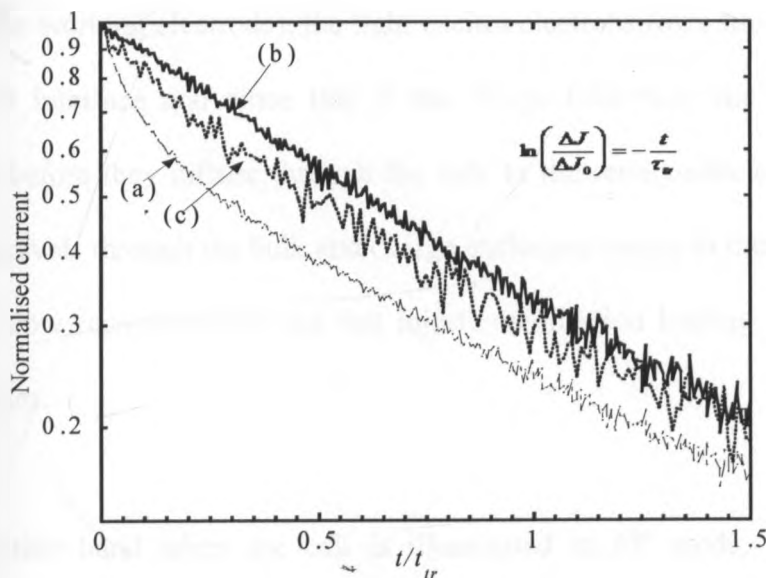


Figure 5.20: Normalized current transients of (a) illumination through the working electrode (SE), (b) illumination through the counter-electrode (EE) for a 25.3 μm thick film and (c) illumination through the working electrode (SE) for 3.0 μm thick film plotted on a semi logarithmic scale. Inset is the model on which the plots are based.

When the 25.3 μm thick solar cell was illuminated through the working electrode (plot (a)), it was observed that there was initially a steep drop in the decay followed by levelling off from around $t/t_r = 0.3$ onwards. This implies that there is a faster photocurrent decay before single exponential decay occurs when the cell is in substrate-electrolyte (SE) illumination mode. However, when under electrode-electrolyte (EE) illumination mode (plot b), the plot is slightly bent upwards for quite a short period and attains constant gradient thereafter. This may imply that photocurrent decay is relatively slower in the initial period in EE mode. Comparing the two illumination modes, the initial period before attaining single exponential decay is longer for SE than for EE illumination.

The difference in the times the single exponential is attained between SE and EE illumination modes may be explained as follows: For a 25.3 μm thick film in SE mode (that is, illumination through the working electrode), the light excites electrons from sites that are very close to the TiO_2/TCO interface and since this is the charge collection site, they are instantaneously collected before they diffuse through the bulk to the semiconductor electrolyte interface. As the light travels through the bulk and charge excitation occurs in the bulk, a balance is attained between slow recombination and fast injection/collection leading to a single exponential at longer times.

On the other hand when the cell is illuminated in EE mode, the light strikes first the semiconductor/ electrolyte interface (SEI) and the excited electrons must diffuse through the bulk before they reach the TiO_2/TCO interface to be collected. Fewer electrons will arrive before a balance between the slow recombination and collection is attained (the single

exponential explained above). This explains the short duration of fast decay observed in EE mode for shorter time scales (plot (b) in figure 5.20).

The case is different for the 3.0 μm thick film where the illumination from either side does not show the difference in the exponential decays (plot c in fig 5.20). For this film, the case is similar to that for the 25.3 μm film in EE illumination where in short time scales the decay is not rapid. This may be explained by the fact that when the cell is illuminated, charge generation, diffusion, and collection are all balanced as well as recombination with the redox electrolyte. As a result there is a single exponential both for shorter and longer time scales. Since the concentration of electrons in the conduction band determines the quasi Fermi level (${}_nE_f$) of a semiconductor, the decay profiles in figure 5.19 may give an indication of the variation of ${}_nE_f$ with the film thickness in different illumination modes. This is both at shorter and longer time scales of the decay as illustrated in figure 5.21.

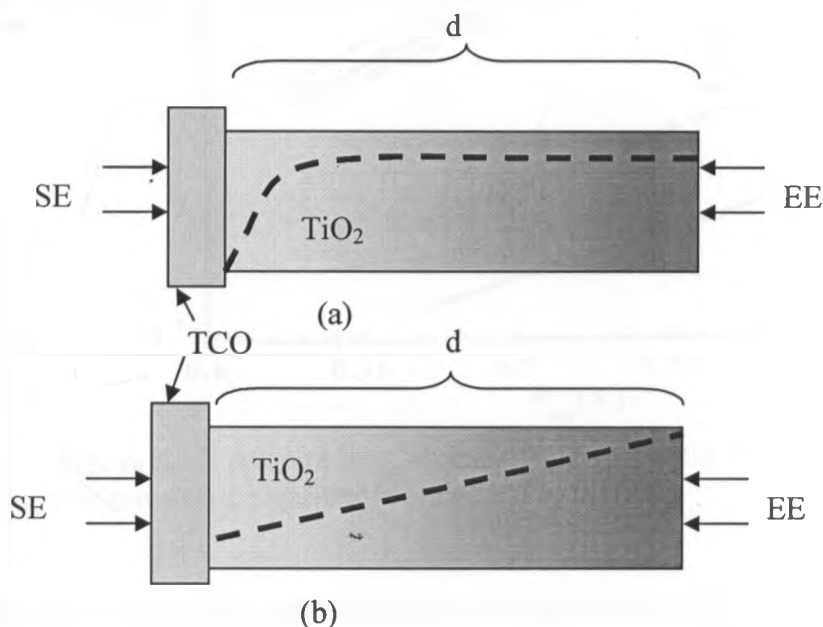


Figure 5.21: An illustration of the variation of quasi Fermi level (dashed line) with film thickness, d at (a) shorter and (b) longer time scales. SE and EE are illumination modes through the working electrode and counter electrode, respectively.

At shorter time scales (figure 5.21a), nE_f has an exponential rise close to the TiO_2/TCO interface (which is the charge collection site) and it becomes constant with film thickness deeper in the bulk. This is the case both for SE and EE illumination modes. At longer time scales, the variation is perceived to be linear across the film and is well pronounced in thinner films (the profile next to the TiO_2/TCO interface).

Figure 5.22 shows the log of accumulated charge against varying V_{oc} for different film thickness.

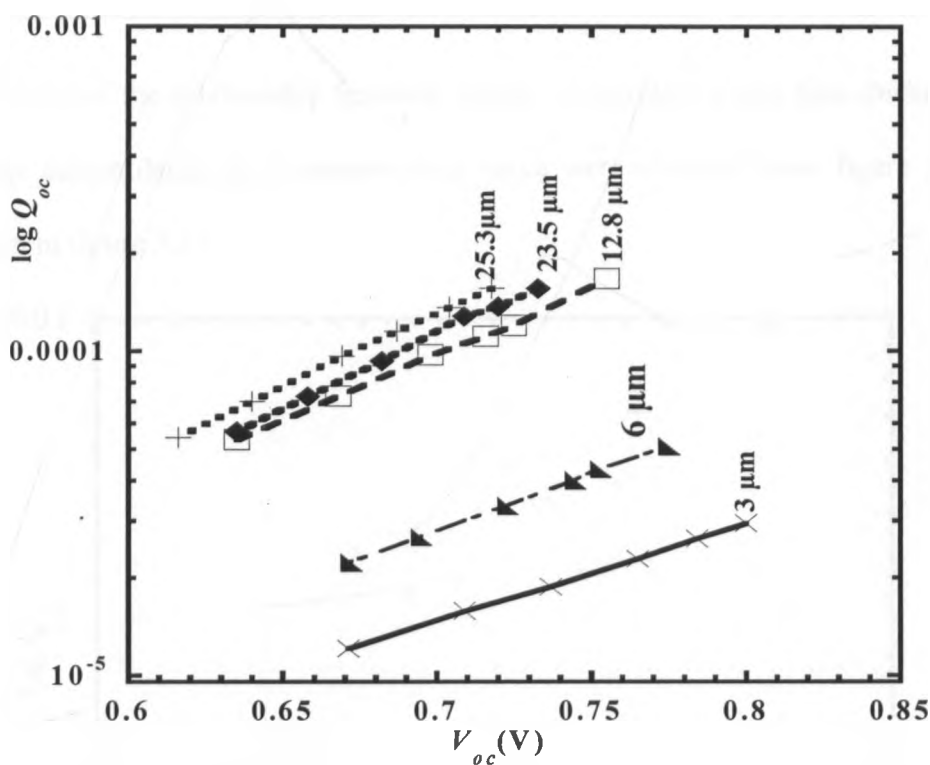


Figure 5.22: Accumulated charge (Q_{oc}) at different V_{oc} for different thickness on a logarithmic scale.

It is observed that the charge accumulation increased linearly with increase in film thickness. Charge accumulation in the bulk has been attributed to trap states (Westermarck *et. al.*, 2002). Therefore the linear profile in figure 5.22 implies that there is an exponential rise in charge

accumulation with increase in film thickness, which may be attributed to the exponential increase in trap states with increase in film thickness. Since the concentration of electrons in the traps is directly related to the concentration of conduction band electrons, it also suggests that with increase in film thickness, there is an exponential rise in the concentration of conduction band electrons. This is based on the multiple trapping (MT) model (Schlichthorl, *et. al.*, 1999; Kambili, *et. al.*, 2002) where most electrons are believed to be localized in traps hence the charge accumulation measure gives an estimate in this distribution function of the electrons.

To get a clear view of the relationship between charge accumulation and film thickness, the values of charge accumulation at a common bias value were obtained from figure 5.22 and plotted as shown in figure 5.23.

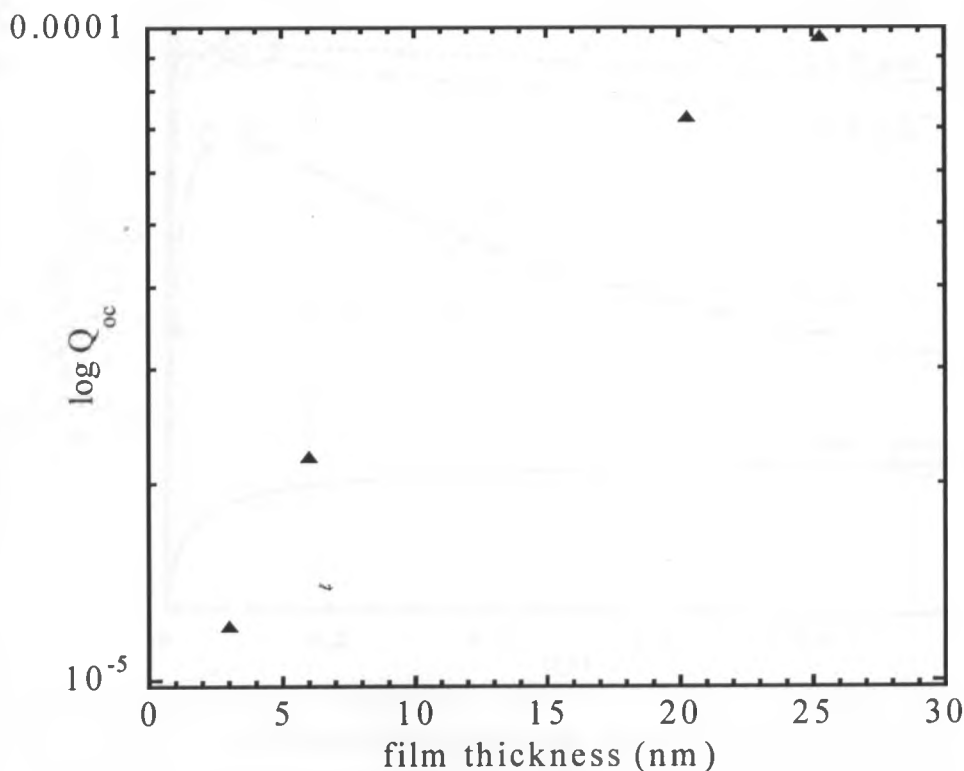


Figure 5.23: Relationship between charge and film thickness obtained from figure 5.20 at V_{oc} of 0.67V for all thicknesses.

At a common bias potential (0.67 V in this case), it can be observed from figure 5.23 that there is an exponential rise in charge accumulation with increase in film thickness. This is in agreement with the suggestion that there is an exponential rise in trap states with increase in film thickness as earlier discussed. The choice of a common bias potential for all the films was considered so that it validates the comparison because it is expected that at that point, the samples across the thickness profile have the same basis for comparison (i.e. common potential).

Results of electrochemical potential studies on the solar cells are shown in figure 5.24. The voltage observed in this set up was referred to in this discussion as the internal voltage while the maximum voltage attained was named V_{sc} .

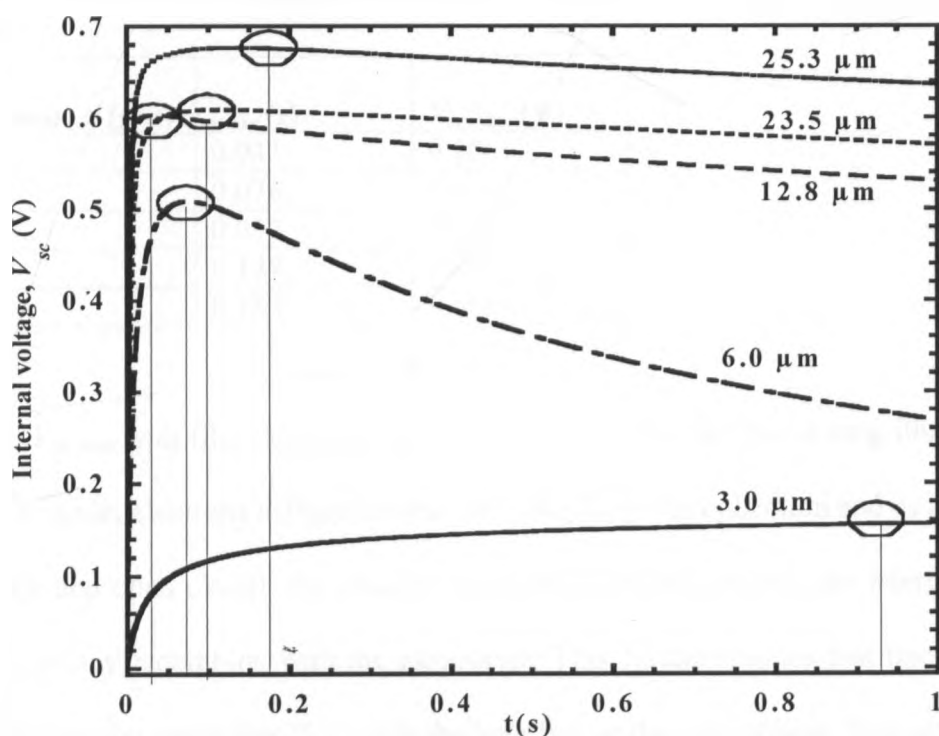


Figure 5.24: Internal voltage decay curves at a constant illumination of 15.6 mWcm^{-2} for different film thicknesses. The circles show the point at which the cell reaches $V_{sc, max}$ and the vertical lines drop to the x-axis to give t_{max} (time taken for the cell to reach $V_{sc, max}$).

From the results, $V_{sc, max}$ (indicated by circles in figure 5.24) increased with increase in film thickness while t_{max} decreased with increase in film thickness up to the 12.8 μm thick film then it started increasing again for films above 12.8 μm . $V_{sc, max}$ for 3.0 μm thick film was not distinctively observed possibly owing to the fact that in very thin films, electrons get recombined with the redox electrolyte before $V_{sc, max}$ is attained. Since the solar cell is in short circuit mode, at the time when it is under illumination, the electrons are continuously generated and collected almost instantly hence the potential build up does not happen. When the cell is switched to open circuit and in the dark, the electrons recombine immediately with the redox electrolyte hence no pronounced $V_{sc, max}$ is observed. The $V_{sc, max}$ and t_{max} obtained in figure 5.24 are tabulated in Table 5.5 for cell illuminated at 15.5mWcm^{-2} .

Table 5.5: Relationship between t_{max} and film thickness at 15.5mWcm^{-2} illumination.

Film Thickness, d (μm)	t_{max} (s)	$V_{sc, max}$ (V)
3.0	0.943	0.166
6.0	0.076	0.509
12.8	0.032	0.603
23.5	0.127	0.627
25.3	0.183	0.669

The increase in $V_{sc, max}$ with film thickness can be attributed to the fact that during illumination and short circuit mode, electrons diffuse towards the TiO_2/TCO for collection and as the cell is switched to dark and open circuit, the charges continue to diffuse towards the interface for a short time before they recombine with the electrolyte. This further implies that thicker films collect more charges (hence higher $V_{sc, max}$) in the bulk before they recombine. This also brings in the concept of trap states earlier discussed, (i.e., an increase in film thickness leads to increase in trap states). An interesting observation was made in the variation of t_{max} with film

thickness at constant illumination intensity (figure 5.24). A decrease in t_{max} with increase in film thickness between 3.0 μm and 12.8 μm was observed then a rise in t_{max} beyond 12.8 μm . This observation can be due to the effect of charge recombination via the electrolyte and it is more pronounced in the 3.0 μm thick film. It can be said, in general, that recombination via the redox electrolyte increases with increase in film thickness. This offers a competition with charge transport and collection and the optimum is around 12 μm as was also observed in the charge transport studies.

To study further the processes that take place in the solar cell when it is subjected to this procedure, results of internal potential decay at different illumination intensities for 25.3 μm thick film are presented in figure 5.25 and discussed below.

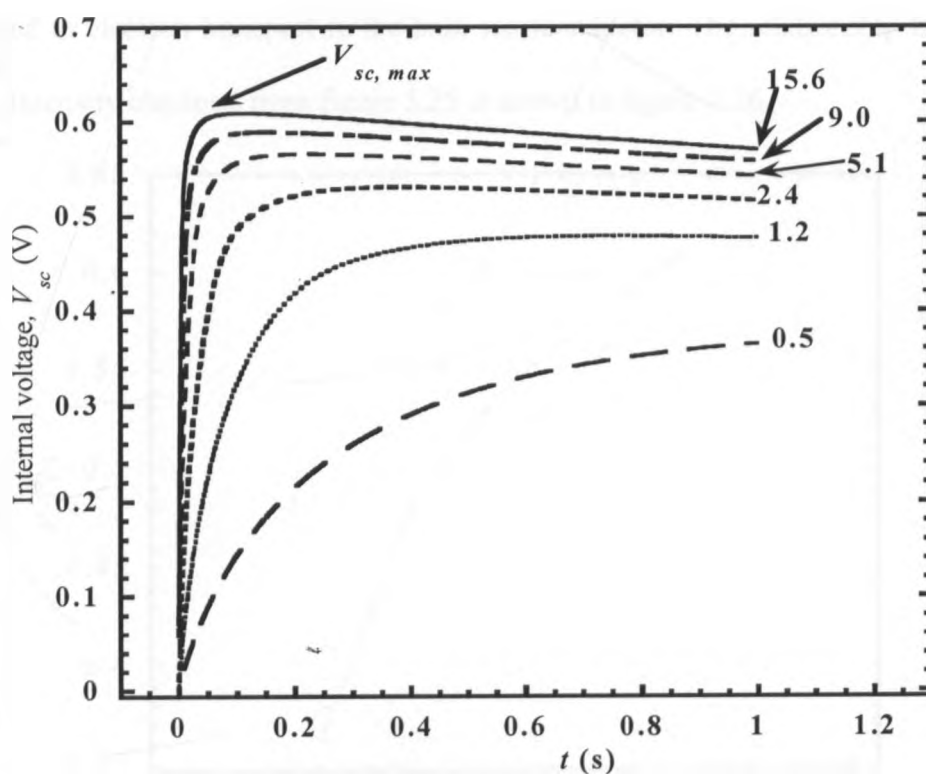


Figure 5.25: Internal voltage decay curves for 25.3 μm thick film at varying intensity (in mWcm^{-2}) obtained by varying the light source bias voltage.

It can be deduced from figure 5.25 that $V_{sc, max}$ depends on the prior illumination intensity and it is obtained after a time, t_{max} , which gets shorter as the illumination intensity is increased. As earlier mentioned in section 3.4.3, $V_{sc, max}$ represents the charge that is left in the bulk material after illumination has been turned off, which is also an indication of the position of the quasi-Fermi level inside the film. This implies that the quasi-Fermi level increases with the prior illumination intensity before the cell is turned to dark and open circuit. Boschloo and Hagfeldt, (2005) reported a similar trend, which was attributed to electrochemical potential of the cell, which is composed of electrostatic and chemical (concentration difference) contributions, as the driving force for electron transport. The case may be similar in our case since earlier on, it was observed that t_{max} was shortest for the film of thickness $12.8 \mu\text{m}$ which had been found to have the best overall efficiency and highest photocurrent density. Those two cases were directly related to electron transport in the bulk semiconductor. The relationship between $V_{sc, max}$ and light intensity obtained from figure 5.25 is shown in figure 5.26.

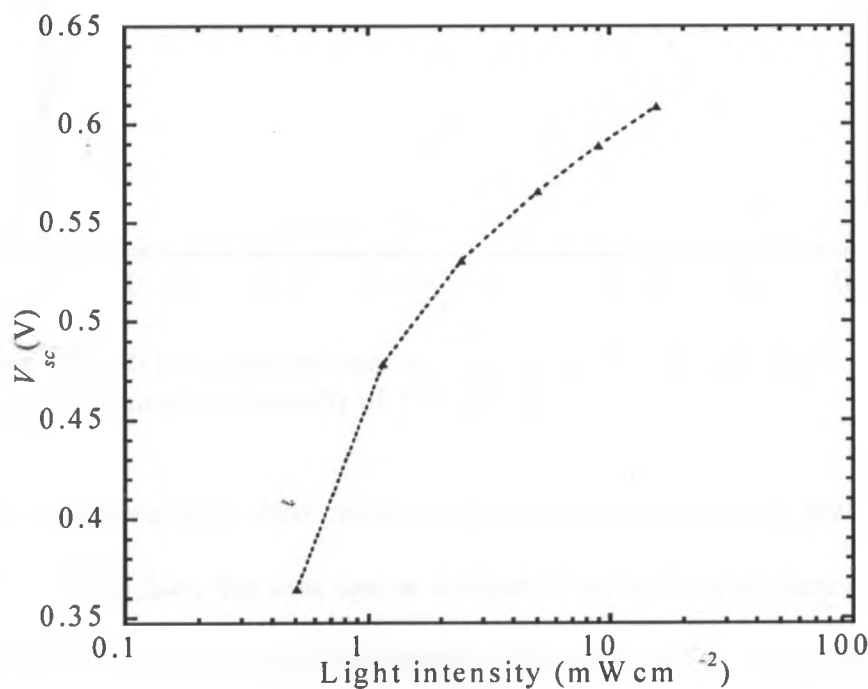


Figure 5.26: Maximum voltage ($V_{sc, max}$) as a function of light intensity for $25.3 \mu\text{m}$ thick film.

The observation here is that $V_{sc, max}$ exhibits logarithmic increase with light intensity, which may imply that the quasi-Fermi level increases with the illumination intensity, basing on the assumption that each photon generates an electron. It clearly shows that at higher intensities, more electrons are generated and hence a higher quasi-Fermi level is attained.

Figure 5.27 shows t_{max} as a function of $V_{sc, max}$. In this set up, t_{max} corresponds to the time required to obtain a uniform distribution of the electrons in the film.

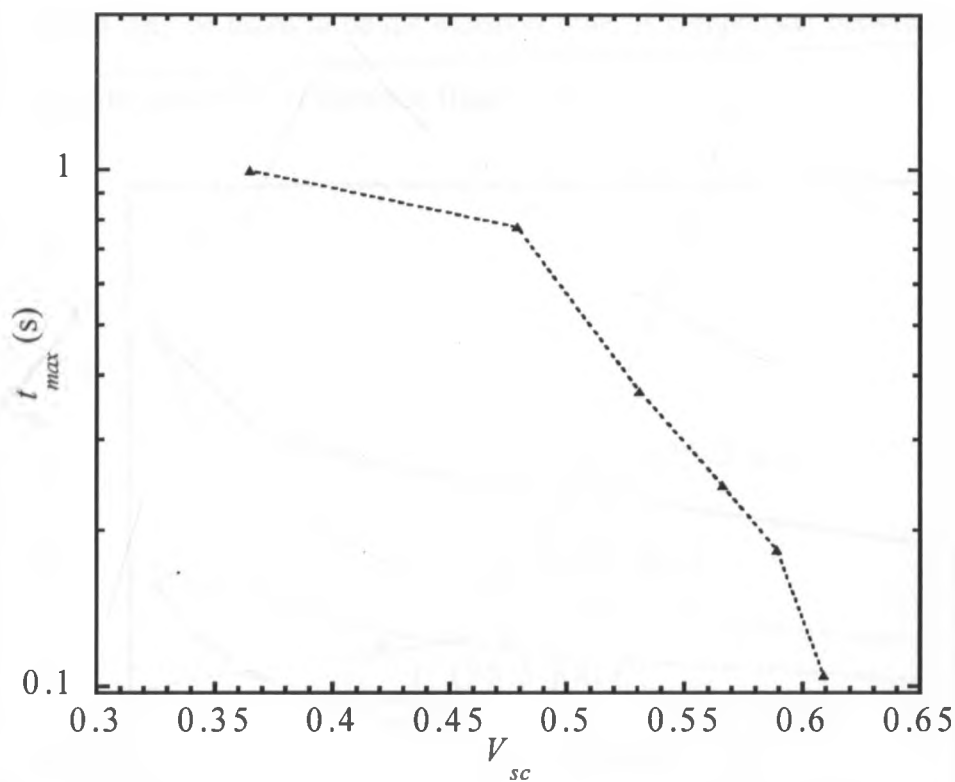


Figure 5.27: Relationship between t_{max} and $V_{sc, max}$ for 25.3 μm thick film at an illumination intensity of 15.5 mWcm^{-2} .

When the cell is switched from short circuit to open circuit and assuming that recombination occurs uniformly in the film, this time can be considered to be transport time and the relation between t_{max} and $V_{sc, max}$ appears to be exponential. This is because in short circuit mode (with illumination from any side), the injected electron will travel inside the TiO_2 film to the TCO to

be collected. In this mode and with continuous illumination and in equilibrium, there is a balance between recombination and collection. But when the cell is switched to open circuit and the light is switched off, it is expected that recombination takes over immediately and one would observe an instant decay of the voltage with time. Instead there is a rise in the voltage for some time to a maximum voltage then the decay begins. This may imply that as the cell is switched from short circuit to open circuit and in dark, the charges will continue moving across the film towards the TCO before recombination takes over. Therefore the time at which $V_{sc, max}$ is attained may be taken to be the transport time. A comparison between the transport time and t_{max} for the same film is shown in figure 5.28.

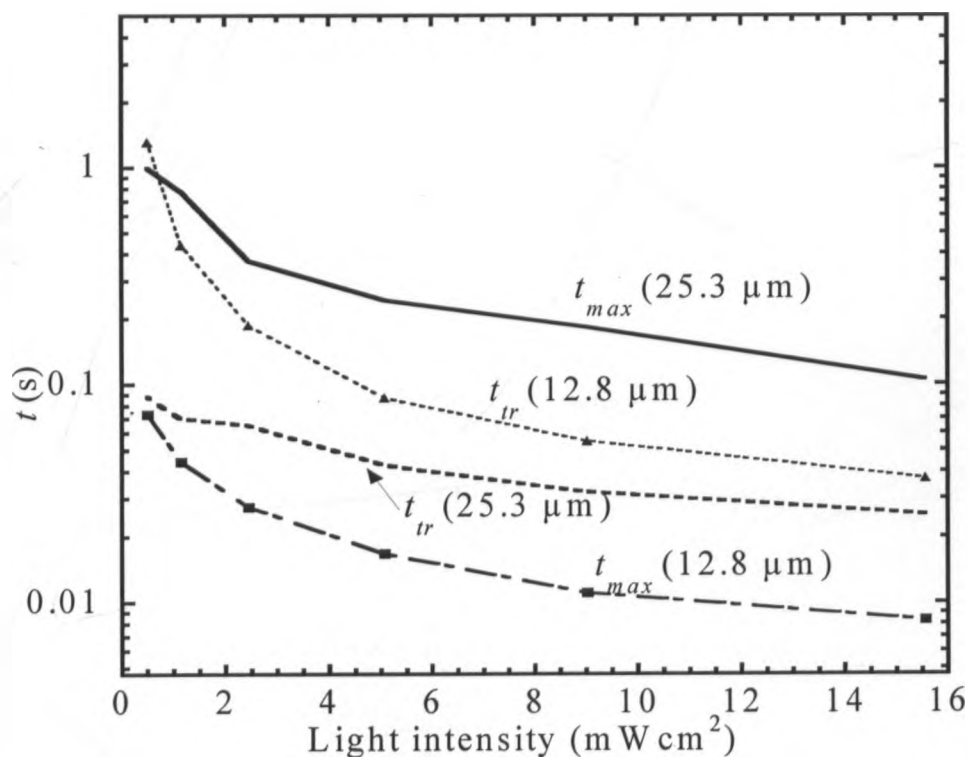


Figure 5.28: Comparison of t_{max} with transport time (t_{tr}) obtained from IMPS at varying illumination intensity for 12.8 and 25.3 μm thick film.

From the figure it can be seen that electron transport (t_{tr}) and t_{max} (the time it takes for $V_{sc, max}$ to be attained) both vary exponentially with the illumination intensity. It is expected that t_{max}

and t_{ir} be the same as earlier discussed in the preceding paragraph. However, t_{max} is on average higher than t_{ir} with almost a constant value for all the intensities. The difference between t_{max} and t_{ir} could be due to the effect of recombination process that takes place in electrochemical potential and IMPS studies. Higher t_{max} implies that there was a slow charge transport in the bulk after the cell was set to dark and open circuit mode. Therefore the difference contradicts the earlier assumption that charge recombination occurs uniformly in the bulk. It means that there was a high recombination rate when the cell was switched to dark and open circuit as compared to when IMPS was performed.

Chapter Six

Conclusion and Suggestions for Further Studies

6.1 Conclusion

A complete dye sensitized electrochemical solar cell employing anthocyanin dye pigment has been fabricated by screen printing method. Screen printing method was found to be reproducible and the solar cells sustained charge for long period since they were effectively sealed using the surlyn thermoplastic sealant. This method has proved to be viable for commercial up scaling since many cells were able to be coated at any one time.

The anthocyanin pigment investigated in this work showed qualities of a good sensitizer, i.e., it was able to change from the LUMO level to HOMO and consequently perform charge transfer from the HOMO level to the conduction band of TiO_2 semiconductor. However, the dye showed low absorption characteristics with the absorption maximum shifting from around 550 nm to 560 nm before and after being adsorbed on the semiconductor, respectively. The absorption maximum at 550 nm for the dye in solution indicated a strong presence of delphinidin molecule which is a principal compound in anthocyanins. The red shift to 560 nm was attributed to the chelating effect between the dye molecule and the Ti^{4+} on TiO_2 which causes the anthocyanin molecule to shift from the stable flavilium state to the unstable quinoid state. The best solar cell in terms of absorption, *I-V* and *IPCE* characteristics was one with dye at pH 2.0 implying that anthocyanin dye pigment is most stable at that pH which corresponds to the stable flavilium state the molecule exists in when in acidic medium. From photoelectrochemical studies, anthocyanin dye molecule was found to perform regeneration via the redox electrolyte by accepting an electron from I⁻. The results for the solar cell at this

pH were comparable with ruthenium N719 based solar cell with a major difference being observed in the maximum *IPCE* recorded (4% at 560 nm for anthocyanin sensitized solar cell and 25.5% at 540 nm for ruthenium N719 based solar cell).

In the study of the effect of film thickness, it can be concluded that the quasi-Fermi level in a semiconductor rises rapidly in very thin films while in thicker films it is almost constant across the thickness. On the other hand, charge transport and collection at the TiO_2/TCO interface compete with recombination at the $\text{TiO}_2/\text{electrolyte}$ interface where recombination is higher than the two at very thin and very thick films. The optimum film thickness was found to be around 12 μm . This gave the highest short circuit photocurrent density as well as overall efficiency. The concentration of conduction band electrons was found to be affected by contributions of trapping-detrapping and charge transfer recombination mechanisms.

Illumination direction was also found to have an effect on the charge transport in the film where thick films exhibited faster photocurrent decay at shorter time scales which changed to a single exponential at longer time scales, for backside illumination. In general for either illumination modes or thicker films, the quasi-Fermi level rises exponentially near the TCO/TiO_2 interface at the onset of illumination and at longer time scales, it is perceived to be linear across the film thickness profile. Charge transport time measured by electrochemical potential method was compared to transport time obtained by IMPS and found to differ by a constant figure at higher light intensities. The difference was attributed to the kind of recombination that takes place when the cell is switched to open circuit and observing charge transport, and the slow diffusion process for charges when in this state.

This study has attempted to bring an understanding to various aspects about charge transport in DSC by providing an explanation to the trends that were observed during the experiments. It has also been determined that the optimal film thickness for screen printed TiO₂ coupled with I⁻/I₃⁻ for efficient charge transport is between 12 to 15 μm. The study on anthocyanin dyes has shown that the natural pigment performs chelation with titanium dioxide and performs charge excitation to the conduction band of TiO₂. Its performance has been comparable to ruthenium N719 dye complex and hence can be considered as an alternative sensitizer for dye sensitized solar cells.

6.2 Suggestions for Further Research

Dye sensitized solar cell research still has many areas that need to be looked in both at fundamental and technological (up scaling) level. However with regard to the work that was carried out in this thesis, the following areas need further studies:

1. Electron transitions of anthocyanin dyes:

The study of molecular transitions of anthocyanin dyes using density functional theories (DFT) may show the level the dye molecule attains when in ground and excited states. With such information, the molecules' HOMO levels can be tuned to be at favourable level with TiO₂ conduction band hence improving on the efficiency of dye injection.

2. Synthesis of anthocyanin dyes:

Anthocyanin dyes have been used as sensitizers in their natural form and the limitations in terms of absorption characteristics have been noted. There is a possibility of synthesizing other organic dyes and blending in the anthocyanins in a well co-ordinated manner such that the new hybrid sensitizer can expand the absorption maximum and also increase the maximum beyond what has so far been achieved. This will hence lead to improvement in the absorption and overall efficiency of the dye.

3. Charge transport in TiO₂:

Studies in this thesis have explained the processes of charge transport in TiO₂ semiconductor under various conditions. It has been concluded that the optimal film thickness for charge transport in the TiO₂ semiconductor under various conditions is around 12 μm – 15 μm. However, there is still room for studies to be carried out in order to understand the processes at thicknesses beyond 30 μm. The study can be extended to samples sensitized with anthocyanin pigments to further observe the effect of porosity and surface adsorption of the dye molecules on the performance of TiO₂ at varying film thickness.

4. Fermi level studies vs. film thickness:

The Fermi levels have been studied through the observation of electron density in the semiconductor for various film thicknesses. This has been an approximation basing on the processes that take place at different film thickness. The accurate Fermi level can be studied by either using DFT or core level photoelectron spectroscopy analyses, which can help in optimising parameters such as film thickness to have an improved charge transport in the mesoporous structure.

5. Up scaling:

The technology used in coating TiO_2 films has demonstrated the viability of producing dye solar cells at a medium scale. Further research can be done on new coating methods such as coating on flexible substrates and rolling techniques.

Finally as highlighted in these few suggested researches, it may be realised that DSC research is multi-disciplinary area touching on chemistry, biology and physics, therefore there is need for co-operation between the mentioned areas in order to realise the goal of producing a cheap and highly efficient solar cell in the near future.

REFERENCES

Albery, W. J. and Bartlett, P. N. The transport and kinetics of photo-generated carriers in colloidal semiconductor electrode particles. *Journal of the Electrochemical Society*, **131**, 1984, 315.

Andreas, K. Solar cells based on dye-sensitized nanocrystalline TiO₂ electrodes. PhD. Thesis No. 1214, Ecole Polytechnique Federale de Lausanne, Switzerland, 1994.

Barbe, C., Arendse, J. F., Comte, P., Jirousek, M., Lenzmann, F., Shklover, V. and Grätzel, M. Nanocrystalline titanium oxide electrodes for photovoltaic applications. *Journal of American Ceramic Society*, **80**(12), 1997, 3157.

Bard, A. J. and Faulkner, L. R. Electrochemical methods: fundamentals and applications. 2nd ed. New York: Wiley & Sons, 2000.

Becquerel, E. M. On the colored photographic image of the solar spectrum. *Journal of the Franklin Institute*, 1848, 238.

Bird, G. Observations on the application of heliographic or photogenic drawing to botanical purposes; with an account of an economic mode of preparing the paper. *Journal of the Franklin Institute of the State of Pennsylvania, and Mechanics Register*, **24**(3), 1839, 202.

Bourdon, J. Spectral sensitization of chemical effects in solids. *Journal of Physical Chemistry*, **69**, 1965, 705.

Boschloo, G. and Hagfeldt, A. Activation energy of electron transport in dye-sensitized TiO₂ solar cells. *Journal of Physical Chemistry B*, **109**, 2005, 12093.

Boschloo, G., Häggman, L. and Hagfeldt, A. Quantification of the effect of 4-*tert*-butylpyridine: addition to I⁻/I₃⁻ redox electrolytes in dye-sensitized nanostructured TiO₂ solar cells. *Journal of Physical Chemistry B*, **110**, 2006, 13144.

Boschloo, G., Marinado, T., Nonomura, K., Edvinsson, T., Agrios, A., Hagberg, D. P., Sun, L., Quintana, M-E., Karthikeyan, C.S., Thelakkat, M. and Hagfeldt, A. A comparative study of a polyene-diphenylamine dye and Ru(dcbpy)₂(NCS)₂ in electrolyte-based and solid-state dye-sensitized solar cells. *Thin Solid Films*, **516**, 2008, 7214.

Cao, F., Oskam, G., Meyer, G. J. and Searson, P. C. Electron transport in porous nanocrystalline TiO₂ photoelectrochemical cells. *Journal of Physical Chemistry*, **100**, 1996, 17021.

Chapin, D. M., Fuller, C. S. and Pearson, G. L. A new silicon p-n junction photocell for converting solar radiation into electrical power. *Journal of Applied Physics*, **25**, 1954, 676.

Cherapy, N. J., Smestad, P., Grätzel, M. and Zhang, J. Ultrafast electron injection: implications for a photoelectrochemical cell utilizing an anthocyanin dye-sensitized TiO₂ solar nanocrystalline electrode. *Journal of Physical Chemistry B*, **101**, 1997, 9342.

Chiba, Y., Ashraful, I., Yuki, W., Ryoichi, K. Naoki, K., Liyuan, H. Dye-sensitized solar cells with conversion efficiency of 11.1%. *Japanese Journal of Applied Physics*, **45**(25), 2006, L638.

Daguerre, L. Practical definition of daguerrotype. *Journal of the Franklin Institute*, 1839, 303.

De Angelis, F., Fantaccil, S and Selloni, A. Alignment of the dye's molecular levels with the TiO₂ band edges in dye-sensitized solar cells: a DFT-TDDFT study. *Nanotechnology*, **19**, 2008, 424002.

de Jongh, P. E. and Vanmaekelbergh, D. Trap-limited electronic transport in assemblies of nanometer-size TiO₂ particles. *Physical Review Letters*, **77**, 1996, 3427.

de Jongh, P. E. and Vanmaekelbergh, D. Investigation of the electronic transport properties of nanocrystalline particulate TiO₂ electrodes by intensity-modulated photocurrent spectroscopy. *Journal of Physical Chemistry B*, **101**, 1997, 2716.

de Jongh, P. E., Meulenkamp, E. A., Vanmaekelbergh, D. and Kelly, J. J. Charge carrier dynamics in illuminated, particulate ZnO electrodes. *Journal of Physical Chemistry B*, **104**, 2000, 7686.

Deb, S. K., Ferrere, S., Frank, A. J., Gregg, B. A., Huang, S. Y., Nozik, A.J., Schlichthorl, G. and Zaban, A. Photoelectrochemical cells based on dye-sensitization of nanocrystalline TiO₂. *Conference proceedings, NREL CP-450*, 1997, 22953.

Dloczik, L., Iluperama, O., Lauermann, I., Peter, L. M., Ponomarev, E. A., Redmond, G., Shaw, N. J. and Uhlendorf, I. Dynamic response of dye-sensitized nanocrystalline solar cells: characterization by intensity-modulated photocurrent spectroscopy. *Journal of Physical Chemistry B*, **101**, 1997, 10281.

Duffy N.W., Peter, L. M. and Wijayantha, K. G. U. Characterization of electron transport and back reaction in dye-sensitized nanocrystalline solar cells by small amplitude laser pulse excitation. *Electrochemistry Communications*, **2**, 2000a, 262.

Duffy, N.W., Peter, L. M., Rajapakse, R. M. G. and Wijayantha, K. G. U. A novel charge extraction method for the study of electron transport and interfacial transfer in dye sensitized nanocrystalline solar cells. *Electrochemistry Communications*, **2**, 2000b, 658.

Duonghong, D., Serpone, N. and Grätzel, M. Integrated systems for water cleavage by visible light; sensitization of titanium dioxide particles by surface derivatization with ruthenium complexes. *Helvetica Chimica Acta*, **6(4)**, 1984, 1012.

El Baraday, M. Nuclear power's changing picture. *IAEA Bulletin*, **49(1)**, 2007, 18.

Eppler, A.M., Ballard, I. M. and Nelson, J. Charge transport in porous nanocrystalline titanium dioxide. *Physica E*, **14**, 2002, 197.

European Commission. World energy technology outlook – 2050. Belgium: *Directorate-General for Research, Brussels*, 2006.

Ferber, J., Stangl, R. and Luther, J. An electrical model of the dye-sensitized solar cell. *Solar Energy Materials and Solar Cells* **53**, 1998, 29.

Fernando, J. M. R. C. and Senadeera, G. K. R. Natural anthocyanins as photosensitizers for dye-sensitized solar devices. *Current Science*, **95**(5), 2008, 663.

Fisher, A. C., Peter, L. M., Ponomarev, E. A., Walker, A. B., Wijayantha, K. G. U. Intensity dependence of the back reaction and transport of electrons in dye-sensitized nanocrystalline TiO₂ solar cells. *Journal of Physical Chemistry B*, **104**, 2000, 949.

Frank, A. J., Kopidakis, N. and Van de Lagemaat, J. Electrons in nanostructured TiO₂ solar cells: transport, recombination and photovoltaic properties. *Journal of Coordination Chemistry Reviews*, **248**, 2004, 1165.

Fujishima, A. and Honda, K. Electrochemical evidence for mechanism of the primary stage of photosynthesis. *Bulletin of the Chemical Society of Japan*, **44**, 1971, 1148.

Garcia, C. G., Polo, A. and Murakami, I. Photoelectrochemical solar cell using extract of *eugenia jambolana* as a natural sensitizer. *Annals of the Brazilian Academy of Sciences*, **75**(2), 2003, 163.

Grätzel M. Perspectives for dye-sensitized nanocrystalline solar cells. *Progress in Photovoltaics Research Applications*, **8**, 2000, 171.

Grätzel M. Photoelectrochemical cells. *Nature*, **414**, 2001, 338.

Grätzel, M. Dye-sensitized solar cells. *Journal of Photochemistry and Photobiology C: Photochemistry Reviews*, **4**, 2003, 145.

Grätzel, M. Solar energy conversion by dye-sensitized photovoltaic cells. *Inorganic Chemistry*, **44**, 2005, 6841.

Hagfeldt, A. Laser-induced photocurrent transients and capacitance measurements on nanocrystalline TiO₂ electrodes. *Solar Energy Materials*, **38**, 1995, pp. 339.

Hao, S., Wu, J., Huang, Y. and Lin, J. Natural dyes as photosensitizers for dye-sensitized solar cell. *Solar Energy*, **80**, 2006, 209.

Haque, S. A., Tachibana, Y., Klug, D. R., Durrant, J. R. Charge recombination kinetics in dye-sensitized nanocrystalline titanium dioxide films under externally applied bias, *Journal of Physical Chemistry B*, **102**, 1998, 1745.

Haque, S. A., Tachibana, Y., Willis, R. L., Moser, J. E., Grätzel, M., Klug, D. R. and Durrant, J. R. Parameters influencing charge recombination kinetics in dye-sensitized nanocrystalline titanium dioxide films. *Journal of Physical Chemistry B*, **104**, 2000, 538.

IEA. Key world energy statistics 2007. *International Energy Agency*, 2007.

Ingo, G. M., Dire S. and Babonneau, F. (1993). XPS studies of SiO₂-TiO₂ powders prepared by sol-gel process. *Applied Surface Science*, **70**(710), 1993, 230.

IPCC. Climate change 2007: the physical science basis: summary for policymakers. *Intergovernmental Panel on Climate Change Secretariat*, 2007.

Ito, S., Zakeeruddin, S. M., Humphry-Baker, R., Liska, P., Charvet, R., Comte, P., Nazeeruddin, M. K., Péchy, P., Takata, M., Miura, H., Uchida, S. and Grätzel, M. High-efficiency organic-dye-sensitized solar cells controlled by nanocrystalline TiO₂ electrode thickness. *Advanced Materials*, **18**, 2006, 1202.

Ito, S., Chen, P., Comte, P., Nazeeruddin, M. K., Liska, P., Péchy, P. and Grätzel, M. Fabrication of screen-printing pastes from TiO₂ powders for dye-sensitized solar cells. *Progress in Photovoltaic Research Applications*, **15**, 2007, 603.

Kambe, S., Nakade, S., Wada, Y., Kitamura, T. and Yanagida, S. Effects of crystal structure, size, shape and surface structural differences on photo-induced electron transport in TiO₂ mesoporous electrodes. *Journal of Material Chemistry*, **12**, 2002, 723.

Kambili, A., Walker, A. B., Qiu, F. L., Fisher, A. C., Savin, A. D. and Peter, L. M. Electron transport in the dye sensitized nanocrystalline cell. *Physica E*, **14**, 2002, 203.

Kim, S.Y., Simultaneous determination of refractive index, extinction coefficient and void distribution of TiO₂ thin films by optical methods. *Applied Optics*, **35**(34), 1996, 6703.

Kuang, D., Klein, C., Ito, C., Moser, J-E., Humphry-Baker, R., Evans, N., Durrant, F., Zakeeruddin, S. M. and Grätzel, M. High-efficiency and stable mesoscopic dye-sensitized solar cells based on a high molar extinction coefficient ruthenium sensitizer and nonvolatile electrolyte. *Advanced Materials*, **19**, 2007, 1133.

Kopidakis, N., Schiff, E. A., Park, N. G., Van de Lagemaat, J. and Frank, A. J. Ambipolar diffusion of photocarriers in electrolyte-filled, nanoporous TiO₂. *Journal of Physical Chemistry, B*, **104**, 2000, 3930.

Kopidakis, N., Benkstein, K. D., Van de Lagemaat, J. and Frank, A. J. Transport-limited recombination of photocarriers in dye-sensitized nanocrystalline solar cells. *Journal of Physical Chemistry B*, **107**, 2003, 11307.

Memming, R. Solar energy conversion by photoelectrochemical processes. *Electrochimica Acta*, **25**, 1980, 77.

Nazeeruddin, M.K., Kay, A., Humpbry-Baker, R., Miller, E., Liska, P., Vlachopoulos, N. and Grätzel, M. Conversion of light to electricity by cis-X₂Bis(2,2'-bipyridyl-4,4'-dicarboxylate)ruthenium(II) charge-transfer sensitizers (X = Cl⁻, Br⁻, I⁻, CN⁻, and SCN⁻) on nanocrystalline TiO₂ electrodes. *Journal of American Chemical Society*, **115**, 1993, 6382.

Nazeeruddin, M.K., Pe'chy, P., Renouard, T., Zakeeruddin, S.M., Humphry-Baker, S.M., Comte, P., Liska, P., Cevey, I., Costa, E. Shklover, V., Spiccia, E.L., C. A. Deacon, C.A., Bignozzi, D., Grätzel, M. Engineering of efficient panchromatic sensitizers for nanocrystalline TiO₂ based solar cells. *Journal of American Chemical Society*, **123**, 2001, 1613.

Nelson R.C. Minority carrier trapping and dye sensitization. *Journal of Physical Chemistry*, **69**, 1965, 714.

Nelson, J. Continuous time random-walk model of electron transport in nanocrystalline TiO₂ Electrodes. *Physical Review B*. **59**, 1999, 15374.

Nelson, J., Eppler A. M. and Ballard, I. M. Photoconductivity and charge trapping in porous nanocrystalline titanium dioxide. *Journal of Photochemistry Photobiology A*, **148**, 2002, 25.

Nelson, J. Physics of Solar cells. London: Imperial College, 2003, 30

Nelson, J. Physics of solar cells. *Lecture Notes for Winter College on Optics and Energy, ICTP*, **2132(2)**, 2010.

Nissfolk, J., Fredin, K., Hagfeldt, A. and Boschloo, G. Recombination and transport processes in dye-sensitized solar cells investigated under working conditions. *Journal of Physical Chemistry B*, **110(36)**, 2006, 17715.

Nissfolk, J. Charge Transport Processes in Mesoporous Photoelectrochemical Systems.

PhD Thesis, Royal Institute of Technology, Stockholm, Sweden, 2009, 11.

O'Regan, B., Moser, J., Anderson, M. and Grätzel, M. Vectorial electron injection into transparent semiconductor membranes and electric field effects on the dynamics of light-induced charge separation. *Journal of Physical Chemistry*, **94**, 1990, 8720.

O'Regan, B. and Grätzel, M. A low cost, high efficiency solar cell based on dye sensitized colloidal TiO₂ films. *Nature*, **353**, 1991, 737.

O'Regan B. and Lenzenmann F. Charge transport and recombination in a nanoscale interpenetrating network of n-type and p-type semiconductors: transient photocurrent and photovoltage studies of TiO₂/Dye/CuSCN photovoltaic cells. *Journal of Physical Chemistry B*, **108**, 2004, 4342.

Peter, L. M. and Wijayantha, K. G. U. Intensity dependence of the electron diffusion length in dye-sensitized nanocrystalline TiO₂ photovoltaic cells. *Electrochemical Communication*, **1**, 1999, 576.

Peter L.M., Duffy, N. W., Wang, R. L. and Wijayantha, K. G. U. Transport and interfacial transfer of electrons in dye-sensitized nanocrystalline solar cells. *Journal of Electroanalytical Chemistry*, **524**, 2002, 127.

Polo, A. S., Yukie, N. and Murakami I. Blue sensitizers for solar cells: natural dyes from calafate and jaboticaba. *Solar Energy Materials & Solar Cells*, **90**, 2006, 1936.

Pulka, H. K. Coatings on glasses. *Thin Film Science and Technology* **6**, 1984, 254.

Quirin S., Tollefson T., Scully, T., Witze, A. and Morton, O. Electricity without carbon. *Nature*, **454**, 2008, 816.

Reddy, B. M., Chowdhury, B. and Smirniotis, P. G. An XPS study of the dispersion of MoO_3 on $\text{TiO}_2\text{-ZrO}_2$, $\text{TiO}_2\text{-SiO}_2$, $\text{TiO}_2\text{-Al}_2\text{O}_3$, $\text{SiO}_2\text{-ZrO}_2$, and $\text{SiO}_2\text{-TiO}_2\text{-ZrO}_2$ mixed oxides. *Applied Catalysis A: General*, **211**, 2001, 19.

Remel, T., Gregory, R. and Baumert, B. Characterization of barium strontium titanate films using XRD, *International Centre for Diffraction Data*, 1999, 38.

Rensmo, H., Westermarck K., Södergren, S., Kohle, O., Persson, P., Lunell, S. and Siegbahn, H. XPS studies of Ru-polypyridine complexes for solar cell applications. *Journal of Chemical Physics*, **111**(6), 1999, 2744.

Sandell, A., Anderson, M. P., Alfredsson, Y., Johansson, M. K.-J., Schnadt, J., Rensmo, H., Siegbahn H. and Uvdal, P. Titanium dioxide thin-film growth on silicon .111. by chemical vapor deposition of titanium (IV) isopropoxide. *Journal of Applied Physics*, **92**(6), 2002, 3381.

Sandell, A., Andersson, M. P., Johansson, M. K.-J., Karlsson, P. G., Alfredsson, Y., Schnadt, J., Siegbahn, H. and Uvdal, P. Metalorganic chemical vapor deposition of anatase titanium dioxide on Si: Modifying the interface by pre-oxidation. *Surface Science*, **530**, 2003, 63.

Sandler, M. W. Photography, an illustrative history. New York: Oxford University Press, 2002, 117.

Schlichthorl, G. S., Huang, Y., Sprague, J. and Frank, A. J. Band edge movement and recombination kinetics in dye-sensitized nanocrystalline TiO_2 solar cells: a study by intensity modulated photovoltage spectroscopy. *Journal of Physical Chemistry B*, **101**, 1997, 8141.

Schlichthorl, G., Park, N-G. and Frank, A. J. Evaluation of the charge-collection efficiency of dye-sensitized nanocrystalline TiO_2 solar cells. *Journal of Physical Chemistry B*, **103**, 1999, 782.

Shi, D., Pootrakulchote, N., Li, R., Guo, J., Wang, Y., Zakeeruddin, M., Grätzel, M. and Wang, P. New efficiency records for stable dye-sensitized solar cells with low-volatility and ionic liquid electrolytes. *Journal of Physical Chemistry C*, **112**(44), 2008, 17047.

Shockely, W. and Read, W. T. Statistics of the recombination of holes and electrons, *Physical Review* **87**(5), 1952, 835.

Smestad, G. Education and solar energy conversion: demonstrating electron transfer. *Solar Energy Materials and Solar Cells*, **55**, 1998, 157.

Södergren, S., Hagfeldt, A., Jorgen, O. and Lindquist, S-E. Theoretical models for action spectrum and the current-voltage characteristics of microporous semiconductor films and PEC cells. *Journal of Physical Chemistry*, **98**, 1994, 5552.

Solbrand, A., Lindstrom, H., Rensmo, H., Hagfeldt, A., Lindquist, S-E. and Sodergren, S. Electron transport in the nanostructured TiO₂ electrolyte system studied with time-resolved photocurrents. *Journal of Physical Chemistry B*, **101**, 1997, 2514.

Solbrand, A., Henningsson, A., Sodergren, S., Lindstrom, H., Hagfeldt, A. and Lindquist, S-E. Charge transport properties in dye-sensitized nanostructured TiO₂ thin film electrodes studied by photo-induced current transients. *Journal of Physical Chemistry*, **103**, 1999, 1078.

Suryanarayana, C. and Norton, G. X-ray diffraction: a practical approach. New York: Plenum Press, 1998, 52.

Sze, S. M. Physics of semiconductor devices. New York: Wiley International Publishers Inc., 1981, 122.

Tang H., Berger, S., Schmid, P.E., Levy, F. Optical properties of anatase TiO₂. *Solid State Communications*. **92**, 1994, 267.

Tennakone, K., Kumarasinghe, A. R., Kumara, G. R. R. A., Wijayantha, K. G. U. and Sirimanne, M. Nanoporous TiO₂ photoanode sensitized with the flower pigment cyanidin. *Journal of Photochemistry and Photobiology A*, **108**, 1997, 193.

Tennakone, K., Kumara, G. R. R. A., Kottegoda, R. M., Wijayantha, K. G. U. and Perera, U. P. S. A solid state photovoltaic cell sensitized with a ruthenium bipyridyl complex. *Journal of Physics D: Applied Physics*, **31** 1998, 1492.

Tributsch, H. Application of electrochemical kinetics to photosynthesis and oxidative phosphorylation: the redox element hypothesis and the principle of parametric energy coupling. *Bioenergetics*, **2**, 1971, 249.

Van de Lagemaat, J. and Frank, A. J. Effect of the surface-state distribution on electron transport in dye-sensitized TiO₂ solar cells: nonlinear electron-transport kinetics. *Journal of Physical Chemistry B*, **104**, 2000, 4292.

Van de Lagemaat, J. and Frank, A. J. Non-thermalized electron transport in dye-sensitized nanocrystalline TiO₂ films: transient photocurrent and random-walk modeling studies. *Journal of Physical Chemistry B*, **105**, 2001, 11194.

Verma, H. R. Atomic and nuclear analytical methods. Berlin: Springer Berlin, 2007, 213.

Wang, Z-S., Cui, Y., Hara, K., Dan-oh, Y., Kasada, C. and Shinpo, A. A high light-harvesting-efficiency coumarin dye for stable dye-sensitized solar cells. *Advanced Materials*, **19**, 2007, 1138.

Westermarck, K., Henningsson, Å., Rensmo, H., Sodergren, S., Siegbahn, H and Hagfeldt A. Determination of the electronic density of states at a nanostructured TiO₂/Ru-dye/electrolyte interface by means of photoelectron spectroscopy. *Chemical Physics*, **285**, 2002, 157.

Williams, R. Becquerel photovoltaic effect in binary compounds. *Journal of Physical Chemistry*, **32** (5) 1960, 1505.

Wongcharee, K., Meeyoo, V. and Chavadej, S. Dye-sensitized solar cell using natural dyes extracted from rosella and blue pea flowers. *Solar Energy Materials & Solar Cells*, **91**, 2007, 566.

Würfel, P. Physics of solar cells: from principles to new concepts. Verlag: Willey-UCH, 2005, 23.

Yoshida, T., Shinada, A., Oekermann, T., Sugiura, T., Sakai, T. and Minoura, M. Time and frequency-resolved photoelectrochemical investigations on nano-honeycomb TiO₂ electrodes. *Electrochemistry*, **70**, 2002, 453.

Zaban, A., Greenshtein, M. and Bisquert, J. Lifetime in nanocrystalline dye solar cells by open-circuit voltage decay measurements. *Chemphyschem*, **4**, 2003, 859.

APPENDICES

Appendix I

LabVIEW Development & Implementation

A1.0 Introduction

In this section, the development of an automated *I-V* and *IPCE* characterization using LabVIEW™ is presented. This is because these two systems were developed to full automation as part of the whole project and thereafter the systems were used to collect data.

LabVIEW (Laboratory Virtual Instruments Electronic Workbench) from National Instruments Inc. (USA) is an application that provides a graphical environment for signal acquisition, measurement, data analysis and presentation by means of an interface between a physical device and the application. LabVIEW programs are called virtual instruments (VIs) because their appearance and operation imitate physical instruments, such as oscilloscopes and multimeters. It contains a comprehensive set of tools for acquiring, analyzing, displaying, and storing data, as well as tools to help one troubleshoot the codes. The interface is built (known as the front panel) which has controls and indicators. Controls can be knobs, push buttons, dials and other input devices while indicators can be graphs, LEDs and other displays. Alongside the front panel is a block diagram, which contains the code to control the front panel objects.

A1.1 Communication Protocol

LabVIEW™ communicates with physical devices through hardware such as data acquisition devices (DAQ's), GPIB, RS-232, etc. The group of instruments that communicate through these protocols have a group of commands known as Standard Commands for Programmable

Instruments (SCPI). This program has been applied here to perform measurement of current and voltage and plot the characteristics. From the characteristics, the Fill Factor (FF) and efficiency is determined. Communication is through GPIB via interface card.

The physical instruments are controlled through a VISA program, Instrument I/O assistant or Instrument Drivers. VISA programs and Instrument I/O assistant use the low level programming language that needs to be developed from the basics. On the other hand instrument drivers are a set of high level programming functions that have been compiled and put together to a VI (equivalent of a routine in text based programming). Most of the instrument vendors have liased with National Instruments to produce specific instrument drivers for their products. For example an oscilloscope from Tektronik or a Keithley 2400 source meter from Keithley Inc have their respective instrument drivers available from National Instruments.

In this report instrument drivers were used as a means of communication with the physical instruments (Keithley 2400 source meter) and acquire and measure the output from the solar cell for device I - V characterization.

A1.2 Automation of I - V Characterization System

The flow chart of events is given in figure 4.1 on page. Each process has one or more subVIs (sub routines in text based programming) that are linked logically to give the required output.

The processes are given below:

(a) **Initialize Source Meter.**

This brings the source meter to default state by removing the previously set parameters so that other parameters can be set to suit the user's objectives. This process has only one subVI known as Keith2400 Initialize.vi.

(b) **Set Parameters**

This process sets the parameters to read from the source meter and measure the output. The important parameters to set here are to source current and measure voltage, source voltage and measure current or source and measure current and voltage concurrently. At this level settings are also made to have the meter measure a fixed point or sweep between the limits set. In this project a choice is made to have a sweep from voltage at open circuit to zero voltage while measuring the resulting current. This process has three subVIs namely Keith2400Voltconfig.vi, Keith2400DCI meas.vi and Keith2400Sweepconfig.vi

(c) **Output On**

This process switches the output on in readiness to perform the source-measure operations.

It has only one subVI known as Keith2400 OutpControl.vi.

The above processes are performed in a sequence and a sequence structure is used to carry out the processes.

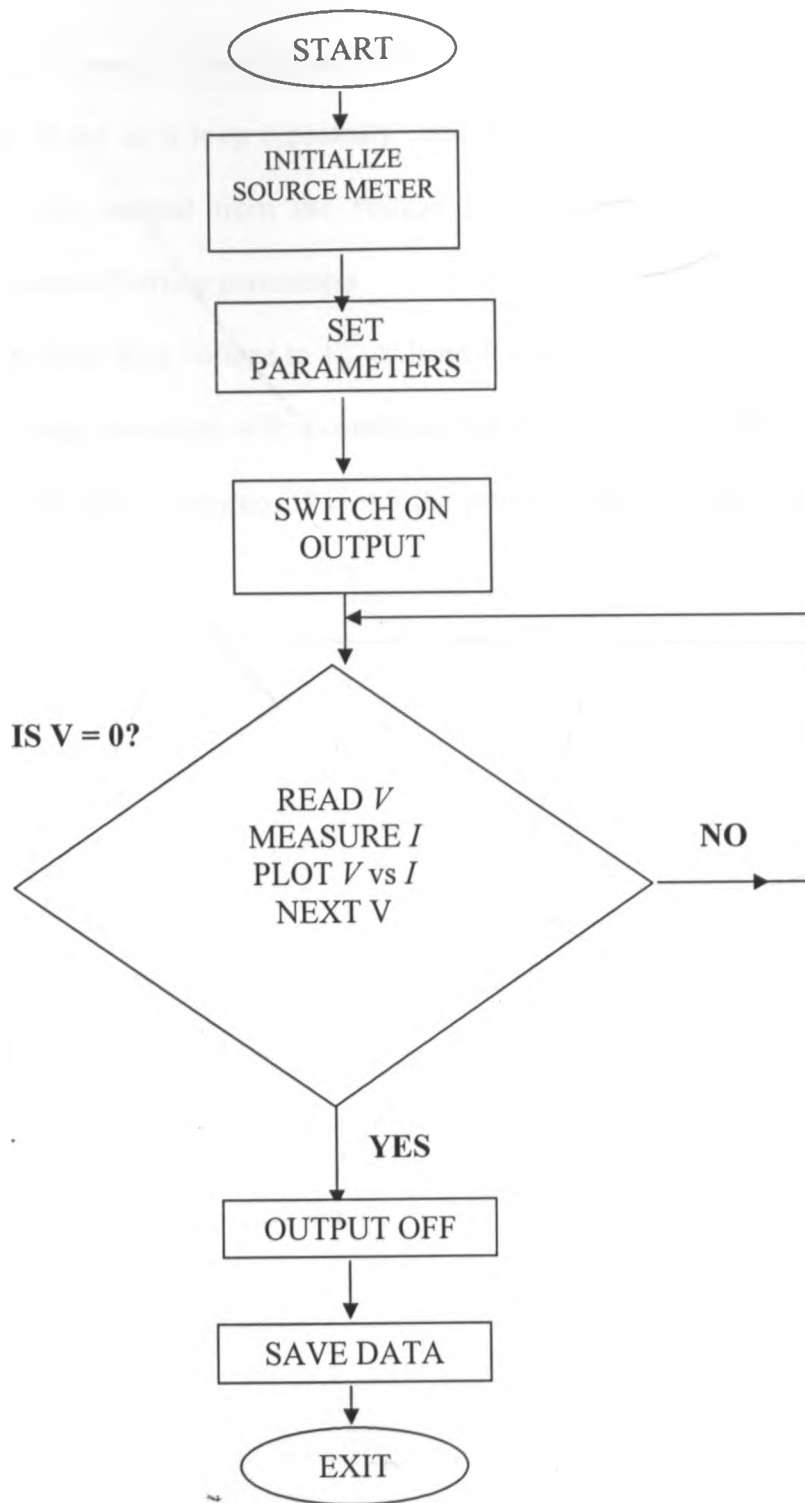


Figure A1: A flow chart showing the events of the processes of measuring and plotting the current voltage characteristics

(d) **Read Voltage, Measure Current and Plot graph**

This process is carried out in a loop repeatedly until a condition is satisfied. A voltage is sourced and the current excited from the voltage is measured. The sweep direction is determined in the process of setting parameters

Voltage can be swept from zero voltage to V_{oc} or from V_{oc} to zero voltage. A while loop has been used to execute these processes with a condition that while V is not equal to zero, perform the source, measure and plot processes. If $V = 0$ the program exits the loop, saves data and switches off output.

Appendix II

Automation of *IPCE* Characterization System

A2.0 Introduction

Revisiting the *IPCE* model equation earlier discussed in chapter 3, i.e.

$$IPCE(\%) = \frac{1240 J_{sc} (mAcm^{-2})}{\lambda (nm) P_{in} (mWcm^{-2})} \times 100\% \quad (A-1)$$

where J_{sc} is the short circuit photocurrent density (measured by a source meter),

λ is the wavelength (obtained from the lamp that is set at a particular wavelength by the monochromator)

P_{in} is the incident radiation at a particular wavelength (obtained by an optical power meter and a detector)

A plot of equation (4) gives a graph of *IPCE* (%) at different wavelengths (λ).

The setup consists of a light source, a monochromator, a photodiode connected to an optical meter and a current measurement system. To get the *IPCE*, first the incident power (P) is measured at each wavelength and stored as a calibration file. The solar cell is then put at the same position as the photodiode and current is measured at each wavelength. The calculation of *IPCE* is accomplished by recalling the calibration file every time a new wavelength is set. This process was automated using LabVIEW™ development application.

A2.1 Communication Protocol

- (a) Monochromator

The monochromator used here is Acton Research Corp. monochromator model SpectraPro-150. Communication with this device was established via serial port COM2. The commands for setting wavelength were processed through the dll (dynamic link library) function call.

(b) Optical power meter

The optical power meter reads the power of incident light at a particular wavelength set by the monochromator. The device is an Oriel Instruments OPM model 70310. Communication was via GPIB interface with address 5. The commands for reading out power from the instruments were established via instrument drivers located in LabVIEW.

(c) Current Measurement

Current was measured by use of Keithley 2400TM source meter whose interface is GPIB address 24. The commands for measuring current at the set wavelength are via instrument drivers which are inside LabVIEW.

A2.2 Algorithm for Automating *IPCE*

The following is a summary of steps to be followed in the LabVIEW program for obtaining *IPCE* automatically.

1. Obtain calibration data from optical power meter
2. Set the initial conditions (start and stop wavelengths)
3. Set wavelength required to the monochromator
4. Obtain current from the sample via Keithley source meter

5. Use the calibration data to incorporate in the *IPCE* formula for overall calculation
6. Plot *IPCE* vs λ at the suitable steps

A2.3 Flowchart

A flowchart to implement the above algorithm is shown in figure 4.2 below

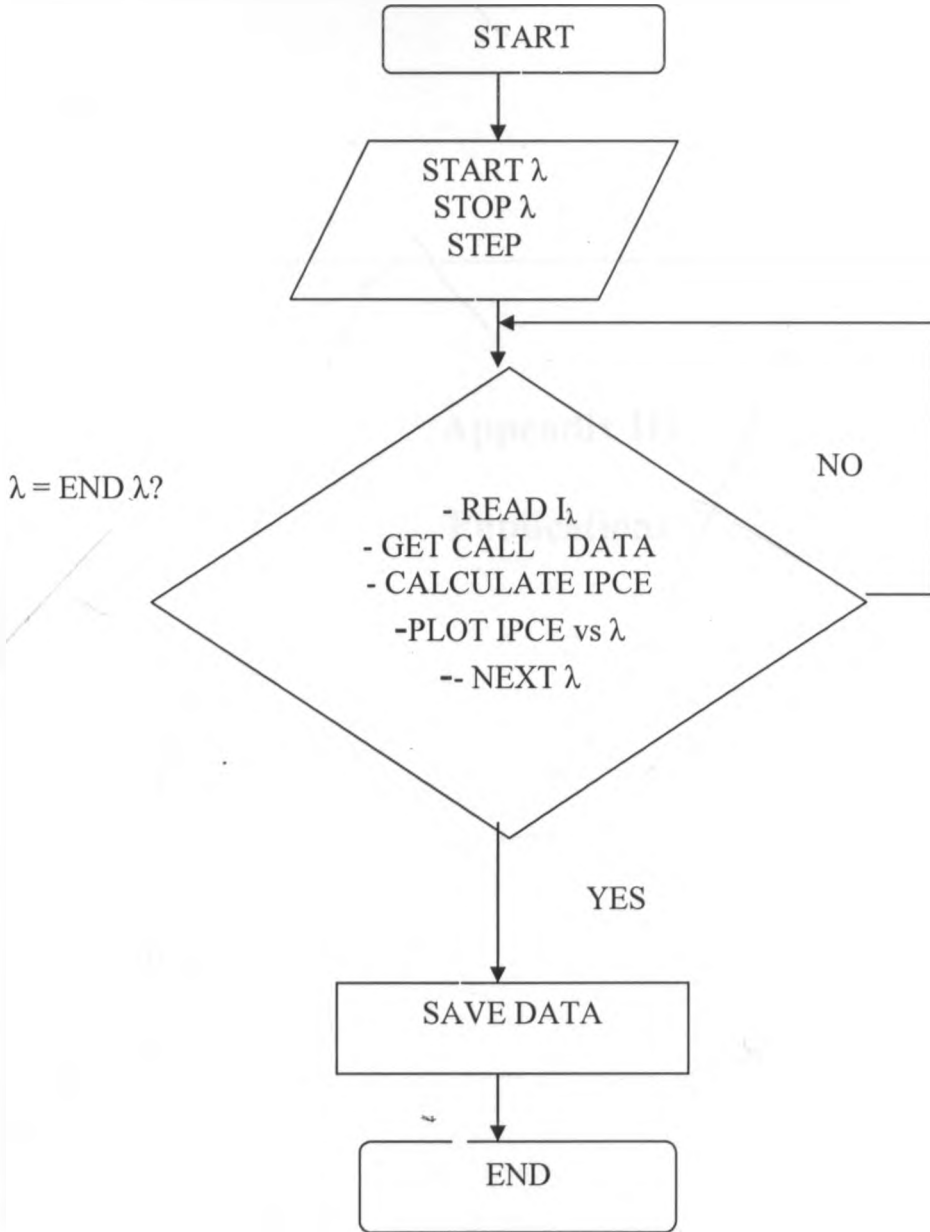


Figure A2: Flowchart for obtaining *IPCE* data from a solar cell.

Appendix III
Publications



Interpretation of small-modulation photocurrent transients in dye-sensitized solar cells – A film thickness study

Jarl Nissfolk^a, Kristofer Fredin^b, Justus Simiyu^c, Leif Häggman^c, Anders Hagfeldt^{a,c}, Gerrit Boschloo^{c,*}

^aCenter of Molecular Devices, Royal Institute of Technology, Chemical Science and Engineering, 10044 Stockholm, Sweden

^bDepartment of Physics and Materials Science, Uppsala University, Sweden

^cUppsala University, Dept. of Physical and Analytical Chemistry, Box 259, 751 05 Uppsala, Sweden

ARTICLE INFO

Article history:

Received 1 October 2009

Received in revised form 3 March 2010

Accepted 15 March 2010

Available online 18 March 2010

Keywords:

Electron transport

Mesoporous TiO₂

Diffusion

Trapping

ABSTRACT

Electron transport in dye-sensitized solar cells with varying mesoporous TiO₂ film thicknesses was investigated using experimental and computational methods. More specifically, photocurrent transients resulting from small-amplitude square-wave modulation of the incident light were recorded for a series of solar cells, whereby the dependence of the wavelength and direction of the illumination was investigated. The responses were compared to simulations using different models for diffusional charge transport and analyzed in detail. The photocurrent transients are composed of two components: an initial fast response in case of illumination from the working electrode side, or an initial apparent delay of photocurrent decay for illumination from the counter electrode side, followed by a single exponential decay at longer times, with a time constant that is identified as the electron transport time. The initial response depends on the thickness and the absorption coefficient of the film. Transport times for different films were compared at equal short-circuit current density, rather than at equal light intensity. Experimentally, the transport time showed a power-law dependence on the film thickness with an exponent of about 1.5. Analysis using the quasi-static multiple trapping (MT) formulation demonstrates that this behavior originates from differences in quasi-Fermi level in the TiO₂ films of different thickness when equal photocurrents are generated. The Fokker–Planck relation was used to derive expressions for the electrons flux in porous TiO₂ films with a position-dependent diffusion coefficient.

© 2010 Elsevier B.V. All rights reserved.

1. Introduction

Dye-sensitized solar cells (DSCs) have attained significant attention during the last years because of their potential to become a low-cost alternative to conventional solar cells. DSCs with an overall power conversion efficiency exceeding 10% have been reported [1–5]. Although the overall function of the device has been fairly well described [6–8], in-depth understanding of several processes is lacking. One of these, which is of central importance for efficiency, is that of electron transport in the electrolyte-impregnated mesoporous TiO₂ film. It has been proposed by several groups that this electron transport is driven by diffusion [9,10]. Experimental measurements as well as computer simulations have displayed that the electron diffusion coefficient is related to the structure of the mesoporous film [11] as well as the “necking” of neighboring nanoparticles [12,13]. Furthermore, it has been found that the electron diffusion coefficient is related to the composition of the electrolyte, via an ambipolar diffusion mechanism [14]. Fi-

nally, the diffusion coefficient depends strongly on incident light intensity, as first reported by Cao et al. [15].

A number of experimental methods have been used to study the electron transport processes in mesoporous TiO₂ films. Small-amplitude modulation methods such as intensity-modulated photocurrent spectroscopy (IMPS) [16–18] and transient photocurrent measurements [14,19] yield a transport time related to the electron diffusion coefficient. The transport time has been investigated as function of applied potential [20]. Charge transport measurements have also been conducted at open-circuit conditions using a transient voltage rise method [21]. Electrical impedance spectroscopy (EIS) has been used to measure charge transport in mesoporous TiO₂ electrodes, as well as complete DSCs [22,23]. DC conductivity measurements of mesoporous TiO₂ electrodes have been performed in redox inactive electrolytes [24], while conductivity measurements using microwave absorption [25] and terahertz spectroscopy [26] have been performed on mesoporous titanium dioxide systems in absence of electrolyte.

Experimental results have demonstrated that the measured (effective) diffusion coefficient is closely related to the total density of electrons and the quasi-Fermi level in the mesoporous TiO₂ [22,23]. This agrees well with the observations that the measured

*Corresponding author. Tel.: +46 18 4713303.

E-mail address: gerrit.boschloo@fki.uu.se (G. Boschloo).

electron diffusion coefficient increases with light intensity in DSCs under short-circuit conditions, as the quasi-Fermi level in the porous TiO_2 is raised by the increased flux of photogenerated electrons. The electron transport and accumulation properties in mesoporous TiO_2 have been explained using a multiple trapping model, in which only a minor fraction of the electrons are being transported in the conduction band, while most electrons are trapped in localized states below the band edge [27,28]. The trap distribution can be related to the chemical capacitance of a nanostructured semiconductor [29]. Computer simulations have verified that the kinetics of the multiple trapping (MT) model lead to an anomalous electron transport process in accordance with experimental results [30,31]. Bisquert and Vihrenko demonstrated that, when the kinetics of the trapping/detrapping process is faster than the time constant of the electron transport, a quasi-steady state condition arises and that a chemical (effective) diffusion coefficient can be defined that depends on the Fermi level [29]. Although the MT model has gained acceptance within the scientific community, it still lacks definite experimental proof. It has been demonstrated, using a theoretical model, that similar transport characteristics can also be obtained when charge carriers are hopping between localized energy states [32]. Recently, an overview of models that describe electron transport in semiconductors with a broad distribution of states was presented by Bisquert [33]. Here, we will present results on transport time measurements using a photocurrent transient method. The transient photocurrent response to a small square-wave modulation of light intensity is recorded. It is demonstrated how the photocurrent response is influenced by film thickness, illumination wavelength and illumination direction (from working electrode or counter electrode side). The relationship between electron transport time and mesoporous TiO_2 film thickness was found to be more linear than expected. The transport time would depend on the square of the thickness if the transport is described by a constant diffusion coefficient. The experimental results are compared with three models using the diffusion model and the quasi-static approximation of the MT model in the absence of recombination. We note that Halme et al. recently studied similar issues using the IMPs technique [34].

Experimental

Solar cell preparation

TiO_2 paste was prepared as described elsewhere [35]. Working electrodes were prepared onto fluorine-doped tin oxide coated glass (FTO) using the screen printing technique, yielding film thicknesses between 4 and 26 μm . The area of the TiO_2 films was 0.48 cm^2 . The electrodes were immersed in a dye bath containing N719 in ethanol overnight for sensitization. Counter electrodes were created by spreading 5 mM H_2PtCl_6 in isopropanol on the FTO substrates (10 $\mu\text{l}/\text{cm}^2$), followed by heating to 100 $^\circ\text{C}$. The DSCs were thereafter assembled by sealing the working and counter electrodes with surlin 1702 (~50 μm thickness) and introducing the electrolyte via pre-drilled holes in the counter electrode. The electrolyte was composed of 100 mM I_2 , 100 mM LiI, 0.1 M tetrabutylammonium iodide and 500 mM 4-tert-butylpyridine, dissolved in 3-methoxypropionitrile.

Characterization methods

Electron transport measurements were performed by recording the photocurrent response to a small square-wave modulation of the light intensity [17,30]. Light emitting diodes (Luxeon Star 1 W) were used as the light source, giving red

(640 nm) and green (530 nm) light with intensities ranging from 0.2 to 32.5 mW cm^{-2} and 0.2 to 73.9 mW cm^{-2} for red and green light respectively. The RC-time constants of the solar cell

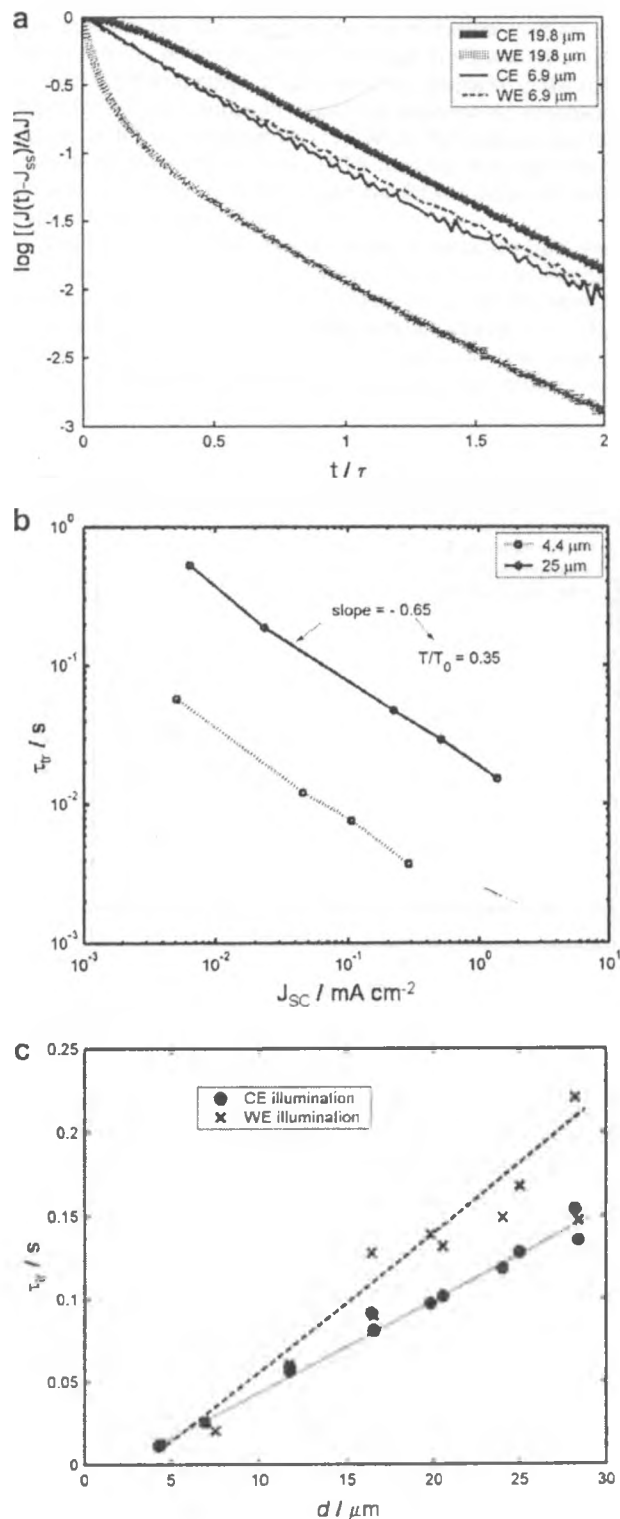


Fig. 1. (a) Normalized data of small-amplitude photocurrent decay transients of mesoporous dye-sensitized solar cells with two film thicknesses, illuminated from working electrode (WE) or counter electrode (CE) side. (b) Electron transport time for two film thickness as function of the short-circuit current density. (c) Transport time for a range of film thicknesses compared at $J_{sc} = 0.5 \text{ mA cm}^{-2}$, for WE and CE illumination.

were in the order of 0.1 ms and were neglected in the analysis of the photocurrent transients.

3.1. Simulations

Model calculations were performed using a finite element analysis solver and simulation program (Femlab multiphysics 3.2 by COMSOL) on a laptop with Intel Pentium 1.7 GHz processor and 4 Gb RAM. Simulation times ranged from 1 to 30 min.

Results and discussion

3.1. Experimental results

The influence of the carrier generation profile on the current transient during an electron transport experiment was studied by varying the TiO₂ film thickness, photon wavelength and illumination direction. In Fig. 1a, current transients are shown for two DSCs with film thicknesses of 6.9 and 19.8 μm, respectively, for green light illumination incident from either the working electrode side (SE illumination) or the counter electrode side (electrolyte–electrode (EE) illumination). As the normalized photocurrents are plotted on a logarithmic scale versus time it is clearly seen that the photocurrent decays as a single exponential on longer timescales. In absence of significant recombination losses, the decay time constant equals the transport time, as will be shown later. On a shorter timescale, the current decay deviates from single exponential behavior. This deviation is most pronounced for the thicker film for SE illumination (see Fig. 1a). Initially, the photocurrent decays faster, whereas for EE illumination the current remains constant for some time before it starts to decay. For the thinner TiO₂ film, no discernable difference between SE and EE illumination can be observed. Repeating the measurements with a red LED as light source gives similar photocurrent transients, however the initial deviations are less pronounced. This is due to the lower absorption coefficient of the N719-sensitized TiO₂ film for red light, leading to more uniform electron generation in the film, as will be discussed more in detail in Section 3.2.1.

Current transient measurements were performed for a range of light intensities. The transport time, τ_{tr} , was extracted from the rate constant of the single exponential decay. It shows a power-law dependence on the light intensity and the short-circuit current density, as illustrated in Fig. 1b for two film thicknesses. A power-law exponent of about -0.65 is determined from the slope. Expectedly, transport times are longer for thicker TiO₂ films.

In comparison of the transport times for DSCs with different film thickness was done under conditions of equal short-circuit photocurrent density. For diffusion driven transport, this approach implies similar gradients of the electron concentration profiles close to the contact. It was therefore chosen over the light intensity parameter for comparison. For a short-circuit current density of 0.5 mA cm^{-2} , the transport times are shown as function of film thickness, d , in Fig. 1c for SE and EE illumination. The relation between τ_{tr} and d is surprisingly linear. For electron transport driven by diffusion one would expect the transport time τ_{tr} to vary with the square of the film thickness [36]. Instead, the data in Fig. 1c was best fitted with a power-law relation, $\tau_{tr} \propto d^\omega$, with a constant ω of 1.55 for EE and 1.32 for SE illumination.

In this section we will compare the presented results with predictions from theoretical electron transport models based on pure diffusion (model 1) and multiple trapping with the quasi-static approximation (models 2 and 3, respectively). Effects of recombination will not be discussed here, but will be briefly addressed in the supporting information.

3.2. Computational results and discussion

3.2.1. Pure diffusion (model 1)

The simplest available electron transport model is that of diffusion of electrons with a constant diffusion coefficient in an effective medium [9]. This implies that the diffusion coefficient, D , is not dependent on the concentration of electrons and effects related to trapping/detrapping. The photocurrent response in the time domain for the pure diffusion model has been solved analytically by Cao et al. for SE illumination [15], while the solution for the frequency-resolved analogue, i.e., IMPS, has been first reported by Peter and co-workers [16]. The equations for the diffusion model are summarized in Appendix A.

During the electron transport measurements, the light intensity is increased and decreased by a step function ΔI_0 , giving rise to a photocurrent transient with amplitude Δj . In the experiment the DSC switches between two steady state situations; the difference in concentration of charge carriers between the two situations is ΔQ . As we describe transport diffusion, we only need to consider

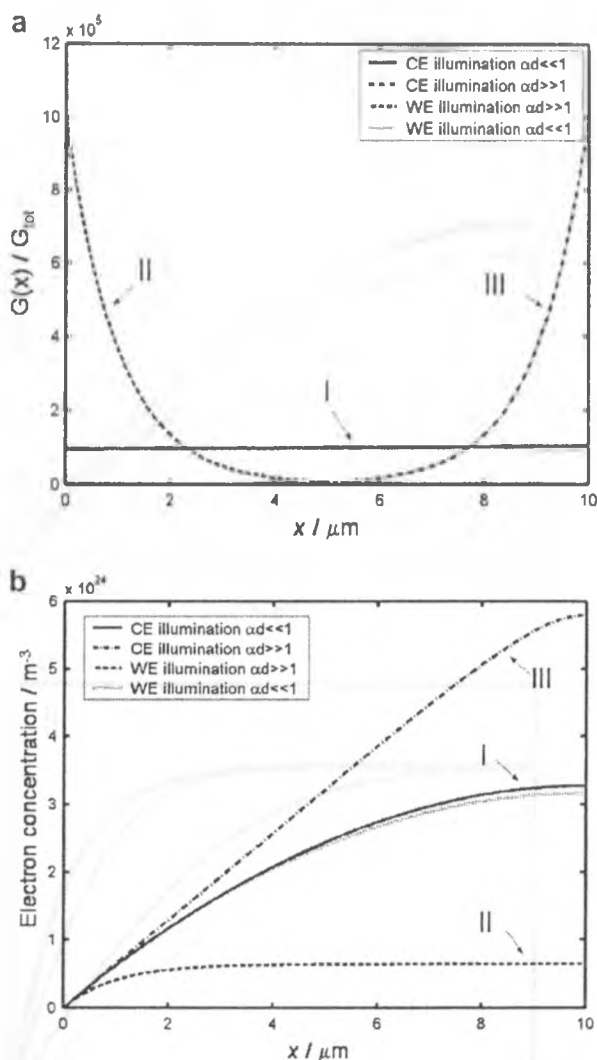


Fig. 2. (a) Generation profile of electrons $G(x)$ at a distance x in the mesoporous TiO₂ film from the conducting substrate, normalized by the total amount of generated charge carriers. (b) The steady state electron concentration profiles in the mesoporous TiO₂ at the same short-circuit current density (10 mA cm^{-2}) for pure diffusion (model 1; $D = 10^{-5} \text{ cm}^2 \text{ s}^{-1}$) for the cases I ($\alpha d = 0.01$), II ($\alpha d = 10$) and III ($\alpha d = 10$).

to simulate the photocurrent decay from which the transport constant can be derived.

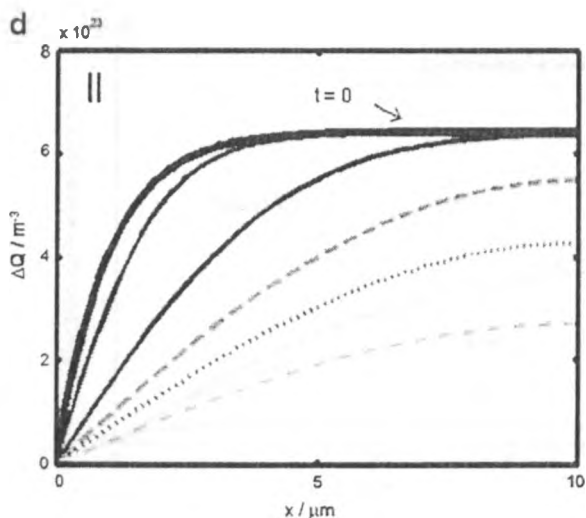
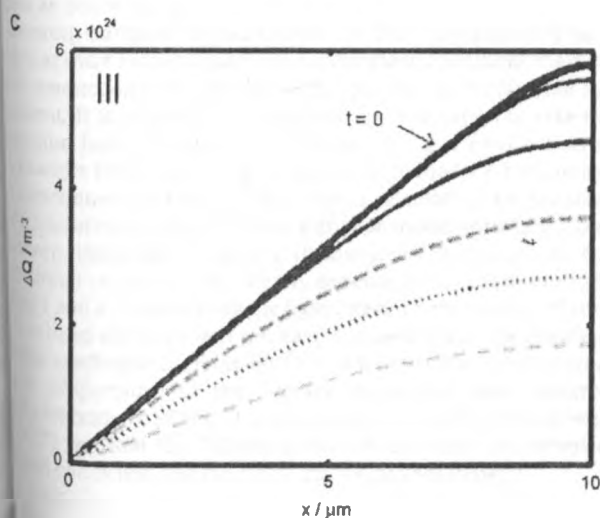
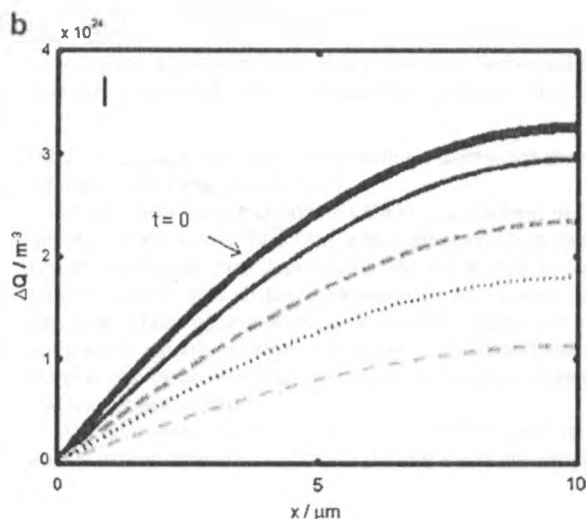
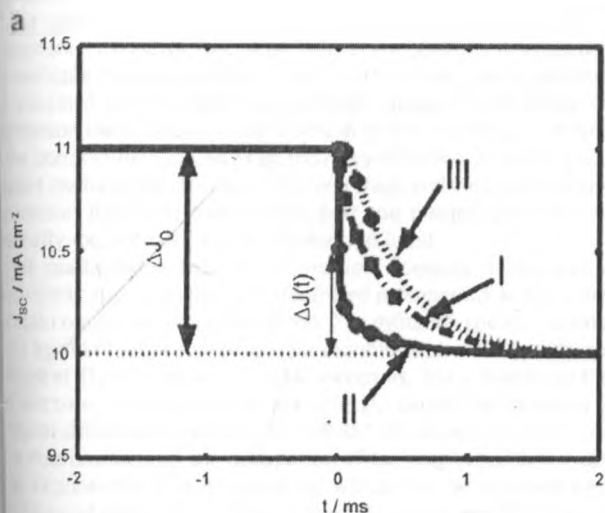
Three generation profiles are considered:

- I. Constant charge carrier generation throughout the film, i.e., the absorption coefficient α is low in comparison to the film thickness d : $\alpha d \ll 1$. The generation profile is then independent on illumination direction.
- II. Generation of charge carriers in a narrow region close to the SE interface. This occurs for SE illumination when $\alpha d \gg 1$.
- III. Generation of charge carriers in a narrow region close to the EE interface. This occurs when $\alpha d \gg 1$ for EE illumination.

The generation profiles and the resulting simulation results for steady state charge density profiles are depicted in Figs. 2a–b. Marked differences between the charge density profiles to be observed. Although the slopes at the SE interface ($x=0$) are equal, the charge density is largest for condition III, smaller for II, and least for I. The photocurrent transients as well as the development of the charge density profiles in time are shown in Fig. 3. Analysis of these profiles can explain the behavior of the current transients. For condition I, which represents that of homogeneous generation of electrons, the charge profile decays homogeneously, i.e., the normalized shape appears not to change.

The current transient follows a single exponential decay. For condition III, corresponding most closely to the experimental results for the thick film ($d = 19.8 \mu\text{m}$) for EE illumination, an apparent delay in the current response is found (compare Fig. 5a, where the normalized transient are shown with Fig. 1a). Noting that the charge density $n(x)$ increases linearly with distance x in the film under steady state conditions (see condition III in Fig. 2b) and following the development of the charge profile with time (Fig. 3c) this can be explained as follows: Because the electron flux is roughly constant in the device due to the diffusion relation $J = -D(dn/dx)$, application of the downward step in light intensity causes the charge density first to be lowered in the EE region. On short time scales, the charge concentration gradient near the FTO contact is maintained, see Fig. 3d. This causes the current to be initially constant before decay sets in. In contrast, for SE illumination (condition II), $n(x)$ is almost constant for x -values exceeding $2 \mu\text{m}$, see Fig. 2b. This implies that electrons extracted at the SE interface will not be fully replaced as for condition III and as a consequence, the slope $(dn/dx)_{x=0}$ will decrease rapidly, leading to a fast reduction in J . The charge density profile in cases II and III become more similar to that of case I in time and eventually single exponential decay is found in all cases.

It is noted that the simple diffusion model predicts the shape of photocurrent transients very well, which puts the previously sug-



The photocurrent transient using the pure diffusion model (model 1), starting at the same steady state conditions for three cases I, II and III as given in Fig. 2b. (b–d) Charge density profiles in the film evolving with time during the photocurrent transient for the three cases.

gested effect of non-thermalized electron transport in case of SE illumination in question [30].

At longer times the photocurrent decay is described by Eq. (1), independent on the illumination level and direction and absorption coefficient:

$$j(t) = J_{sc} + \Delta j \cdot e^{-t/\tau_{tr}} \quad (1a)$$

$$\tau_{tr} = \frac{d^2}{2.47D} \quad (1b)$$

where J is the photocurrent density, and J_{sc} the constant bias level of j . Similar expressions have been derived by others groups, although slight differences in the factor 2.47 are reported, i.e. 2.35 [30] and 2.77 [37]. In our analysis we use an infinite lifetime of the electrons, making the approximation valid when the lifetime at short-circuit condition is much longer than the transport time.

The transport time for the pure diffusion model is only related to the thickness and the diffusion coefficient. The transport time will not change with different intensities of bias light, which is in contradiction with the experimental results (see, e.g., Fig. 1b). In the following section trapping/detrapping of charge carriers is included in the model to account for this effect.

2.2. Quasi-static multiple trapping model with distance-independent chemical diffusion coefficient (model 2)

The light intensity dependence of the electron transport time in mesoporous dye-sensitized solar cells is successfully described by the multiple trapping model [27,28]. In this model, most electrons are assumed to be trapped in localized energy states below the conduction band. Only a small fraction of the electrons is present in the conduction band and can move by diffusion. There is a continuous exchange of electrons between traps and conduction band: conduction band electrons get trapped and trapped electrons are thermally excited back to the conduction band.

The mathematics behind the multiple trapping model and its quasi-static approximation are described in Appendix B. Here, only the main outcomes are summarized: The diffusion coefficient measured by small-amplitude transient techniques is not the diffusion coefficient D_0 of conduction band electrons, but a much smaller electron concentration dependent D_n , called the apparent or chemical diffusion coefficient [27,29,38]. D_n depends on the trap state distribution and the occupation of the trap sites. In the case of an exponential trap distribution, which will be assumed here, the chemical diffusion coefficient depends on the electron concentration as described by Eq. (A17).

Electron transport measurements in DSCs are normally performed at short-circuit conditions. Under these conditions the density of conduction band electrons is not constant in the film, but has a gradient. It is, however, a reasonable approximation to take the conduction band electron concentration (n_c) as a constant, as n_c only changes strongly close to the substrate. In model 2, the average n_c is determined from the n_c profile that is calculated from the steady-state solution by using the pure diffusion model with D_0 at a certain short-circuit current density. In absence of recombination, the short-circuit current will be linearly dependent on light intensity in models 1 and 2. By increasing the light intensity, the number of conduction band electrons will increase and hence also the chemical diffusion coefficient D_n . From Eq. (A5), it follows that the photocurrent is proportional to the average conduction band electron density for both for SE and EE illumination. Using this relation with Eq. (A17), we find the following relation between the chemical diffusion coefficient and the short-circuit current density:

$$D_n \propto j_{sc}^{1-T/T_0} \quad (2a)$$

$$D_n \propto j_{sc}^{1-T/T_0-1} \quad (2b)$$

Relation (2b), derived using the relationship between τ_{tr} and a constant diffusion coefficient (Eq. (1b)), explains the power-law dependence of the transport time with short-circuit current. The value of T/T_0 is easily determined from experimental data: from the slope in Fig. 1b T/T_0 is found to be 0.35 in the investigated DSCs.

The relation between transport time and film thickness was investigated using model 2. Fig. 4 shows how the conduction band electron density depends on film thickness, when the short-circuit current is held constant. There is a difference in the charge density profiles when changing the film thickness for the three illumination conditions. In case II (strong light absorption near the FTO contact), the average density of conduction band electrons remains almost constant when the thickness is changed, as n_c is constant in the film except for a very narrow region near the SE interface. Consequently, the chemical diffusion coefficient remains constant and transport times scale with the square of the film thickness. For cases I and III, the average conduction band electron concentration scales linearly with film thickness. The measured transport time will depend both on the thickness and on the average charge density. The relation between τ_{tr} and d obtained from simulations with model 2 is:

$$\tau_{tr} \propto d^\omega, \text{ with } \omega = 2 \text{ for case II and } \omega = 1 + T/T_0 \text{ for cases I and III} \quad (3)$$

The photocurrent response will in all cases (I, II and III) have the same response as for pure diffusion (model 1), when rescaling the time by the transport time. This is because both models assume that diffusion coefficient is independent on the position in the film.

3.2.3. Quasi-static MT model with distance dependent chemical diffusion coefficient (model 3)

Under short-circuit conditions there is a gradient in the charge density in the porous TiO₂ film, which gives rise to a chemical diffusion coefficient that depends on the position x in the film. In model 3, takes this distance dependence of D_n into account. In the quasi-static approximation of the MT model, the continuity equation is usually written in terms of conduction band electrons. Here, it will be shown that it may also be written in terms of total electron concentration.

A fundamental condition in Fick's first law (used in models 1 and 2) is that diffusion coefficient is constant in the whole system.

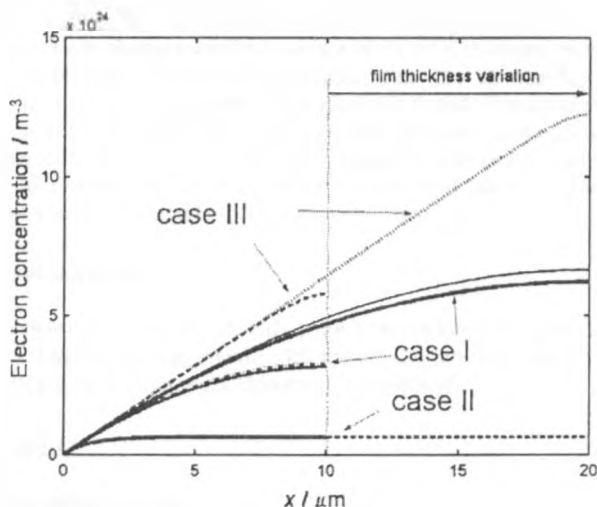


Fig. 4. The charge density profiles for conduction band electrons at constant short-circuit density, calculated for two film thicknesses using model 2 for cases I, II and III.

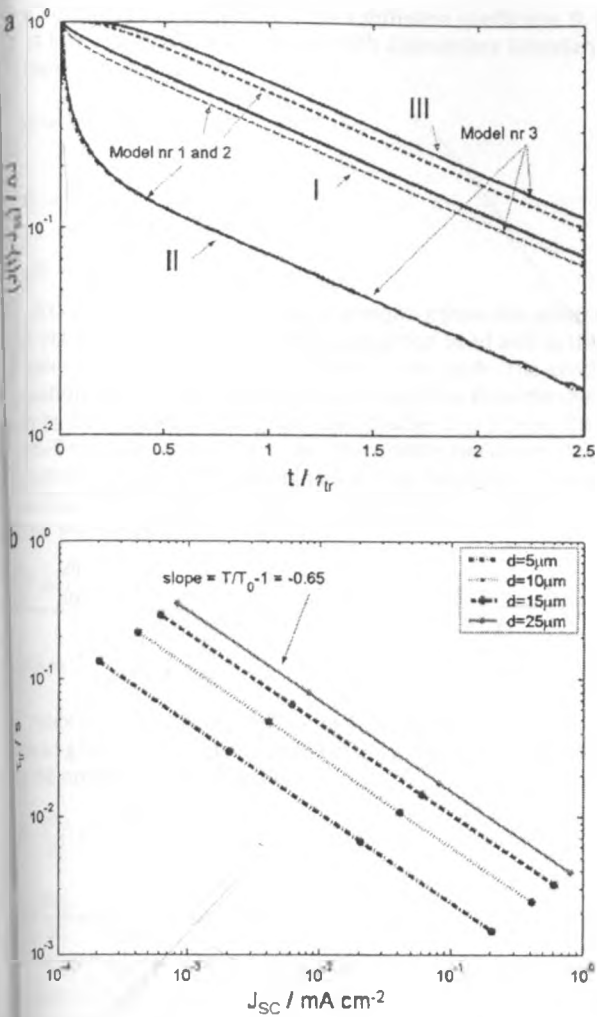


Fig. 5. (a) Simulated photocurrent decay transients using models 1, 2 and 3. For models 1 and 2, the diffusion coefficient is not position-dependent. For model 3, the factor $T/T_0 = 0.35$ has been used. The three cases I, II and III are shown for the three cases used, α values were 10^3 and 10^6 m^{-1} and d was 10^{-5} m . (b) Simulated transport time measurements using model 3, performed for a range of film thicknesses and light intensities ($T/T_0 = 0.35$).

The first law does therefore not hold in systems where the diffusion coefficient varies with position x in the film. In such systems it is appropriate to use the Fokker–Planck diffusivity law instead

$$J = -\frac{d}{dx} [D(x)n(x, t)] \quad (4)$$

In model 3, the quasi-static approximation of the multiple trap model is used, and it is assumed that the total electron concentration is equal to the concentration of trapped electrons, i.e. $n + n_t \approx n_t$. Using the Fokker–Planck equation the following expression is derived, see Appendix C for details:

$$-\frac{T_0}{T} D_j(x) \frac{dn(x)}{dx} \quad (5)$$

$D_j(x)$ is a position-dependent jump diffusion coefficient. Note that the flux of trapped electrons is considered, which is fundamentally different from the flux of conduction band electrons in model 1. The continuity equation for either trapped electrons or conduction band electrons yields the same response for the quasi-static approximation. The description using the Fokker–Planck equation

is a more general description that can also be applied to alternative electron transport models, such as the transport by hopping [32].

Simulations of model 3 were performed by numerically solving the nonlinear partial differential equations with boundary conditions $J(x=d) = 0$ and $n(x=0) = n_0$. The simulation was performed for the three cases I, II and III described earlier, using the factor $T/T_0 = 0.35$, which was obtained from experimental results. The photocurrent response for model 3 is very similar to the simulations obtained with models 1 and 2, see Fig. 5a. There are, however, small differences depending on α and d . Only in case II (charge generation near SE interface) all models overlap perfectly. A series of transport measurements were simulated with model 3 with a range of film thicknesses and light intensities and absorption coefficients, see Fig. 5b. Transport times were calculated from the single exponential photocurrent decay after the initial transient. The transport time versus film thickness gave the same power-law relation, Eq. (4), as for model 2.

In cases I and III, there is an electron concentration gradient in a larger part of the film. Near the EE interface the film has a higher diffusion coefficient than near the SE interface where charge density is lower. An estimation of the transport time from the average concentration of electrons, as is done in model 2, gives slightly longer transport times than the ones calculated with model 3 for cases I and III.

In the simulations electron recombination was not taken into account. In the supporting information a simple approach to include recombination, using a constant diffusion length, is described

4. Conclusions

The photocurrent transients of dye-sensitized solar cells, upon small stepwise changes in light intensity, are well modeled using a simple diffusion model, where the diffusion coefficient depends on the average conduction band electron concentration in the mesoporous TiO_2 film. For uniform light absorption and electron generation in the film a single exponential decay (rise) is found, with a time constant that corresponds, in absence of recombination, to the transport time. For non-uniform light absorption, initially a faster decay is observed in case of SE illumination, experimentally as well as in simulations, converging to single exponential at longer time scales. An apparent delay for the single exponential decay is found in case of EE illumination. It has been demonstrated that, under conditions of constant photocurrent density, the electron transport time changes with the square of the film thickness only under conditions of electron generation near the SE interface, while in other cases a weaker dependence is found. Simulations, where a diffusion coefficient was used that depends on the local electron concentration, showed only marginal differences compared to simulations using a diffusion coefficient based on the average conduction band electron concentration.

Acknowledgement

This work has been supported by the Swedish Research Council and the Swedish Energy Agency. J.S. thanks the International Science Programme at Uppsala University for support.

Appendix A

A.1. Pure diffusion model

In this model, transport of electrons in mesoporous TiO_2 is described by diffusion using a fixed diffusion coefficient. All electrons

are considered to be mobile with a diffusion coefficient D . Fick's first law can therefore be applied with appropriate boundary conditions. Eqs. A1(a)–A1(c).

$$j(x) = -D \frac{dn_c(x)}{dx} \tag{A1a}$$

$$j(d) = \left. \frac{dn_c(x)}{dx} \right|_{x=d} = 0 \tag{A1b}$$

$$n_c(0) = n_0 \tag{A1c}$$

$j(x)$ denotes the electron flux at position x from the substrate, n_c the electron concentration in the conduction band and n_0 the conduction band electron concentration in the dark. The continuity equation with a source term for charge injection from the dye is given by Eq. (A2), where the generation profile, $G(x)$ follows the Lambert–Beer law and differs for electrolyte–electrode (EE) and substrate–electrode (SE) illumination. I_0 is the photon flux of incident monochromatic light and α is the absorption coefficient at the same wavelength.

$$\frac{\partial n_c}{\partial t} = \frac{\partial j}{\partial x} + G(x) \tag{A2}$$

$$G(x) = \begin{cases} I_0 e^{-\alpha x} & \text{SE} \\ I_0 e^{-\alpha(x-d)} & \text{EE} \end{cases} \tag{A3}$$

Note that this model does not include the recombination, which would give an additional term in Eq. (A2). The continuity equations for SE and EE illumination are:

$$\frac{\partial n_c}{\partial t} = D \frac{\partial^2 n_c}{\partial x^2} + \alpha I_0 e^{-\alpha x} \tag{A4a}$$

$$\frac{\partial n_c}{\partial t} = D \frac{\partial^2 n_c}{\partial x^2} + \alpha I_0 e^{-\alpha(d-x)} \tag{A4b}$$

These result in steady state solutions for given in Eq. (A5). J_{SC} is short-circuit electron flux, equal to $I_0(1 - e^{-\alpha d})$.

$$n_c(x) = \frac{J_{SC}}{\alpha D} \frac{(1 - \alpha x e^{-\alpha d} - e^{-\alpha x})}{(1 - e^{-\alpha d})} \tag{A5a}$$

$$n_c(x) = -\frac{J_{SC}}{\alpha D} \frac{(e^{-\alpha(d-x)} - \alpha x - e^{-\alpha d})}{(1 - e^{-\alpha d})} \tag{A5b}$$

Appendix B

Multiple trapping model and quasi state approximation

In this model, traps with energies below the conduction band are added. Electron transport takes place in the conduction band diffusion. During transport electrons will undergo numerous trapping and detrapping events. Detrapping is a thermally activated process. Experimental results suggest that there is an exponential distribution of traps $g(E)$ below the conduction band edge that can be described by:

$$g(E) = \frac{N_T}{k_B T_0} \exp[(E - E_c)/k_B T_0] \tag{A6}$$

where N_T is the total density of localized states and T_0 is a parameter related to the average depth of the distribution. The charge density of electrons in the trapped states n_t is calculated by integrating the band gap states for a certain Fermi level E_F (Eq. (A7)). Fermi–Dirac statistics (Eq. (A8)) are used to calculate the occupancy of energy levels.

$$n_t = \int_{E_c}^{E_t} g(E) f_t(E) \tag{A7}$$

$$f_t(E) = \frac{1}{1 + e^{(E-E_F)/k_B T}} \tag{A8}$$

The density of conduction band electrons is given by the Boltzmann approximation:

$$n_c = N_c \exp[(E_F - E_c)/k_B T] \tag{A9}$$

It is assumed that electrons are not interacting and each energy level can be occupied by one electron. The resulting relation between trapped non-mobile electrons and mobile electrons in the conduction band is then

$$n_t = N_t \exp[(E_F - E_c)/k_B T_0] = \frac{N_t}{N_c^{T/T_0}} n_c^{T/T_0} \tag{A10a}$$

$$n_c = \frac{N_c}{N_t^{T_0/T}} n_t^{T_0/T} \tag{A10b}$$

The trapping model assumes that there is one single diffusion coefficient for the conduction band of electrons in the film, D_0 , which is independent of light intensity. The trapping/detrapping to and from the conduction band adds an additional factor to the continuity equation for diffusion:

$$\frac{\partial n_c}{\partial t} = -\frac{\partial j}{\partial x} + G(x) - \frac{\partial n_t}{\partial t} \tag{A11}$$

where $\frac{\partial n_t}{\partial t}$ is the rate of change in concentration of trapped electrons per unit time, which is the sum of the trapping and detrapping kinetics described by Bisquert and Vikhrenko [29]. Under steady state illumination, the rates for trapping and detrapping are the equal and the number of conduction band electrons and trapped electrons are constant with time, so that $\frac{\partial n_t}{\partial t} = \frac{\partial n_c}{\partial t} = 0$. The concentration of conduction band electrons in the multiple trapping model is equal to that of the pure diffusion model when the same diffusion coefficient for the conduction band electrons, D_0 , is used. When small modulations of light intensity are applied, both the number of conduction band electrons and trapped electrons change with time. The terms $\frac{\partial n_t}{\partial t}$ and $\frac{\partial n_c}{\partial t}$ are then non-zero and electrons are being trapped and detrapped during the modulation. The kinetics involved in equilibrating the electrons in the conduction band and the trap states is a fast process. When this time is much faster than the measured quantity, in this case transport time for a small modulation of light, effects coming from equilibration may be neglected, which is the quasi-static approximation [29]. When charge carriers in the traps and conduction band are in thermal equilibrium during the transition for the modulation, there is a relation between the rate of change in number of mobile charge carriers and non-mobile charge carriers [29]:

$$\frac{\partial n_t}{\partial t} = \frac{\partial n_t}{\partial n_c} \frac{\partial n_c}{\partial t} \tag{A12}$$

This is the so-called quasi-static condition. Eq. (A12) shows that the change of trapped electrons per unit time is directly related to the rate of change of the conduction band electrons at quasi equilibrium, being the case for fast trapping/detrapping kinetics. For the quasi-static and steady state situations the relation between charges in the traps and conduction band is given by Eq. (A10b). The number of trapped electrons is considered to be much higher than the conduction band electrons, i.e. $n_c \ll n_t$. Therefore we can write the total number of electrons as trapped electrons $n_{tot} = n_c + n_t \approx n_t$. Using the quasi-static condition from A12 in Eq. (A11) will form Eq. (A13)

$$+ \frac{\partial n_t}{\partial n_c} \frac{\partial n_c}{\partial t} = - \frac{\partial J}{\partial x} + G(x) \quad (A13)$$

For $\frac{\partial n_c}{\partial t} \gg 1$ this equation can be re-written:

$$= - \frac{\partial n_c}{\partial n_t} \frac{\partial J}{\partial x} + \frac{\partial n_c}{\partial n_t} G(x) \quad (A14a)$$

$$= -D_0 \frac{\partial n_c}{\partial n_t} \frac{\partial^2 n_c}{\partial x^2} + \frac{\partial n_c}{\partial n_t} G(x) \quad (A14b)$$

We note that the generation term of the total amount of electrons is different from the generation term of conduction band electrons $\frac{\partial n_c}{\partial n_t} G(x)$. The effective diffusion coefficient differs from D_0 . From Eq. (A10b) one can derive that:

$$= \frac{N_c^{T/T_0} T_0}{N_T T} n_c^{1-T/T_0} = \frac{N_c T_0}{N_T T} \exp \left[(E - E_c) \left(\frac{1}{k_b T} - \frac{1}{k_b T_0} \right) \right] \quad (A15)$$

The apparent electron diffusion coefficient measured by small-amplitude transient measurements methods is related to D_0 as follows [29]:

$$= \frac{\partial n_c}{\partial n_t} D_0 = \frac{N_c T_0}{N_T T} \exp \left[(E - E_c) \left(\frac{1}{k_b T} - \frac{1}{k_b T_0} \right) \right] D_0 \quad (A16)$$

$$\frac{T_0 N_c^{T/T_0}}{T N_T} n_c^{1-T/T_0} D_0 \quad (A17)$$

Index C

Diffusion in inhomogeneous systems described by Fokker–Planck equation

The transport of charge carriers can in very general terms be described by kinetic or “jump” diffusion. The movement of carriers takes place by random jumps between positions with spacing a and a certain frequency $\Gamma(n)$ that depends on the local carrier concentration. The jump diffusion coefficient D_j is given by:

$$\frac{1}{6} \Gamma(n) a^2 \quad (A18)$$

We start by describing the movement between 3 positions in terms 1, 2 and 3 with distance, a , between each position, see Fig. A1. The flux of charge carriers from position 3, with a concentration n_3 to position 2 is $J_{3-2} = n_3 \times \Gamma(n_3)$ and from position 1 to 2 $J_{1-2} = n_1 \times \Gamma(n_1)$. The flux away from position 2 to the positions 1 and 3 will cancel each other, $J_{2-1} = -J_{3-1}$. The macroscopic flux will then be $J = J_{1-2} - J_{3-2}$.

$$= n_1 \times \Gamma(n_1) - n_3 \times \Gamma(n_3) \quad (A19)$$

We can write this in terms of jump diffusion coefficient and carrier concentration at any position x in the film. This results in the Fokker–Planck equation (Eq. (A20)), which can be used for inhomogeneous systems [39].

$$\frac{d[D_j(x)n(x)]}{dx} = - \frac{dD_j(x)}{dx} n(x) - D_j(x) \frac{dn(x)}{dx} \quad (A20)$$

In the case where the diffusion coefficient does not depend on position, $\frac{dD_j(x)}{dx} = 0$, and Fick’s first law (Eq. (A1a)) is obtained. The diffusion coefficient for electrons in TiO_2 depends on the carrier concentration. As there is an electron concentration profile, we will obtain a variation in the diffusion coefficient value in the quasi-static approximation of the multiple trapping model. The dependence of the chemical diffusion coefficient D_n on carrier concentration is given by Eq. (A17). If we test $D_j(x) = D_n$ in the Fokker–Planck Eq. (A20), the flux equation appears as:

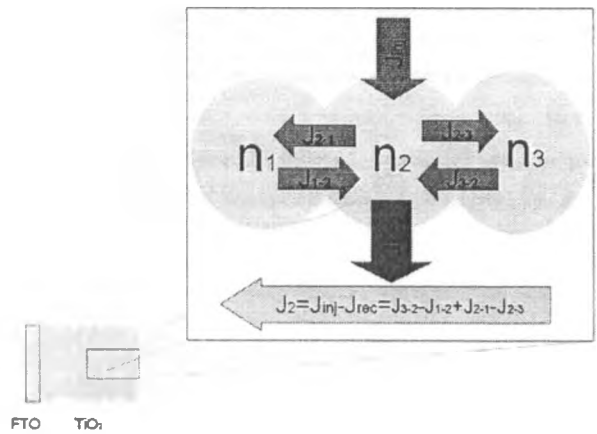


Fig. A1. Schematics of the charge carrier generation, charge transfer between particles and recombination.

$$J(x) = - \left(\frac{T_0}{T} - 1 \right) D_j(x) \frac{dn(x)}{dx} - D_j(x) \frac{dn(x)}{dx} = - \frac{T_0}{T} D_j(x) \frac{dn(x)}{dx} \quad (A21)$$

The flux is thus similar to that of pure diffusion except that the diffusion coefficient is concentration dependent and that an additional constant factor appears. The factor $\frac{T_0}{T}$ is called the thermodynamic factor and originates from the presence of an electron concentration dependent diffusion coefficient [7,33,40]. It can be seen that the jump diffusion, D_j , and the chemical diffusion coefficient, D_n differ by the thermodynamic factor:

$$D_n = \frac{T_0}{T} D_j(x) \quad (A22)$$

References

- [1] B. O'Regan, M. Grätzel, Nature 353 (1991) 737.
- [2] M.K. Nazeeruddin, A. Kay, I. Rodicio, R. Humphry-Baker, E. Müller, P. Liska, N. Vlachopoulos, M. Grätzel, J. Am. Chem. Soc. 115 (1993) 6382.
- [3] M.K. Nazeeruddin, P. Pèchy, T. Renouard, S.M. Zakeeruddin, R. Humphry-Baker, P. Comte, P. Liska, L. Cevey, Emiliana Costa, V. Shklover, L. Spiccia, G.B. Deacon, C.A. Bignozzi, M. Grätzel, J. Am. Chem. Soc. 123 (2001) 1613.
- [4] A. Hagfeldt, M. Grätzel, Acc. Chem. Res. 33 (2000) 269.
- [5] Y. Chiba, A. Islam, Y. Watanabe, R. Komiya, N. Koide, L. Han, Jpn. J. Appl. Phys. 45 (2006) 638.
- [6] M. Grätzel, J. Photochem. Photobiol. C: Photochem. Rev. 4 (2003) 145.
- [7] J. Bisquert, D. Cahen, G. Hodes, S. Ruhle, A. Zaban, J. Phys. Chem. B 108 (2004) 8106.
- [8] L.M. Peter, J. Phys. Chem. C 111 (2007) 6601.
- [9] S. Södergren, A. Hagfeldt, J. Olsson, S.E. Lindquist, J. Phys. Chem. 98 (1994) 5552.
- [10] G. Hodes, I.D.J. Howell, L.M. Peter, J. Electrochem. Soc. 139 (1992) 3136.
- [11] K.D. Benkstein, N. Kopidakis, J. Van de Lagemaat, A.J. Frank, J. Phys. Chem. B 107 (2003) 7759.
- [12] K. Fredin, S. Ruhle, C. Grasso, A. Hagfeldt, Sol. Energy Mater. Sol. Cells 90 (2006) 1915.
- [13] M.J. Cass, A.B. Walker, D. Martinez, L.M. Peter, J. Phys. Chem. B 109 (2005) 5100.
- [14] N. Kopidakis, E.A. Schiff, N.G. Park, J. Van de Lagemaat, A.J. Frank, J. Phys. Chem. B 104 (2000) 3930.
- [15] F. Cao, G. Oskam, P.C. Searson, J. Phys. Chem. 100 (1996) 17021.
- [16] L. Dloczik, O. Ilperuma, I. Lauermann, L. Peter, E. Ponomarev, G. Redmond, N. Shaw, I. Uhlendorf, J. Phys. Chem. B 101 (1997) 10281.
- [17] P.E. de Jongh, D. Vanmaekelbergh, J. Phys. Chem. B 101 (1997) 2716.
- [18] G. Schlichthorl, N.G. Park, A.J. Frank, J. Phys. Chem. B 103 (1999) 782.
- [19] A. Solbrand, H. Lindstrom, H. Rensmo, A. Hagfeldt, S.E. Lindquist, S. Södergren, J. Phys. Chem. B 101 (1997) 2514.
- [20] J. Nissfolk, K. Fredin, A. Hagfeldt, G. Boschloo, J. Phys. Chem. B 110 (2006) 17715.
- [21] B.C. O'Regan, K. Bakker, J. Kroeze, H. Smit, P. Sommeling, J.R. Durrant, J. Phys. Chem. B 110 (2006) 17155.
- [22] F. Fabregat-Santiago, J. Bisquert, G. Garcia-Belmonte, G. Boschloo, A. Hagfeldt, Sol. Energy Mater. Sol. Cells 87 (2005) 117–131.
- [23] Q. Wang, S. Ito, M. Grätzel, F. Fabregat-Santiago, I. Mora-Sero, J. Bisquert, T. Bessho, H. Imai, J. Phys. Chem. B 110 (2006) 25210.
- [24] H. Greijer-Agrell, G. Boschloo, A. Hagfeldt, J. Phys. Chem. B 108 (2004) 12388.

- [25] J.E. Kroeze, T.J. Savenije, J.M. Warman, *J. Am. Chem. Soc.* 126 (2004) 7608.
- [26] E. Hendry, M. Koeberg, B. O'Regan, M. Bonn, *Nano Lett.* 6 (2006) 755.
- [27] A.C. Fisher, L.M. Peter, E.A. Ponomarev, A.B. Walker, K.G.U. Wijayantha, *J. Phys. Chem. B* 104 (2000) 949.
- [28] J. van de Lagemaat, A.J. Frank, *J. Phys. Chem. B* 104 (2000) 4292.
- [29] J. Bisquert, V.S. Vikhrenko, *J. Phys. Chem. B* 108 (2004) 2313.
- [30] J. van de Lagemaat, A.J. Frank, *J. Phys. Chem. B* 105 (2001) 11194.
- [31] J. Nelson, R. Chandler, *Coord. Chem. Rev.* 248 (2004) 1181.
- [32] J. Bisquert, *J. Phys. Chem. C* 111 (2007) 17163.
- [33] J. Bisquert, *Phys. Chem. Chem. Phys.* 10 (2008) 3175.
- [34] J. Halme, K. Miettunen, P. Lund, *J. Phys. Chem. C* 112 (2008) 20491.
- [35] P. Wang, S.M. Zakeeruddin, P. Comte, R. Charvet, R. Humphry-Baker, M. Gratzel, *J. Phys. Chem. B* 107 (2003) 14336.
- [36] A. Solbrand, H. Lindstrom, H. Rensmo, A. Hagfeldt, S.E. Lindquist, S. Sodergren, *J. Phys. Chem. B* 101 (1997) 2514.
- [37] S. Nakade, T. Kanzaki, Y. Wada, S. Yanagida, *Langmuir* (2005) 10803.
- [38] J. Bisquert, *J. Phys. Chem. B* 108 (2004) 2323.
- [39] B.P.v. Milligen, P.D. Bons, B.A. Carreras, R. Sanchez, *Eur. J. Phys.* 26 (2005) 913–925.
- [40] J. van de Lagemaat, N. Kopidakis, N.R. Neale, A.J. Frank, *Phys. Rev. B* 71 (2005).

Conduction Band Edge of (Ti,Sn)O₂ Solid Mixtures Tuning for Photoelectrochemical Applications

J. Simiyu^{*}, B. O. Aduda and J. M. Mwabora,

¹University of Nairobi, Dept. of Physics, P.O. Box 30197 - 00100, Nairobi, Kenya

ABSTRACT

We report investigation of effect of conduction band edge on the dye injection and transport by preparation of (Ti,Sn)O₂ solid mixtures in ratios of 80:20 and 90:10 as possible applications in dye sensitized solar cells. SEM micrographs showed highly porous with nanometer sized particles of around 6 - 10µm diameter. X-ray diffraction patterns showed strong TiO₂ anatase peaks with crystal orientation directions (101) being the strongest in both the solid mixtures and in pure TiO₂. XPS studies have shown an apparent chemical shift for Ti 2p and O1s core level spectra with an energy difference between the unmodified and the solid mixture being 0.65eV. Initial I-V studies have shown high open circuit potential (V_{oc}) but low short circuit photocurrent, showing a possible unfavorable band edge shift between the semiconductor and the dye LUMO level.

INTRODUCTION

Photoelectrochemical solar cells with wide-band-gap oxide semiconductors have received much attention since the development of dye-sensitized solar cell with porous TiO₂ thin film by Gratzel's group [1, 2]. The chemical and physical processes involved in the operation of these cells take place in two-phase system consisting of porous TiO₂ film and I₃⁻/I⁻ redox electrolyte. Charge injection from the photoexcited dye and regeneration of the dye by electron transfer from I⁻ lead to transport of electrons in the TiO₂ as well as transport of I₃⁻ and I⁻ ions in the electrolyte with electron transfer from I⁻ to the oxidized dye and regeneration of I⁻ from I₃⁻ at the counter electrode linking the two transport processes.

To achieve a favorable electron injection efficiency requires proper matching of the dye molecule's LUMO (Lowest Unoccupied Molecular Orbital) level (in excited state) with the conduction band of the semiconductor. Various approaches have been applied, among them using dye molecules that have high LUMO levels in excited state, modifying the conduction band edge of the semiconductor to either lower or raise it [3 - 6] and using redox couples with high molecular orbital levels while maintaining the same band edge for the semiconductor. These studies have been done extensively on single semiconductors like TiO₂, and to lesser extent ZnO and SnO₂ [7, 8].

Recently dye sensitized nanoporous semiconductor materials comprising more than one material have been studied as a possible way to improve on performance [9 - 12]. Tennakone et al. [13] reported the suppression of charge recombination for the mixture (referred to as composite) of SnO₂ with small crystalline size of 15nm and ZnO with large crystalline size of 2 µm. Tai et al [14 - 16] studied widely SnO₂-TiO₂ coupled and composite solar cells using various sensitization dyes. They have reported higher values of Incident Photon to Current

conversion Efficiency (IPCE) in the coupled system compared with that of the composite system, attributing it to a better charge separation due to easy electron transfer in two semiconductor layers with different energy levels. These studies have been mainly on rutile type mixtures; however, anatase (Ti,Sn)O₂ solid mixtures have been reported before [17] but as potential applications in photocatalysis. An investigation of electron transport properties of these mixtures is of great importance for potential application in photovoltaics.

In the present study, sol-gel derived anatase nanostructured (Ti,Sn)O₂ solid mixtures were prepared at two ratios (80:20 and 90:10). The intention was to have SnO₂ formed inside TiO₂ hence only affecting the conduction band edge while maintaining crystal phase of the main semiconductor. Structural properties (SEM, ESCA & XRD) and electrochemical behavior were studied for the two ratios. Current voltage characteristics and electron transport studies were carried out on these solar cells.

EXPERIMENTAL DETAILS

The starting materials were titanium iso-propoxide (C₁₂H₂₈O₄Ti), tin chloride precursors (SnCl₄.5H₂O), iso-propanol and 0.1M ammonia solution. All reagents were of analytical grade and were supplied by Sigma Aldrich unless stated otherwise. 7.4g of SnCl₄.5H₂O was dissolved in 50ml iso-propanol then mixed with 60g titanium iso-propoxide. The resulting solution was then mixed drop wise slowly in 300ml of 0.1M NH₃ under heavy stirring. This method produced instant precipitates, which was then heated to 80°C and peptized at that temperature for 8 hours. The precipitate was then cooled to room temperature and 250ml portion measured out and autoclaved at a temperature of 220°C for 12 hours. This resulted in (Ti,Sn)O₂ suspension of 6.22%wt which was further concentrated in rotor vapor to 20%wt concentration. Finally the paste was centrifuged and washed in ethanol three times to remove the salts and iso-propanol to produce (Ti,Sn)O₂ colloidal solution containing 40%wt. The (Ti,Sn)O₂ colloid in ethanol was then mixed with 20.0g of tarpineol and further underwent stirring – sonication – stirring process. The same process was repeated after addition of 10% ethyl cellulose (Fluka GmbH, Germany) in ethanol to the colloid and then concentrated in a rotor vapor and collected in a reagent bottle. The resulting paste was about 21%wt of (Ti,Sn)O₂ solid mixture.

The above paste was used to coat films on F:SnO₂ conducting glass substrate by screen printing method. The mesh size was 6x8mm and one frame had 20 mesh openings that gave a total of 20 films at a single coating. To coat subsequent layers, the coated film was heated at a temperature of 150°C for five minutes and left to cool to room temperature then another coat applied until the required number of coatings was achieved. The films were then sintered in air for one hour at 450°C and left to cool to room temperature. These films were either used for XRD, SEM and ESCA analysis or assembled into complete solar cells for I-V, and transport/recombination analysis, after determining the film thickness. All films used in this study had 3µm film thickness.

X-Ray diffraction was obtained by means of Siemens D5000 Diffractometer (Bruker AXS GmbH, Germany) with θ -2 θ Parallel beam geometry. The range was from 10° to 80° with detector type of scan at a scan speed of 0.6°/min and step size of 0.01°. (Ti,Sn)O₂ films for XRD analysis were coated on plain glass such that the SnO₂ peaks observed are ascribed to the presence of SnO₂ in the solid mixture. SEM micrographs were measured with LEO 1550 scanning electron microscope at 20kv electron source. ESCA spectra were recorded with

Quantum 2000 scanning ESCA probe (Physical Electronics Inc., USA) with Al K_{α} x-ray source with photon energy of 1486.6eV.

Screen printed films were cut to a size of 3 x 2cm and heat treated at a temperature of 300°C for one hour to remove chemisorbed water and left to cool to 80°C and then subsequently immersed in a dye bath consisting of 0.5mM ruthenium N719 dye complex in ethanol for 12 hours sensitization. Platinised counter electrodes were prepared by coating clean, predrilled conducting glass substrates (measuring 1.5 x 1.5cm), with 48mM of hydrochloroplatinic acid and heating the counter electrode at 450°C for 30 minutes in air and gradually cooled to room temperature. The dye sensitized (Ti,Sn)O₂ photoelectrode and counter electrode were then separated by a 25µm thick thermoplastic surlyn film (DuPont, USA), and sealed by heating. The internal space having the dye sensitized nanoporous film was filled with a drop of the electrolyte through the two holes on the counter electrode. The electrolyte consisted of 0.1M iodine, 0.1M LI, 0.6M TBA, 0.5M 4-terBPY in 3-methoxypropionitrile solvent medium. The electrolyte introduction holes were then sealed with another surlyn film under a thin glass cover by heating. Finally, silver was painted along the edges of the cell to make contacts and to reduce series resistance in the device.

I-V characteristics were obtained using Newport solar simulator model 91160 (Oriel Instruments, USA) to give an irradiation of 100mW/cm² (equivalent of one sun at AM 1.5) at the surface of the solar cells. All the solar cells characterized in this work had an active area of 0.48cm². The current – voltage characteristics under these conditions were obtained by applying an external potential bias to the cell and measuring the generated current with a Keithley 2400 digital source meter (Keithley, USA). This process is fully automated using LabVIEW™ software from National Instruments Inc, USA.

The set up for electron transport and lifetime measurements consisted of Stanford Research Systems lock-in amplifier model SR 570 (Stanford Research Systems, USA), the HP 33120 function generator, and BNC 2110 data acquisition board (National instruments Inc, USA) controlled automatically by LabVIEW™ (National Instruments Inc, USA) application. The light source was from a laser diode (LabLaser, Coherent LabLaser, USA) with λ_{\max} 635nm. Switching from potentiostatic (to measure in short circuit) and galvanostatic (in open circuit) was achieved by use of a solid state switch. Electron transport and lifetime measurement followed a method developed by Boschloo et al. [18] for time resolved measurements. A small square wave modulation (<10% intensity, 0.1 – 2Hz) was added to the base light intensity. The solar cell response was fitted to exponential rise or decay function. Traces were averaged 10times for transport and 2 times for recombination studies.

RESULTS AND DISCUSSION

Structural Properties

From SEM analysis (Figure 1), the films produced were highly porous with nanometer sized particles. However, samples for solid mixtures ((b) and (c)) had slightly smaller particle size than for pure TiO₂ (d). This is possibly due to two main reasons, one being that the starting materials for both batches were different, i.e. pure TiO₂ samples were made from P25 Degussa which has large particle sizes while the solid mixtures were made from titanium isopropoxide and the colloid particle size was determined by the autoclave temperature (which was 220°C). Another

possibility is that the presence of SnO_2 particles in the solid mixture may inhibit the growth of the colloid particles during autoclave digestion.

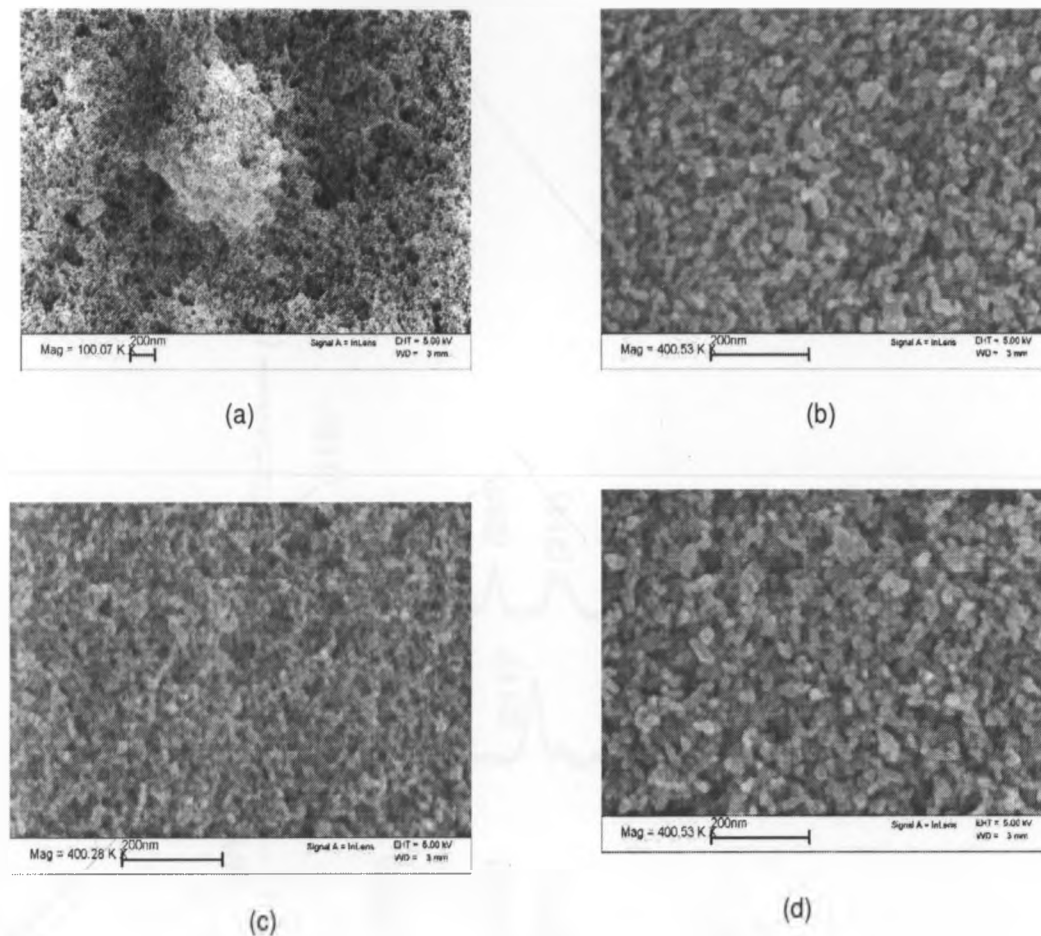


Figure 1: SEM scans for: (a) pure SnO_2 , (b) 80:20 $(\text{Ti,Sn})\text{O}_2$ solid mixture (c) 90:10 $(\text{Ti,Sn})\text{O}_2$ solid mixture and (d) TiO_2

This is because TiO_2 colloids prepared from titanium isopropoxide (not shown in this work) have typical sizes ranging from 10 nm to 30 nm in diameter depending on the autoclave temperature. An increase in autoclave temperature to 250°C did not yield any meaningful rise in the particle size. From XRD analysis' particle size determination using Scherrer's formula, pure SnO_2 and solid mixtures gave particle sizes ranging from 6 nm to 10 nm. The size seemed not to affect dye sensitization as the solid mixtures showed very high dye attaching ability during sensitization. However, solar cells made from solid mixtures had very low I_{sc} which does not agree with high dye attaching ability (this will be discussed in detail under IV results later in the report).

From XRD scans (Figure 2), strong anatase peaks from TiO_2 were observed in solid mixture and in pure TiO_2 with crystal orientation directions (101) being the strongest. Previous works on solid mixtures have mainly produced rutile mixture, but in this work, solid mixtures in anatase form have been produced. Another aspect worth noting is that TiO_2 peaks in pure form do not show any peak shift in mixtures which suggests the absence of crystal phase change when SnO_2

and TiO_2 are mixed. This is important because the only property in focus in solid mixtures is the variation of conduction band edge that should only affect the dye injection and not phase change that may affect the matching between Ti and Sn and hence the electron transfer during transport.

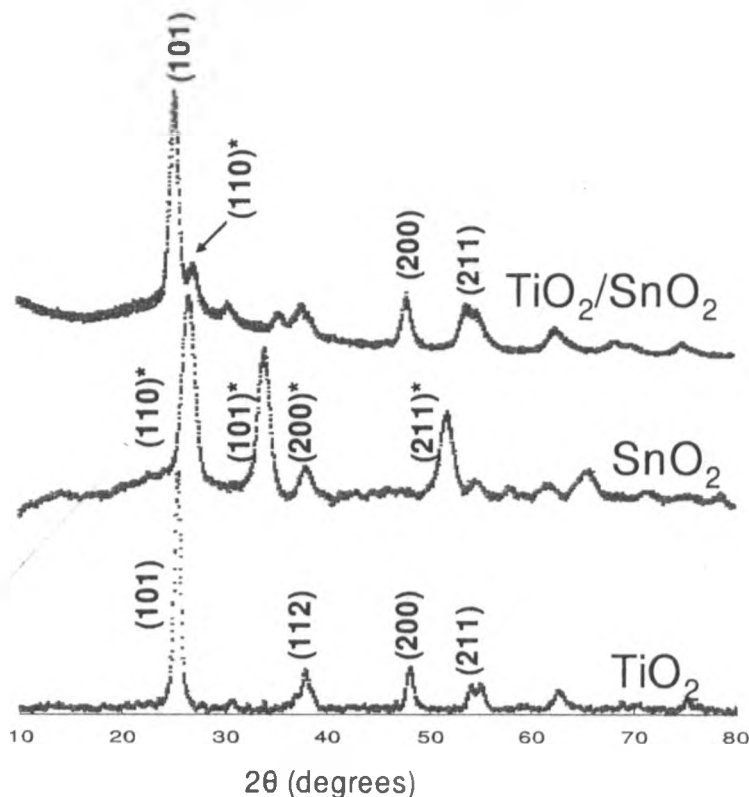


Figure 2: XRD surface scans for pure $(\text{Ti,Sn})\text{O}_2$ and 80:20 $(\text{Ti,Sn})\text{O}_2$ solid mixtures. Bragg reflections with * are for SnO_2 while the ones without are for TiO_2 .

However, at this point, it is not conclusively established that the solid mixture formed is a case where Sn forms within Ti shell and both form solid mixture oxide. XPS analysis so far carried out does not also show that. In Figure 2 for the case of mixtures, the strongest peak for SnO_2 is in (101) direction but due to the small percentage composition compared to TiO_2 it appears to be very small.

ESCA Results

From XPS studies (Figure 3), there is an apparent chemical shift for Ti 2p and O1s core level spectra (figures (c) and (d) on one hand and (e) and (f) on the other); with the energy difference between the unmodified and the solid mixture is found to be 0.65eV. Chemical shifts in SnO₂ have been observed before [19], and have been attributed to possible change in Fermi level position in the semiconductor band gap or just due to band bending. This observation may be a similar occurrence in this case for Ti, which is very likely because it is also expected that O1s peaks shift with the same magnitude. From figures 3 (e) and (f), the energy shift is found to be 0.74eV which is within the range as of Ti 2p.

An interesting observation here is the absence of chemical shift in Sn 3d when mixed with TiO₂ (Figures 3 (a) and (b)). This may partly confirm that SnO₂ forms inside TiO₂ shell which may only affect the conduction band edge while maintaining crystal phase of the main semiconductor (in this case TiO₂). This property was earlier observed in XRD analysis in terms of phase shift.

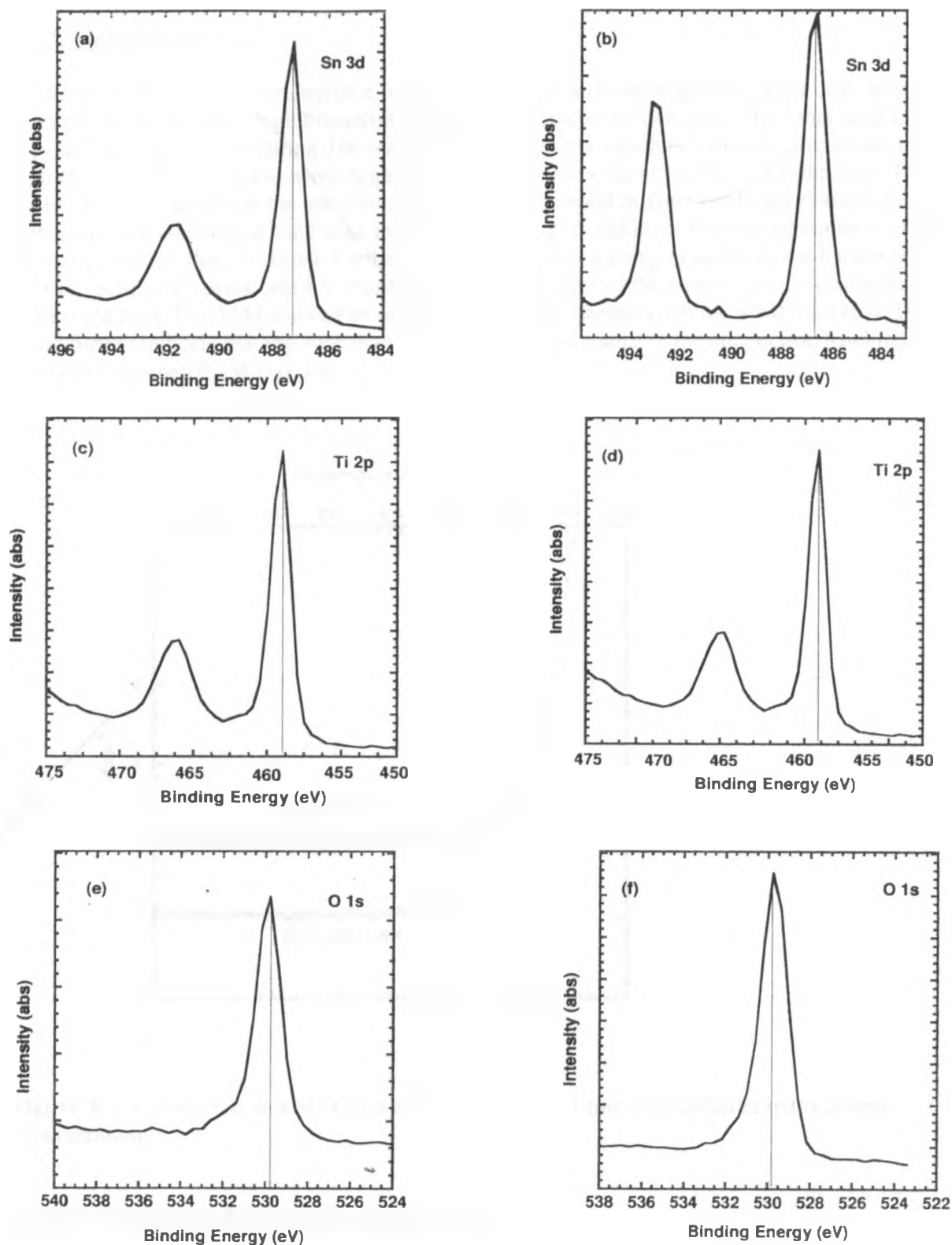


Figure 3: Core level XPS scans for (a) Sn 3d in pure SnO₂ (b) Sn 3d in 80:20 (Ti,Sn)O₂ mixture (c) Ti 2p in pure TiO₂ (d) Ti 2p in 80:20 (Ti,Sn)O₂ mixture (e) O 1s in TiO₂ and (f) O 1s in 80:20 (Ti,Sn)O₂ mixtures

I-V Characteristics

Figure 4 shows I-V characteristics for $(\text{Ti},\text{Sn})\text{O}_2$ solid mixture solar cells. Solar cell samples from this paste exhibited high Photovoltage but low photocurrent densities. The films showed very high dye adsorption during dye-sensitization, a property which is expected to translate to high electron harvesting and hence high photocurrent density; however that is not the case. This could therefore imply that the introduction of SnO_2 in the solid mixture could have raised the semiconductor conduction band edge instead of lowering it, making it hard for electrons to climb the energy barrier that is created. Further investigations are ongoing to ascertain the band edge position involving optical and I-V characterization. A change of the redox couple's concentration from 0.1M LI & I to 0.5M showed an improvement in the photocurrent recorded (plot (b)). This could further indicate that the raise in concentration caused a shift in the conduction band more positive than when 0.1M was used.

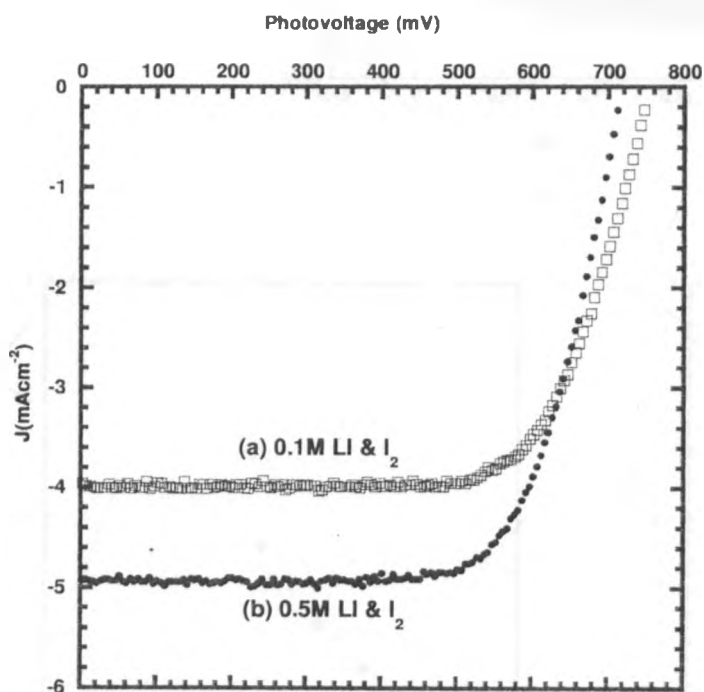
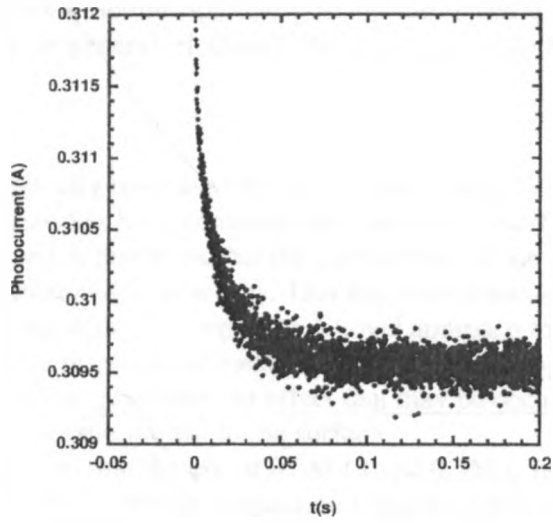


Figure 4: I-V characteristics of $(\text{TiO}_2\text{Sn})\text{O}_2$ solid mixture films with different redox couple concentration

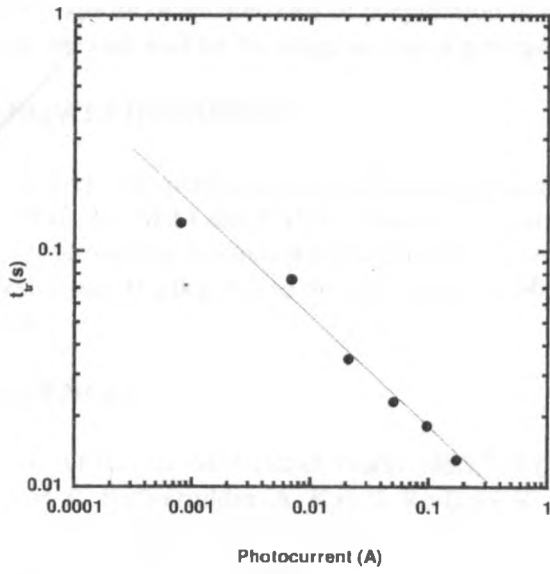
Electron Transport & Recombination Studies

Figure 5 shows electron transport and lifetime results for the solid mixture with 0.5M LI & I_2 redox electrolyte couple; (a) shows the current transient obtained for the sample and (b) is the

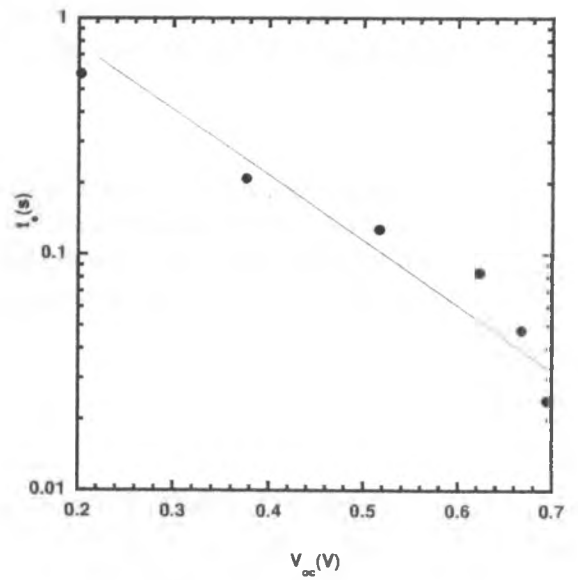
transport time obtained from (a) plotted against the photocurrent at different diode light intensities.



(a)



(b)



(c)

Figure 5. (a) Current transients for charge transport measurements, (b) transport time vs photocurrent and (c) electron lifetime vs photovoltage

The measured electron transport time (t_{tr}) and lifetime (t_e) are shown as function of photocurrent (b) and photovoltage (c) respectively at various light intensities. An exponential relationship is obtained between t_e as reported before in other studies [18, 20, 21]. Samples exhibited long t_{tr} times indicating slow transport process in the solid mixtures. One possible explanation for this is the inconsistent solid mixture formation which may lead to grain boundaries in the nanoporous structure. Another possible cause could be the formation of trap states in the solid mixtures. In general, electron lifetimes were longer than the transport times.

CONCLUSIONS

Sol-gel route has successfully been used here to produce titanium mixed oxide with anatase structure. XRD and ESCA studies have confirmed that mixed (Ti,Sn)O₂ was formed as a solid solution. It has been observed in this work that the particle size of the mixed oxide was smaller than that for the TiO₂ obtained in a similar way. This has been observed before by Marcela et al [17] and from Leite and coworkers' [19] report on a novel approach to control particle size of SnO₂ prepared by the polymeric precursor method, using Nb₂O₅ as dopant. This effect was attributed to surface effect of the precursor, an effect that may be occurring in the present work, i.e presence of SnO₂ restricting the growth to the surface.

Initial results have indicated that the use of 0.5M LI and 0.5M I₂ raised the photocurrent density indicating that there was a shift in conduction band more positive than when 0.1M was used. This could have improved on electron injection in the system hence the increased photocurrent density. However, ESCA results have not conclusively shown that indeed solid mixture was formed with SnO₂ forming inside TiO₂, this leaves room for further work on this and also explore other methods of preparation of this mixtures. More important in the preparation step will be the stage at which precipitates form and when the mixtures are formed.

ACKNOWLEDGEMENTS

This research was performed at Angstrom Laboratory, Uppsala University, Sweden. Authors thank MSL, for SEM and ESCA, Material Chemistry for the X-ray diffractograms, Anders Hagfeldt Group for discussions and hosting me, International Science Programs (ISP) for the fellowship and thanks also to the University of Nairobi for granting me a study leave during this research.

REFERENCES

- [1] B. O'Regan, M. Gratzel, *Nature* **353**, 737 (1991).
- [2] M.K. Nazeeruddin, A. Kay, I. Rodicio, R. Humphry-Baker, E. Muller, P. Liska, N. Vlachopoulos, M. Gratzel, *J. Am. Chem. Soc.* **115**, 6382 (1993).
- [3] R. Cavicchi, M. Tarlov and S. Semanchik, *J. Vacc. Sci. Tech.*, **A8**, 2347 (1990).
- [4] D.F. Cox, T.B., Fryberger and S. Semanchik, *Surface Science*, **224**, 121(1989).
- [5] A. Ciera, A Cornet, J.R. Morante, S.M. Oilaizola, E. Castino and J Gracia, *Mater. Sci. Eng. B*, **66/70**, 406 (2000).
- [6] J. Szuber, G. Czempic, R, Larcuprete and B Adamowicz, *Sensors & Actuators B* **65**, 375 (2000).

- [7] S.E. Lindquist, A. Hagfeldt, S. Sodergren, H. Lindstrom, in: G. Hodes (Ed.), Wiley, Weinheim, pp. 169–200 (2001).
- [8] J.B. Asbury, E. Hao, Y. Wang, H.N. Gosh, T. Lain, *J. Phys. Chem. B* **105**, 4545 (2001).
- [9] C. Nasr, P.V. Kamat, S. Hotchandani, *J. Phys. Chem.* **102**, 10047 (1998).
- [10] K. Tennakone, G.R.R.A. Kumara, I.R.M. Kottegoda, V.P.S. Perera, *Chem. Commun.* 1999 15 (1999).
- [11] K. Tennakone, J. Bandara, P.K.M. Bandaranayake, G.R.R.A. Kumara, A. Konno, *Jpn. J. Appl. Phys.* **40** L732 (2001)
- [12] G.R.R.A. Kumara, K. Tennakone, V.P.S. Perera, A. Konno, S. Kaneko, *J. Phys. D: Appl. Phys.* **34** 868 (2001).
- [13] K. Tennakone, P.K.M. Bandaranayake, P.V.V. Jayaweera, A. Konno, G.R.R.A. Kumara, *Physica E* **14** 190 – 196 (2002)
- [14] Weon-Pil Tai, Kozo Inoue, Eosin Y-sensitized nanostructured SnO₂/TiO₂ solar cells, *Materials Letters* **57** 1508–1513 (2003).
- [15] Weon-Pil Tai, *Solar Energy Materials & Solar Cells* **76** 65–73 (2003)
- [16] Weon-Pil Tai, Kozo Inoue, Jae-Hee Oh, *Solar Energy Materials & Solar Cells* **71** 553–557 (2002)
- [17] M. Marcela, D. Oliveira, C. Danielle, Schnitzler, and A.J. G. Zarbin, *Chem. Mater.* **15**, 1903-1909 (2003)
- [18] G. Boschloo, L. Haggman, A. Hagfeldt, *J. Phys Chem B* **110**, 13144 (2006)
- [19] E.R Laite, I.T. Weber, E. Longo, J.A. Varela, *Adv. Mater.* **12**, 965 (2000).
- [20] J. Nillsfolk, F. Kristofer, A. Hagfeldt, & G. Boschloo, *J. Phys. Chem B*, **110** (36), 17715 – 17718 (2006)
- [21] G. Schlichthorl, S. Huang, J. Sprague, A. Frank, *J. Phys Chem B* **101**, 8141. (1997)

Titania Nanotubes Prepared by Synthesis Method for Dye Sensitized Electrochemical Solar Cells

J. Simiyu¹, J. M. Mwabora¹, B. O. Aduda¹, S-E. Lindquist², A. Hagfeldt² and G. Boschloo²

¹University of Nairobi, Nairobi, Kenya

²Uppsala University, Department of Physical Chemistry, Uppsala, Sweden

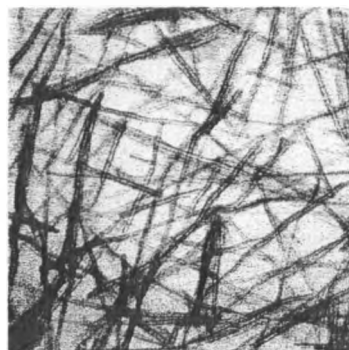
1. Introduction

The area of nanostructured materials for dye sensitized solar cells has gained great interest especially after a breakthrough by Gratzel and coworkers in developing a solar cell from nanostructured oxide of titania gaining an overall efficiency of about 11% [1–5]. Since then the research has been going on with an emphasis on further improvement on this achievement [6–8].

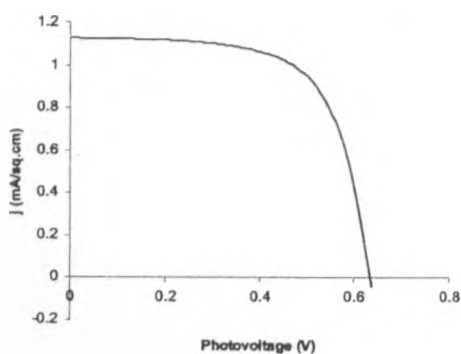
One area that is having a lot of interest is improvement on the charge transfer characteristics from the dye to semiconductor and hence in the whole system. The approach in our research group has been on synthesis of nanofibers of titania oxide that can provide a directed transport of electrons to the conducting back contact and hence giving optimal electronic charge transport through the cell. Titania nanofibers have been synthesised before [9–11], but the reports have been inconclusive as to what stage of synthesis the nanofibers form.

2. Main results

TiO₂ nanofibers measuring average length 500nm and diameter 10nm have been prepared by synthesis method using 10M NaOH and dispersed in alcohol (Fig. 1a). Thin films prepared from the nanofibers had thickness varying from 4.5 – 5.5µm. The films were used to fabricate complete dye sensitised solar cells with Ruthenium complex dye as sensitizer. I-V characteristics yielded Voc and Isc of 0.41V – 0.58V and 0.18mA – to 1.1mA, respectively, under standard illumination of 100mW/cm² (using a halogen lamp and data acquired using Keithley 2400 Source Metre[®] controlled by LabVIEW[®] software) (Fig. 1 b). XRD analysis indicated strong anatase peaks with crystal orientation in the direction (101). This showed that there was no loss of crystalline structure of the TiO₂ during the synthesis process. However, as the sintering temperature was raised, the percentage crystal content of anatase reduced as the rutile structure slowly formed.



(a)



(b)

Fig.1: TEM images for titania nanotubes autoclaved at 500°C (a) in purified water and (b) corresponding I-V characteristics.

3. Conclusion

Initial results have indicated that nanotubes of TiO₂ can be produced by synthesis method and it has also been seen that nanotube formation occurs at the rinsing stage. However, TEM results have not shown conclusively whether the nanotube profile is in tubular form with cylindrical profile or a solid profile. This report has also demonstrated that titanium dioxide nanotubes can be a potential material for solar cells.

References

- [1] M. Grätzel and B. O'Regan, *Nature* **353**, 737 (1991).
- [2] M. Grätzel and A. Hagfeldt, *Chem. Rev.* **95**, 49 (1995).
- [3] M. Grätzel, T. Gerfin and L. Walder, *Chem. Rev.* **44**, 345 (1997).
- [4] M. K. Nazeeruddin, A. Kay, I. Rodicho, Humphry-aker, E. Muller, P. Liska, N. Vlachopoulos, and M. Grätzel, *J. Am. Chem. Soc.* **115**, 6382 (1993).
- [5] V. Aranyos, H. Grennberg, S. Tingry, S-E. Lindquist and A. Hagfeldt, *Solar Energy Materials and Solar Cells* **64**, 97 (2000).
- [6] L. Hammastrom, J. Alsins, A. Borje, T. Norry, L. Zhang and B. Akermark, *J. Photochem. & Photobiol.* **102**, 139 (1996).
- [7] N. J. Cherapy, P. Smestad, M. Gratzel and J. Zhang, *J. Phys. Chem. B* **101**, 9342 (1997).
- [8] G. Smestad, *Solar Energy Materials and Solar Cells* **55**, 157 (1998).
- [9] T. Kasuga, M. Hiramatsu, A. Hoson, T. Sekino and K. Niira, *Advanced Materials* **11**, 1307 (1999).
- [10] Y-K. Zhou, L. Cao, F.-B. Zhang, B-L. He and H-L. Li, *J. Electrochemical Society* **150** (9), A1246 (2003).
- [11] Y. D. Li and X. M. Sun, *Chem. Eur. J.* **9**, 2229 (2003).